Analysis of Flagellar Gait Changes Across Fluid Viscosities:
From Shapes to Motor Models

By

KELLI E. GUTIERREZ
DISSERTATION

Submitted in partial satisfaction of the requirements for the degree of

DOCTOR OF PHILOSOPHY

in

Applied Mathematics

in the

OFFICE OF GRADUATE STUDIES

of the

UNIVERSITY OF CALIFORNIA

DAVIS

Approved:

Robert D. Guy, Chair

Becca Thomases

Harishankar Manikantan

Committee in Charge

2026

For Luma.

Contents

Abstract

Many microswimmers propel themselves using flagella, which are thin, threadlike filaments that beat in a periodic wavelike motion. The flagellar beat emerges from the coupled interactions between the surrounding fluid and the active and passive responses of the flagellum. Previous studies have observed qualitative waveform changes with varying fluid rheology. It is thought that this spatiotemporal coordination among motors is due to mechanical feedback on dynein motors. However, the mechanisms of mechanochemical feedback are not well understood, since the motor forces cannot be measured directly.

In this dissertation, we explore the effects of fluid viscosity on the flagellar waveforms of *Chlamydomonas reinhardtii* swimming in Newtonian fluids. First, we quantify changes in the flagellar waveforms in response to varying fluid viscosity, using (i) shape mode analysis on a dataset of ten cells swimming in fluids with different viscosities, and (ii) a full swimmer simulation to analyze how shape changes affect the swimming speed and to explore the dimensionality of the shape space. The time-independent mean shape changes substantially in response to viscosity, while the changes in the time-varying stroke are more subtle. Second, we develop a computational model that couples a molecular motor model with a nonlinear swimming simulation to examine how motor forces respond to external loading. Although these motor models have been shown to qualitatively reproduce the *Chlamydomonas reinhardtii* waveform, we find that they do not reproduce the beat frequency or beat asymmetry observed in our dataset.

Acknowledgments

First, I want to start by thanking my advisor, Bob Guy, for his mentorship throughout my Ph.D. Bob has continually challenged me to be a better mathematician and thinker, and he has always believed in my abilities, for which I am very grateful. I am so fortunate to have an advisor who cares for my growth as both an academic and a person. I promise to keep trying to make the font in my figures big enough! I also want to thank Becca Thomases, for inviting me into group meeting and supporting me in my Ph.D every step of the way. I have always felt encouraged by Becca throughout this journey and I am especially grateful to her for welcoming me to Smith College for a month last summer. Additionally, I want to thank the final member of my dissertation committee, Hari Manikantan, who taught my favorite fluids course at UC Davis and always was there to offer research and career advice. I feel lucky to have a committee that is so involved and committed to supporting me. I also want to thank the other two members of my qualifying exam committee, Tim Lewis and JP Delplanque, for their guidance and support throughout this process. I would like to acknowledge Tina Denena, Marji LeGrand, and Minh Hoang for all of their support as I navigated the Ph.D. Finally, I want to thank Rohit Thomas and Korana Burke for their mentorship and advice, which helped me grow into a better instructor.

The completion of my Ph.D. would not be possible without the support of other students and postdocs throughout the process. To the Complex Fluids Group, including but not limited to Alana, Alex, Carlos, Thomas, Fizza, Jeff, Michael, Wilder, Ken, and Gavin, thank you for your advice during our weekly group meetings and listening to my bad poetry. I would also like to thank the many friends in the department who have been some of my strongest supporters: Selma, Darian, Alana, Jenny, Lauren, Alaina, and Evuilynn.

Beyond the Ph.D., I would be remiss not to thank those who helped me get here in the first place at University of the Pacific. To Dr. Beltukov, who sat me down in his office during ODEs my freshman year and told me to decide if I wanted to get a Ph.D., thank you for all of your guidance and for setting me up for success. To Dr. Mayberry and Dr. Holland, thank you for being examples of what kind of teacher I want to be and for being such supportive undergraduate advisors. To Dr. Goff, thank you for continuing to support me and for allowing me to teach at UOP during my final year of graduate school! I would also like to thank the 'Outer Product' gang, all of the friends

who helped me learn to program and become a better mathematician and team player, including Justin, Katie, Kadri, Jack, and Savio.

I was also lucky to have a support system outside of graduate school. To Jessica, thank you for listening to me talk about math every time I came to visit and for always being so supportive of my journey. To Tulinh, thank you for letting me stay with you during conferences and for always being encouraging. And finally, to Cassidy (and Kyle), thank you for being the most supportive best friend as I navigated this journey and always being there to hear out my issues with my research, even when you had no idea what I was talking about.

Finally, I want to acknowledge my family for their love and support throughout this process. To my siblings, Julie and Kevin, thank you for listening to my practice talks and for visiting me. To my grandma, Gerry Loritsch, thank you for your love and support during my academic career. To my grandma, Kathy Torres, thank you for listening to me talk about my work every Sunday on our phone calls and for being so supportive even though I know sometimes what I say sounds like nonsense. To my mom and dad, thank you for listening to me give practice talks, for reading my papers, and for helping me with math and physics from the very beginning. I am so lucky to have your support, and I am grateful to have a fun story to tell my students about how you met in calculus class. Finally, to my husband John, for letting me talk though bugs in my code, for making me dinner when I was working, and for being the most supportive and dependable person throughout this entire process. And last but not least, to my cat Luma, who started this journey with me from the very beginning.

CHAPTER 1

Introduction

Microorganisms swim in a wide range of fluid environments, from small algae and *Paramecium* moving through water to mammalian sperm navigating mucus. The study of microorganism locomotion in viscous fluids is important due to its relevance in biological processes such as fertilization, its role in understanding bacterial behavior for disease prevention, and its broader implications for cell motility. Understanding microorganism locomotion has also become important for technological applications including micro-robotics [28, 48] and targeted drug delivery [30, 51].

Many microorganisms swim using flagella, which are thin, threadlike filaments that propagate waves to enable motion at low Reynolds number [52]. The eukaryotic flagellar axoneme is composed of a characteristic 9+2 structure, which consists of nine microtubule doublets around the cylindrical perimeter of the flagellum and two microtubules in the center [9]. When adenosine triphosphate (ATP) is present, dynein motors drive the sliding of these doublets and generate forces [58], which cause flagellar bending and result in a periodic beat. The general structure and the physical mechanisms that govern force generation and bending are well established. The beat emerges from the coupled dynamics of the external fluid, the flagellum and internal motors. It is thought that the dynein motors along the flagellum are coordinated spatially and temporally to produce the observed waves of bending, but the mechanism of mechanochemical feedback that regulates motor activity is not well understood [5, 40, 57, 68].

Evidence of mechanochemical feedback is evident from the observed flagellar gait changes in response to different fluid rheologies [33, 54, 83]. For example, sperm exhibit substantial changes in flagellar waveforms when swimming in fluids with viscosities ranging from 150 and 140,000 times that of water [23, 45, 81]. We aim to quantify how varying fluid viscosity leads to systematic changes in flagellar shape and swimming speed. Few studies explore changes in flagellar gait with small incremental variations in fluid viscosity; notably, Yagi et al. [82], Qin et al. [67], and Wilson et al. [78] document changes in the flagellar beat of the algae *Chlamydomonas reinhardtii* over a narrow viscosity range. In this dissertation, we analyze experimental data from Qin et al. [67] over

a small range of fluid viscosities, quantify the resulting changes in flagellar gait, and investigate how motor forces respond to these changes in fluid viscosity through simulations.

1.1. *C. reinhardtii* Flagellar Beat and Swimming Experimental Data

Chlamydomonas reinhardtii, a single-celled alga, has a small body approximately 10 μm wide and swims using two thin flagella that execute a breaststroke-like motion to pull the cell forward in a fluid. *C. reinhardtii* is often used as a model organism in cell and molecular biology to address key questions, such as how cells generate regular flagellar waveforms [31]. Additionally, *C. reinhardtii*'s two flagella share the 9+2 microtubule structure found in all eukaryotic flagellar axonemes [39], and this alga is widely used in studies of cell and ciliary motility. A practical advantage for experimental work of this organism is that its flagella maintain a nearly constant thickness along their length, making them easier to image and analyze. The original experiment from Qin et al. [67] investigates how changes in fluid viscosity and elasticity affect the swimming behavior of this biflagellated alga.

The experiment systemically modifies the viscosity and elasticity of the fluid in order to study variations in the flagellar beat pattern, beat frequency, and swimming velocity. Fluid viscosity is adjusted in Newtonian fluids by dissolving increasing quantities of increasing amounts of Ficoll (Sigma-Aldrich) in M1 buffer solution, while the elasticity in viscoelastic fluids is controlled by adding small amounts of polymer polyacrylamide (PAA) to water. The Ficoll concentration varies between 5% and 20% by weight in the buffer solution, producing fluids with viscosities ranging between 1 and 6 cP. The polymer concentration ranges from 33.3 to 80 ppm, resulting in fluid relaxation time λ that varies between 0.03 s and 0.12 s. The non-dimensional Deborah number is used to characterize these viscoelastic fluids and distinguishes between the fluid- and solid-like properties of a material. The Deborah number is defined as

$$De = \frac{\lambda}{T}$$

where λ is the fluid relaxation time scale and T is the period of the flagellar beat. For this experiment, the Deborah number ranges from 1.5 to 6.5. Fluid viscosity and elasticity were measured using a stress-controlled rheometer (TA Instruments) [67].

The experimental setup involves suspending motile *C. reinhardtii* cells in fluids, after which a small volume is stretched to form a thin film (thickness $\sim 20\mu m$) using a wire-frame device.

Cell motion in the thin film is captured using an optical microscope and a high-speed camera. When freely swimming, the flagellar gait of *C. reinhardtii* is generally three-dimensional, particularly during turning or rotation [14, 69]. In these experiments, the cells were confined to a thin film to ensure planar swimming, where the film thickness is approximately twice the cell body diameter, preventing the cells from rotating about their swimming axis and ensuring that only swimming in the mid-plane of the film was recorded [67]. Experimental data is therefore obtained for two-dimensional planar flagellar beating only. Any experimental data where the flagellum length deviated more than 10% or where the cell body rotated significantly was excluded.

This dataset include the position of the flagellum over the course of several periods, the average swimming speed, and the frequency of the flagellar beat for six Newtonian and three viscoelastic fluids. More experimental details are found in Qin et. al [67]. This data set is particularly valuable due to the visualization of the flagellar beat patterns shown in Figure 1.1, which allow us to quantify these gait changes.

We focus specifically on the cells in Newtonian fluids and investigate how fluid viscosity quantitatively affects the flagellar waveforms of *C. reinhardtii*. These ten cells, swimming in fluids with viscosities ranging from 1-6 cP, along with their flagellar gait patterns, are shown in the first two rows of Figure 1.1. For each cell, the data consist of the flagellum location in the body frame at time intervals $\Delta t = 0.0017$ seconds for approximately 4-7 full cycles of the periodic beat. At each time point, the positional data include 31 approximately equally spaced coordinates (x, y) along the flagellum. This positional data was smoothed and made differentiable by standard algorithms [67].

Along with the flagellar gaits, the dataset also includes the average swimming speed and frequency of the flagellar beat, which are plotted for the cells in Newtonian fluids in Figure 1.2. As previously observed [54, 63, 67], both the swimming speed and beat frequency decrease with fluid viscosity, but the speed decreases more rapidly than the frequency. Thus, the frequency changes are not entirely responsible for the reduction in swimming speed with increasing viscosity. Figure 1.2c shows that the speed, nondimensionalized by flagellar length and period, decreases with fluid viscosity, which implies that the speed reduction is related to the flagellar gait changes.

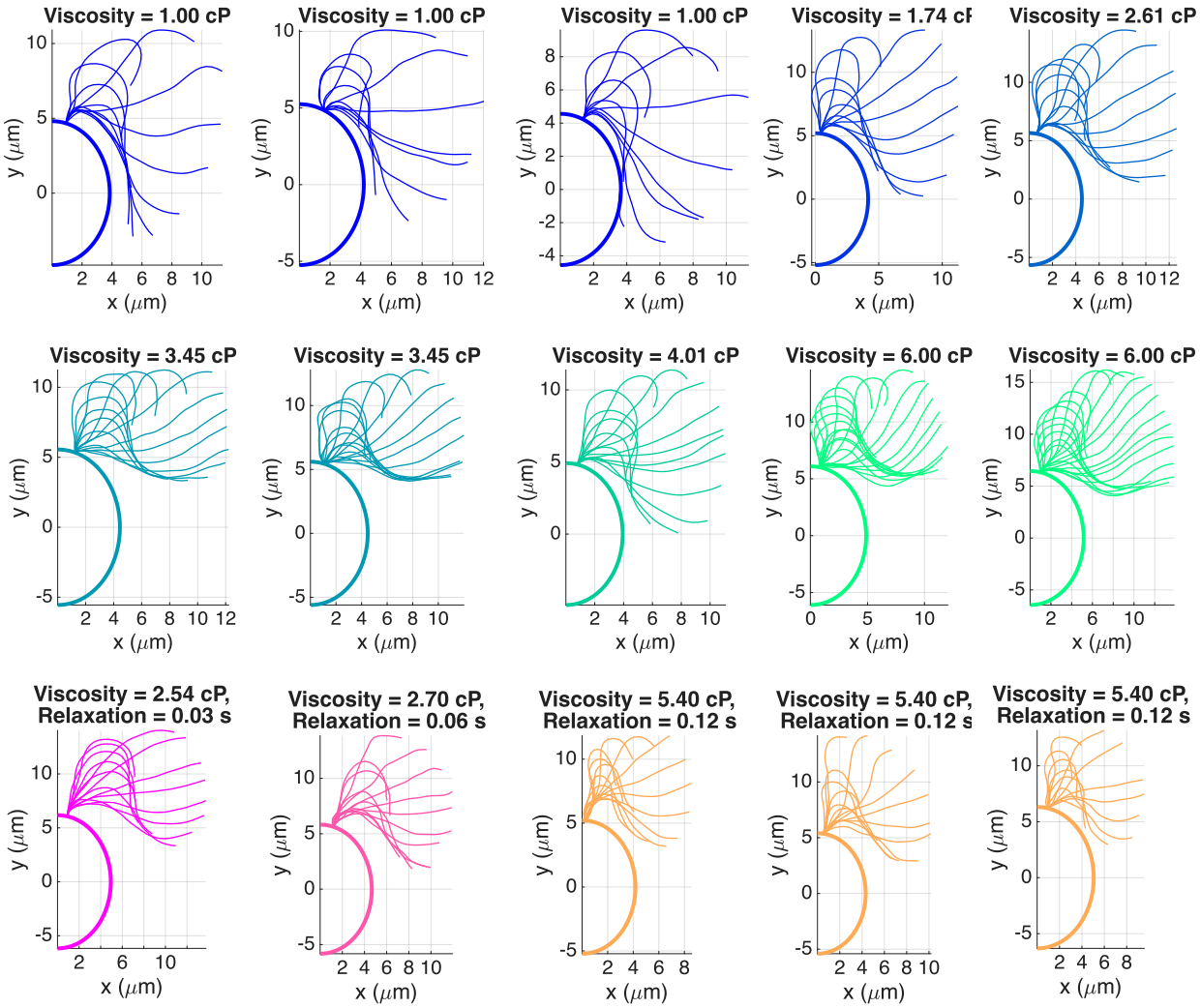

FIGURE 1.1. Flagellar stroke patterns over one period, attached to a *C. reinhardtii* half cell outline centered at the origin, with body size and flagellum length varying across cells. Each panel corresponds to individual cells from experiments in Qin et al. [67]. The first two rows, colored in blue and green, depict cells in Newtonian fluids with viscosities of 1–6 cP. The final row, colored in pink and orange, depicts cells in viscoelastic fluids characterized by viscosities of 2.54–5.40 cP, relaxation times of 0.03–0.12 s, and Deborah numbers ranging from 1.5-6.5.

1.2. Mathematical Modeling of Flagellar Gait Changes with Fluid Viscosity

In this research, we investigate how fluid viscosity affects the flagellar waveform of *C. reinhardtii* in Newtonian fluids using experimental data and numerical swimming simulations. The mechanism behind the observed changes in flagellar shape and swimming speed in response to fluid viscosity cannot be deduced from the experimental data. We explore these effects of fluid viscosity in

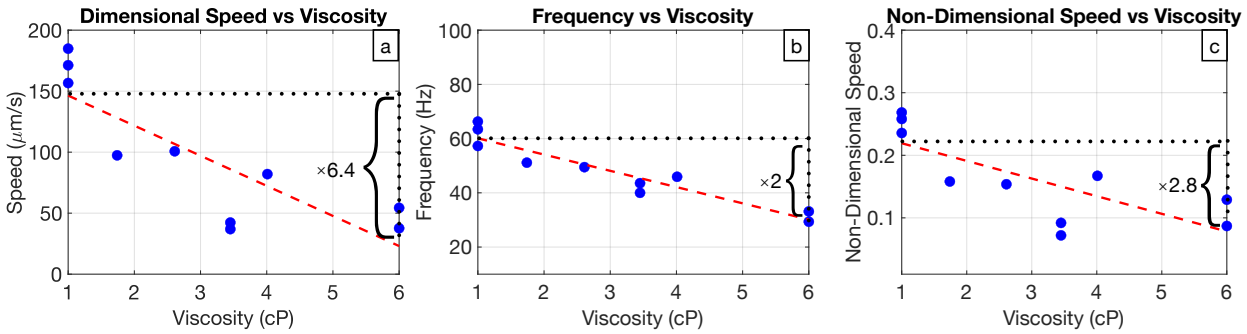

FIGURE 1.2. Effect of increasing viscosity from 1.00 cP to 6.00 cP on the swimming speed and the beat frequency. (a) The dimensional speed decreases by approximately a factor of 6.4. (b) The beat frequency decreases by approximately a factor of 2. (c) The non-dimensional swimming speed decreases by approximately a factor of 2.8.

two ways: (1) quantifying viscosity-dependent changes in the flagellar gait through data analysis and swimming simulations, and (2) examining the mechanisms behind flagellar gait changes by developing a computational model that studies how motor forces respond to external loading.

To quantify the effects of the flagellar beat, we first perform shape mode analysis on the ten cells in Newtonian fluids from the experimental dataset [67]. We identify a unified Newtonian shape basis, construct low dimensional representations of the flagellar beat, and then separately examine how the fluid viscosity influences the mean shape and the time-dependent stroke. We then use a numerical swimming simulation to further quantify changes in flagellar gait with fluid viscosity by investigating the effect of the gait changes on the cell swimming speed. The simulation allows us to isolate the contributions of the mean shape and time-dependent stroke to the swimming kinematics. We find that the viscosity-dependent changes in mean shape have a substantial impact on the swimming speed, whereas changes in the time-dependent stroke with viscosity are comparable to changes seen from cell-to-cell variation.

Next, we investigate the mechanistic origins of these gait changes by studying how flagella generate their characteristic beating patterns. Building on previous work [9, 11, 53, 66, 68], we develop a molecular motor model for the filament where a mechanochemical feedback mechanism regulates the beat. We then couple this model to a swimming simulation in which the flagellar beat emerges from the underlying motor dynamics. This framework enables us to investigate how the emergent flagellar gaits respond to changes in fluid viscosity. In particular, we analyze the effect

of the *C. reinhardtii* cell body on the gait, explore the waveform asymmetry, and examine how the emergent beat frequencies vary with fluid viscosity.

The remainder of the dissertation is organized as follows. In Chapter 2, we introduce shape mode analysis and apply this tool to the *C. reinhardtii* dataset [67] to quantify flagellar shape changes with fluid viscosity and construct a low dimensional representation of the gait. In Chapter 3, we develop a computational swimming simulation for a *C. reinhardtii* cell with a prescribed flagellar gait and use the simulation to further quantify the effects of fluid viscosity on flagellar shape. Portions of Chapters 2 and 3 have been previously published in Gutierrez, et al. [36]. In Chapter 4, we review potential mechanochemical feedback mechanisms that may regulate the flagellar beat and introduce a formulation for a molecular motor model coupled with a swimming simulation. In Chapter 5, we analyze the output of this motor model and conclude with observations about the limitations of the proposed molecular motor mechanism and model.

CHAPTER 2

Using Shape Mode Analysis to Quantify Flagellar Gait Changes

In this chapter, we introduce shape mode analysis [77] as a tool to quantify shape changes in flagellar waveforms with varying fluid viscosity. We discuss multiple approaches for performing shape mode analysis on this data set, but ultimately we identify a unified shape basis for all cells in Newtonian fluids to build low-dimensional reconstructions of the data. We conclude the chapter by quantifying how fluid viscosity affects the mean shape and the time-dependent stroke of the flagellar gait in distinct ways.

Shape mode analysis [77] is a technique which has previously been used to analyze and quantify movement patterns in flagellar waveforms. For example, using shape mode analysis, Guasto et al. [33] demonstrated how external and internal fertilizers have distinct flagellar gaits and Saggiorato et al. [70] showed that sperm steer with the second harmonic of the flagellar beat. Other studies have utilized shape mode analysis to study flagellar datasets of sperm [44, 45, 65, 76, 77, 84] and cilia [74, 75]. Notably, shape mode analysis has been used to study waveforms of *C. reinhardtii* in the contexts of flagellar synchronization [49] and the effect of calcium on the flagellar gait [29]. We utilize this tool on our *C. reinhardtii* dataset [67] to analyze flagellar shape changes with fluid viscosity.

2.1. Shape Mode Analysis

In order to quantify the shape changes in flagellar waveforms with varying fluid viscosity, we utilize shape mode analysis [77], which analyzes different flagellar movement patterns using principal component analysis (PCA) and projects higher-dimensional data onto a low-dimensional set. We investigate the PCA decomposition of our data to quantitatively compare gaits across fluid rheologies.

For each cell, at each point in time, we have the position of a flagellum

$$(x(s_j, t_\ell), y(s_j, t_\ell))$$

where $s_j = j\Delta s$ is the discrete arc length and $t_\ell = \ell\Delta t$ is the discrete time. From these positions, we compute the tangent angles at each point and describe the flagellar shape by a vector of tangent angles, $\vec{\psi}(t_\ell)$. Next, we compute the mean shape across all time steps $\overline{\psi}$, which is the mean of all $\vec{\psi}(t_\ell)$ across different values of t_ℓ. We subtract the mean from these vectors, $\vec{\psi}(t_\ell) - \overline{\psi}$, to give the data a fixed orientation, and collect all of these vectors into an array Ψ. This gives us the array where the ℓ-th column is

$$\Psi^\ell = \vec{\psi}(t_\ell) - \overline{\psi}.$$

All of the data in array Ψ may refer to the data for all time intervals of one particular cell, as described in Section 2.1.1, or the data for all cells at all time intervals in a Newtonian fluid, as described in Section 2.1.2.

To perform shape mode analysis, after combining all of the data into one array Ψ, we define the covariance matrix $C = \Psi^T\Psi$. The eigenvectors of C define an orthonormal basis of shapes called shape modes $\mathbf{S}_k$ [77]. The shape of the flagellum for the jth cell at the time t_m is decomposed as:

$$\vec{\psi}_j(t_m) = \overline{\psi_j} + \sum_k v_k^j(t_m)\mathbf{S}_k, \tag{2.1}$$

where $\mathbf{S}_k$ is the kth shape mode. The coefficients $v_k^j(t_m)$, are defined as a projection of the demeaned data onto that particular shape mode

$$v_k^j(t_m) = \langle \vec{\psi}_j(t_m) - \overline{\psi_j}, \mathbf{S}_k \rangle. \tag{2.2}$$

These time-dependent coefficients characterize how much the kth shape mode $\mathbf{S_k}$ contributes to the data at a particular point in time.

Using shape mode analysis, we investigate the flagellar shapes and how the shape changes with viscosity. This investigation involves analyzing the shapes using individual bases for each cell in the data, as well as analyzing shapes from the perspective of a unified basis across all cells in Newtonian fluids. Particularly, we look at the base shapes $\mathbf{S}_k$ that make up flagellar gait, investigate low-dimensional Fourier series representations of the time-dependent coefficients $v_k^j(t_m)$, and examine how the temporal parts of the stroke and the mean shape change with viscosity.

2.1.1. Individual Basis. We begin the data analysis by performing shape mode analysis on the data from each cell individually. First, we give the data a fixed orientation the data by removing the mean shape, where the mean shape is pictured in Figure 2.1A. As viscosity increases in the Newtonian fluids, pictured in blue and green, the curvature of the mean shape decreases. For the viscoelastic fluids, pictured in pink and yellow, the mean shapes mostly align with mean shapes for flagella in Newtonian fluids of higher viscosity and the curvature does not decrease.

The eigenvalue decomposition of the covariance matrix $C = \Psi^T \Psi$ for each data set produces an orthogonal basis for the shape space. We order the eigenvalues from largest to smallest, which

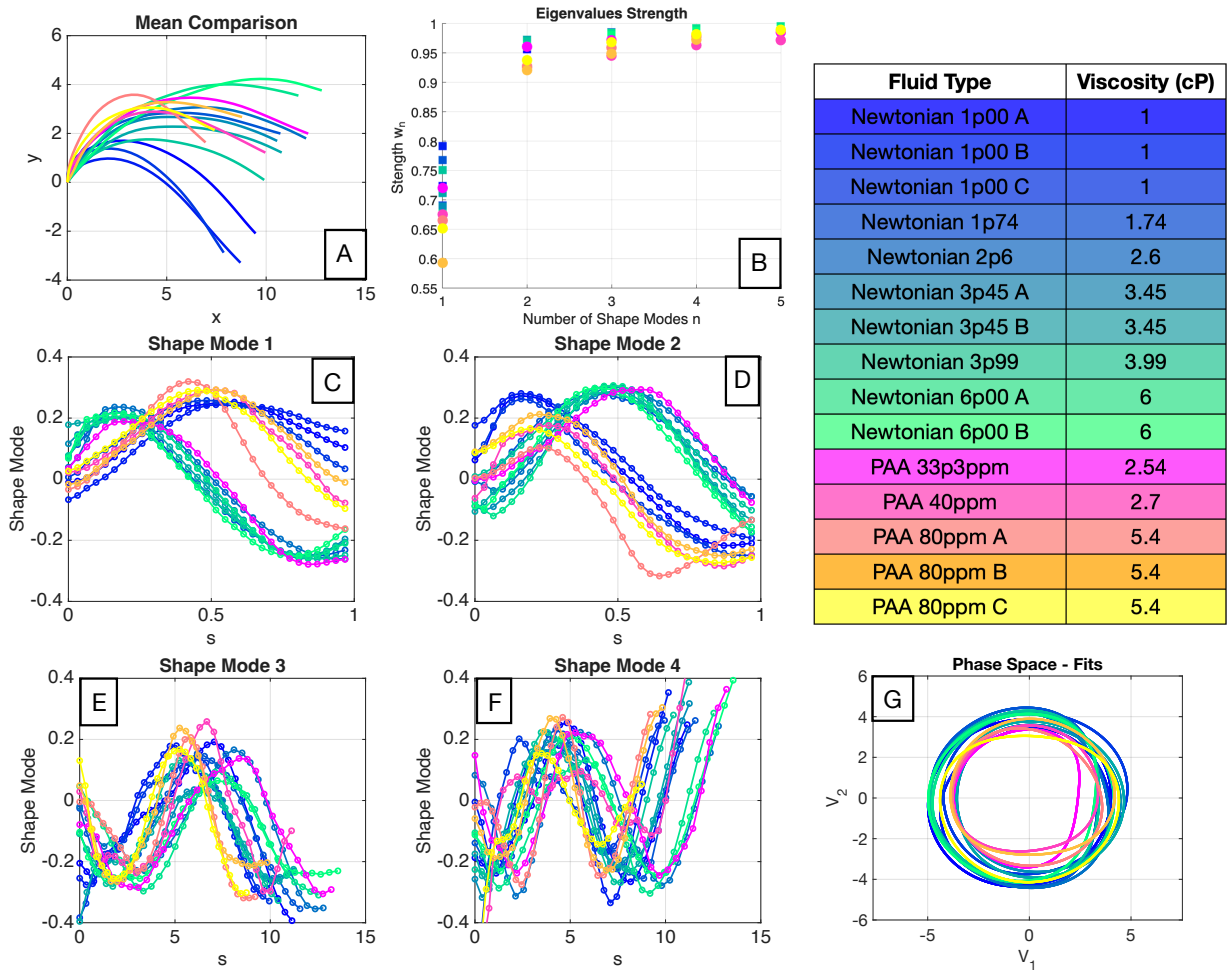

Fluid Type	Viscosity (cP)
Newtonian 1p00 A	1
Newtonian 1p00 B	1
Newtonian 1p00 C	1
Newtonian 1p74	1.74
Newtonian 2p6	2.6
Newtonian 3p45 A	3.45
Newtonian 3p45 B	3.45
Newtonian 3p99	3.99
Newtonian 6p00 A	6
Newtonian 6p00 B	6
PAA 33p3ppm	2.54
PAA 40ppm	2.7
PAA 80ppm A	5.4
PAA 80ppm B	5.4
PAA 80ppm C	5.4

FIGURE 2.1. This figure details shape mode analysis done individually on each cell in the data set, for cells in both Newtonian and viscoelastic fluids. The colors correspond to the fluid viscosity and elasticity as defined in the legend. (A) Comparison of the mean shape. (B) Eigenvalue strength w_n, as detailed in Equation (2.3). (C-F) First four shape modes or eigenvectors of $\Psi^T \Psi$ for each cell in the data set, plotted against arc length s. (G) Fits in phase space using Equation 2.2.

gives an ordering that corresponds to the shape modes' relative contribution to the overall shape of the flagellum. Note this ordering corresponds to that from the singular value decomposition of Ψ, and therefore the eigenvalue λ_i corresponds to the singular value σ_i, i.e. $\lambda_i = \sigma_i^2$.

The eigenvalue strength w_n is defined as

$$w_n = \frac{\sum_{i=1}^{n} \lambda_i}{\sum_i \lambda_i}. \tag{2.3}$$

where λ_i is the ith eigenvalue from the covariance matrix $C = \Psi^T \Psi$ for a particular cell in the data set. The eigenvalue strength quantifies the amount of variability from the space spanned by the first n shape modes contributes to the total variance in the data [62]. The eigenvalue strength w_n for the PCA from each cell in the data is shown in Figure 2.1B.

For each cell, since the eigenvalue strength $w_1 > 0.5$, as shown in Figure 2.1B, the first shape mode contains over half of the information. However, we need at least two different base shapes to produce traveling waves. The first two modes contain most of the information for the all shapes, but we will look at the first four shape modes to get over 95% of the shape information for all bases. The eigenvalue strength changes with the fluid rheology, but it is unclear how this distinction affects how many shape modes are needed to fully represented for the waveforms in different fluids.

The shape modes in Figures 2.1C-F look to be relatively smooth and the number of local extrema increases with mode number. There is not much distinction between data sets for the third and fourth shape mode. Focusing on the first two shape modes, in the Newtonian case, the dominant mode for the fluids with higher viscosities is straighter in the middle and bends on the edges, with approximately odd symmetry and an "S" shape. The mode with the bend in the middle and approximately even symmetry is the dominant mode for the lower viscous fluids, with an "U" shape. The viscoelastic modes match with the less viscous fluids in all but one case, regardless of their viscosity. Though the first two shape modes look different, they appear to be phase-shifted versions of each other. It is unclear from this analysis if the distinction between which cell in the data set has which mode matters in the motion of the flagellum.

The shape modes make up the general shape of the flagellar stroke, and we investigate how these shapes change over a period using the time-dependent coefficients. Recall that v_k^j is described as a time-dependent coefficient of the jth cell associated with the kth shape mode, as defined in Equation (2.2). The time-dependent coefficients $v_k^j(t_m)$ are fit with a Fourier series with N

frequencies as a function of the phase angle $\phi(t)$ as follows:

$$V^j_{k,N}(t_m) = \sum_{n=1}^{N} A^j_{k,n} \sin(n\phi(t_m)) + B^j_{k,n} \cos(n\phi(t_m)). \tag{2.4}$$

The phase angle

$$\phi(t) = \omega t + \phi_0$$

is defined as linear relationship with the slope as the beat frequency, ω, and the vertical intercept as the phase angle, ϕ_0. We can think of the phase angle ϕ_0 as the initial angle, i.e. the location along the loop where the cell begins in its flagellar beat. We visualize v^j_1 and v^j_2 in phase space in Figure 2.1G for reconstructions based on two frequencies. It is difficult to distinguish between the loops in phase space when the shape basis changes with the fluid rheology.

When performing shape mode analysis on each data set individually, trends that correspond with change in fluid viscosity are not obvious. The most distinctive trend is in terms of the mean shape, as the mean curvature decreases with viscosity for the Newtonian fluids. Additionally, visualizing the phase space does not demonstrate any clear trends. In particular, we are comparing limit cycles for different eigenbases, so it is not evident if this is the appropriate method of comparison. The strongest difference between shapes in Figure 2.1 is between those shapes in Newtonian fluids and those waveforms in viscoelastic fluids. Thus, in the following section, we compare these two groups of waveforms by performing PCA on the Newtonian data all together, rather than on all of the data sets individually.

We choose not to continue analyzing the datasets for waveforms in viscoelastic fluids. First, we do not have as much data to compare, so it is more difficult to draw conclusions for only three different rheologies. Second, we eventually will be using a swimming simulation to further quantify changes in flagellar gait in Chapter 3, and building a swimming simulation for a cell in a viscoelastic fluid is more computationally expensive.

2.1.2. Unified Newtonian Basis. In this section, we narrow our focus to the cells in Newtonian fluids and consider a unified shape basis for all of these cells. Again, for each cell, at each point in time, we compute the tangent angles at each point and describe the flagellar shape by a vector of tangent angles, $\vec{\psi}_j(t_m)$, where j indexes the cell. Again, we subtract the time-independent mean shape $\overline{\psi_j}$ from each vector $\vec{\psi}_j(t_m)$ in order to give the data a fixed orientation. We collect all

of these de-meaned vectors into an array Ψ_j for each cell, where $\vec{\psi}_j(t_m) - \overline{\psi_j}$ is the m-th column of Ψ_j. The representation of the flagellar shape for each cell can be decomposed into two parts: a time-independent mean shape, $\overline{\psi_j}$, and a time-varying stroke. To perform shape mode analysis on the data, we combine all of the demeaned arrays Ψ_j into a single array:

$$\Psi = \left[\Psi_1 \;\middle|\; \Psi_2 \;\middle|\; \ldots \;\middle|\; \Psi_j \;\middle|\; \ldots\right].$$

Similar to the previous section, we perform an eigenvector decomposition of the covariance matrix $C = \Psi^T\Psi$, which produces an orthogonal shape basis. Again, the eigenvalues are ordered from largest to smallest when ordering the shape modes to align with the ordering of the singular values from singular value decomposition of Ψ.

The first four shape modes are pictured in Figure 2.2a and look similar to shape modes for asymmetric beats, such as in *C. reinhardtii* [29] or cilia [11]. The first mode has an "S" shape, the second mode has an "U" shape, and for higher-number shape modes, the number of extrema increases, which is similar to the shape modes for different types of sperm [11, 33, 44, 45, 65, 66, 76, 77].

Focusing on the cumulative sum of the eigenvalues, defined as the eigenvalue strength w_n in Equation (2.3), we notice the first two shape modes capture 92.5% of the variance of the data, meaning that only two shape modes are needed to reconstruct the flagellar shapes and include over 90% of variability. From a statistical point of view, two modes are sufficient to represent the

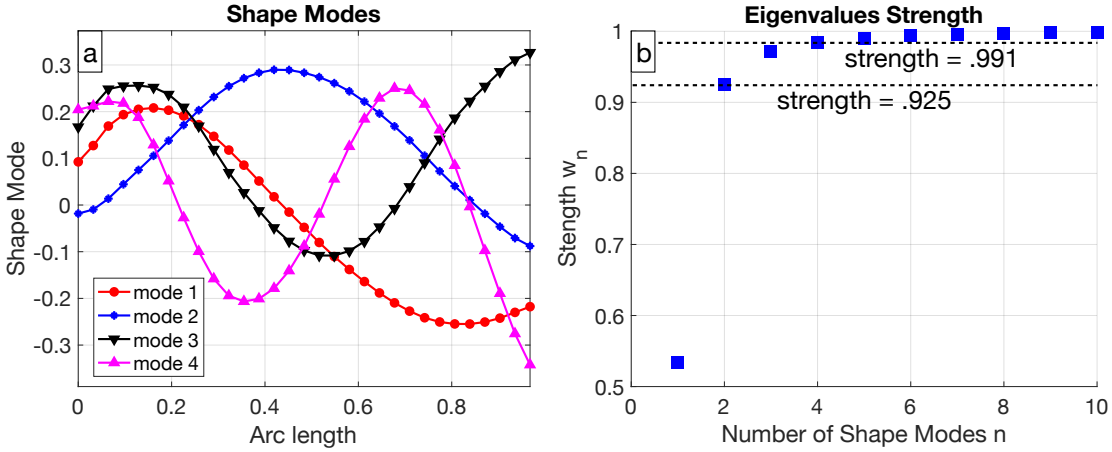

FIGURE 2.2. (a) The first four shape modes plotted against arc length, which are the first four eigenvectors of $\Psi^T\Psi$. (b) The eigenvalue strength w_n, defined in equation (2.3), quantifies the amount of variability captured by n shape modes.

majority of the information about the stroke, which implies the shape space is two-dimensional. It is common for studies utilizing shape mode analysis on sperm and *C. reinhardtii* to only use two modes, since two modes often capture over 90% of the variance [11, 44, 65]. Note that Gholami et al. [29] uses four modes in a *C. reinhardtii* flagellar shape reconstruction, despite two modes capturing over 90% of the variance. It remains to be seen how data variation from higher indexed shape modes affects the swimming speed of the cell, which we will explore in Chapter 3.

In addition to examining the shape modes, we also study how these flagellar shapes change over time by looking at the time-dependent coefficients. The time-dependent coefficient of the jth cell associated with the kth shape mode, v_k^j, is defined in Equation (2.2). We visualize v_1^j and v_2^j in the phase space in Figure 2.3a for a particular example cell.

In Figure 2.3a, each blue data point corresponds to a flagellar shape at a particular point in time from the data projected onto a two-dimensional shape space. The collection of these data points from this sample cell are expected to live on a closed curve since the flagellar beat is periodic [49, 50, 60, 75, 77] and the data covers several periods of the flagellar beat. The polar angle ϕ between v_1^j and v_2^j as a function of time along with its linear fit, $\phi(t) = \omega t + \phi_0$, are shown in Figure 2.3b. The slope of the line, ω, is the angular beat frequency and the intercept, ϕ_0, is the initial angle, i.e. the location along the loop where the cell begins in its flagellar beat. Due to the linearity of the data in Figure 2.3b, the angular speed is constant, meaning

$$\frac{d\phi}{dt} = \omega.$$

This angle ϕ reasonably approximates phase, so we describe the temporal data as functions of the phase angle. Thus, the time-dependent coefficients $v_k^j(t_m)$ are fit with a Fourier series with N frequencies as a function of the phase angle $\phi(t)$ as follows, just as in Equation (2.2):

$$V_{k,N}^j(t_m) = \sum_{n=1}^{N} A_{k,n}^j \sin(n\phi(t_m)) + B_{k,n}^j \cos(n\phi(t_m)).$$

Figure 2.3c shows the time-dependent coefficients for the first four shape modes and a Fourier series phase fit with two frequencies for each set of coefficients.

To choose how many frequencies are needed in each Fourier series fit, we start by examining the time-dependent coefficients in Fourier space in Figure 2.3c. In the top panels in Figure 2.3c(I, III, V, VII), the time-dependent coefficients are plotted in real space against non-dimensional time,

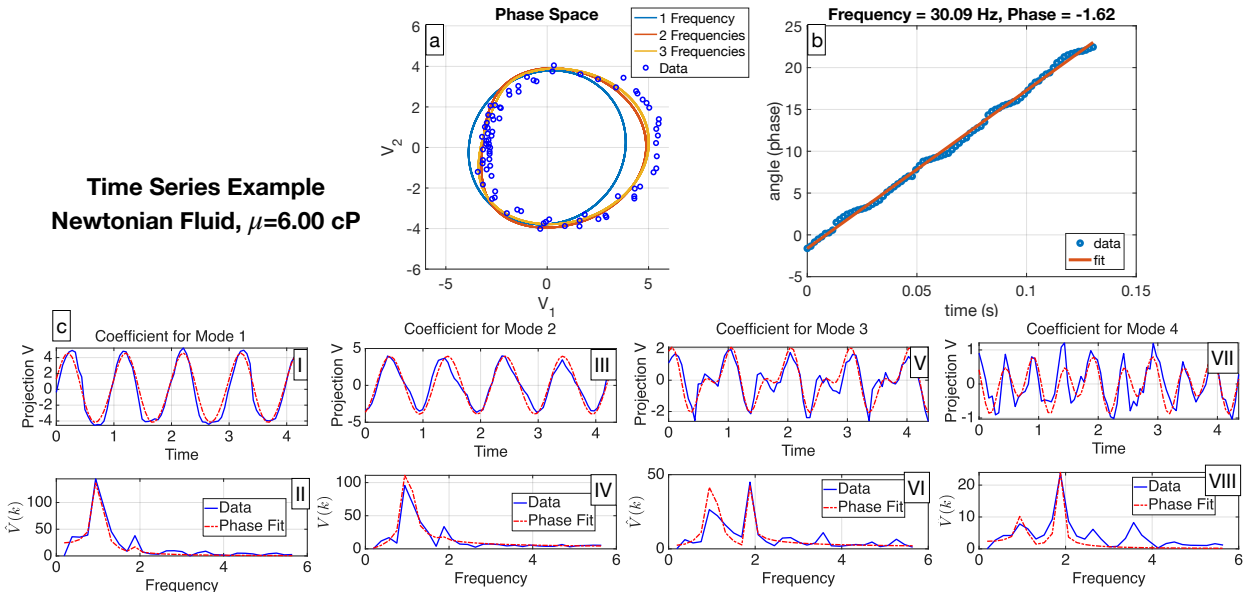

FIGURE 2.3. A time series example for a cell in a Newtonian fluid with viscosity 6.00 cP. (a) Phase space, where the blue data points represent the projection of the experimental data onto the first two shape modes, according to Equation (2.2), and the Fourier series representations for v_1 and v_2 with different frequencies are visualized with the different colored loops. (b) Linear fit for the polar angle in the v_1-v_2 plane, where the slope is the angular frequency and the y-intercept is the initial phase. (c) Fourier series representations for $v_1 - v_4$, with plots (I,III,V,VI) in real space against non-dimensional time and plots (II, IV, VI, VIII) in Fourier space against non-dimensional frequency.

where the Fourier series representations are plotted in red and the data are plotted in blue. In the bottom panels in Figures 2.3c(II, IV, VI, VIII), the time-dependent coefficients are plotted in Fourier space against non-dimensional frequency, where again the Fourier series representations are in red and the data are in blue. In Figures 2.3c(II, IV), for the first two shape modes, there is a strong peak at the dominant frequency and the first harmonic has a smaller but significant peak that is approximately a third of the height. Turning back to phase space in Figure 2.3a, which focuses on the data projected onto a two-dimensional phase space, it is clear that the first harmonic (i.e., the second frequency) makes a substantial difference in the fit, but the third frequency does not make a significant visual difference. In Figures 2.3c(VI, VIII), for the third and fourth shape modes, the dominant peak is at the second frequency, with the first frequency peak being at approximately half of its height. This implies that if the reconstruction has more than two shape modes, at least two frequencies should be used in the Fourier series phase fit. It is important to note that the third and fourth shape modes contribute to 6.6% of shape space, as is shown in Figure 2.2b, so higher

frequencies than the dominant one contribute less to the overall stroke. There is no clear criterion for choosing the number of frequencies to use in Fourier series phase fits solely based on Figure 2.3. We investigate the swimming speed to see how different Fourier series representations affect the flagellar behavior in Chapter 3.

2.1.3. Low-Dimensional Representation. We combine the information we have learned from our Newtonian shape basis in order to form a reconstruction of the data, as illustrated through an example in Figure 2.4. This reconstruction is explained explicitly through Equation (2.1), where $v_k^j(t_m)$ are fit using truncated Fourier series as defined in Equation (2.4). An important feature of this reconstruction is that assuming we are only considering four shape modes for our basis, we

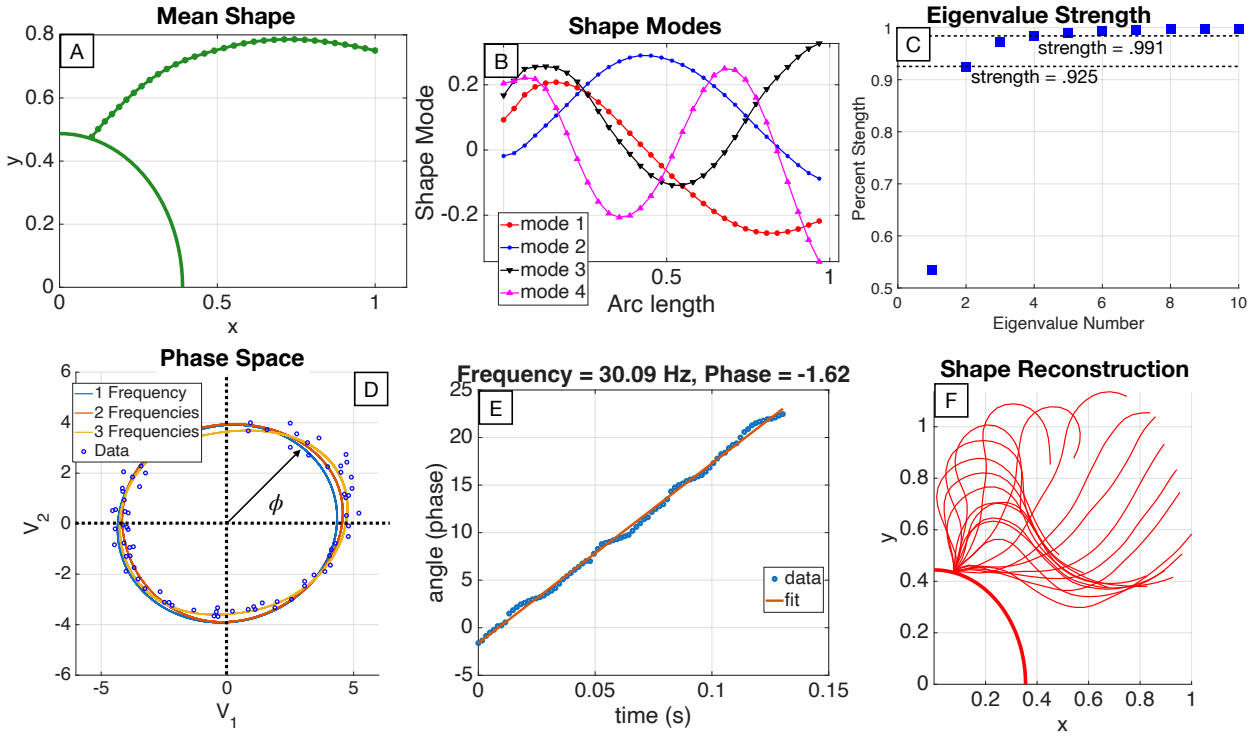

FIGURE 2.4. Method for generating the low-dimensional reconstruction of each cell in the data set. (A) Mean shape for a cell in viscosity 6.00 cP fluid, given as an example of one of the free parameters. (B) Shape basis modes for the Newtonian basis, as seen in Figure 2.2a. (C) Eigenvalue strength denoting the importance of the first four shape modes, as seen in Figure 2.2b. (D) Phase space representation with three different fits to the data for a cell in viscosity 6.00 cP fluid, as visualized initially in Figure 2.3a. (E) Frequency and phase of the flagellar gait, extracted from the data as shown in Figure 2.3b. (F) Shape reconstruction with four basis shape modes and two frequencies in the Fourier series fit, for the flagellar gait of a cell in viscosity 6.00 cP fluid.

have only $8N$ parameters that control the reconstruction of the time dependent stroke at a given point in time, where N is the number of frequencies used in the Fourier series representation of the time-dependent coefficients $v_k^j(t_m)$. This value arises from there being four shape modes, N frequencies, and two different parameters $A_{k,n}^j$ and $B_{k,n}^j$ for each term in the truncated Fourier series representation as seen in Equation (2.4). The mean shape, a function of arc length, is also different for each cell in the dataset.

2.2. Low-Dimensional Representation Comparisons Across Fluid Viscosity

2.2.1. Phase Space - Comparing All Cells. In Figure 2.5, we examine the phase space in order to compare how different numbers of frequencies used in Fourier series representations from (2.4) affect the time-dependent coefficients across all cells. Phase loops reconstructed with only one frequency in the Fourier series are similar in shape, and it is difficult to distinguish between loops of different viscosities. When multiple frequencies are included, the phase loops become less elliptical. The loops at lower viscosities tend to be elongated in the V_2 direction and the loops at higher viscosities are elongated in the V_1 direction, which is visually apparent as the number of frequencies increases.

We quantify the apparent change in loop aspect ratio in Figure 2.5 by looking at relative ratios of two-norms of the time-dependent coefficients. Table 2.1 gives the ratios of the two-norm of the Fourier coefficients of $V_{1,N}^j$ and $V_{2,N}^j$ for each cell. The norm of $V_{k,N}^j$ is given as follows, using the

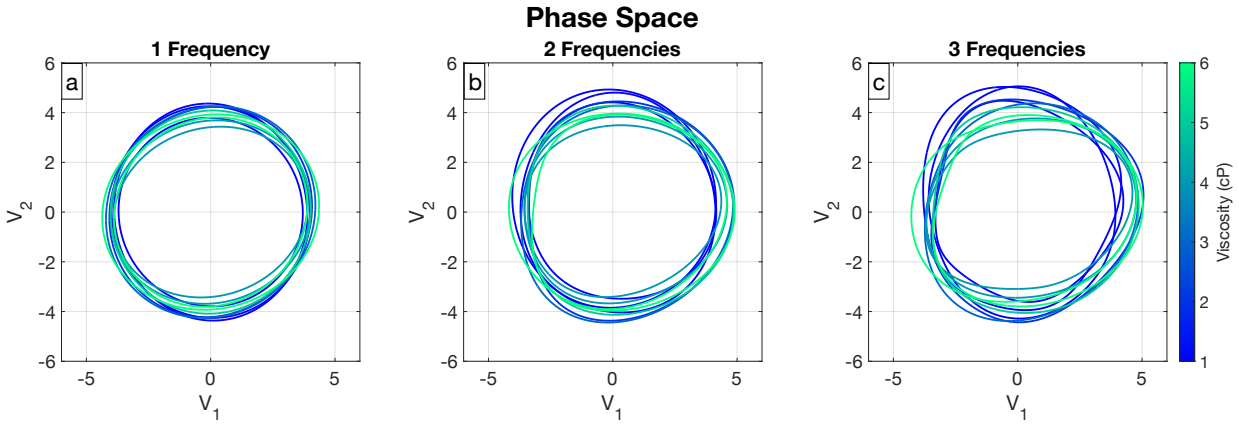

FIGURE 2.5. Phase space comparison. All the figures show the Fourier series representation from (2.4) of V_1 and V_2 plotted in phase space, colored according to viscosity, where curves in (a) have one frequency, those in (b) have two frequencies, and those in (c) have three frequencies.

Vis. (cP)	1.00	1.00	1.00	1.74	2.61	3.45	3.45	4.01	6.00	6.00
$N = 1$	0.94	0.98	0.89	0.96	0.99	1.14	1.09	0.99	1.11	1.02
$N = 2$	0.91	0.95	0.89	0.96	0.99	1.15	1.10	1.01	1.11	1.07
$N = 3$	0.92	0.97	0.89	0.97	0.99	1.15	1.09	1.02	1.12	1.07

TABLE 2.1. Ratios R_N^j described in Equation (2.6), for varying viscosities and number of frequencies $N = 1, 2, 3$.

definition of $V_{k,N}^j$ from Equation (2.4):

$$C_{k,N}^j = ||V_{k,N}^j(t)||_2 = \sqrt{\sum_{n=1}^{N} \left(A_{k,n}^j\right)^2 + \left(B_{k,n}^j\right)^2}. \tag{2.5}$$

The ratios shown in Table 2.1 are defined as

$$R_N^j = \frac{C_{1,N}^j}{C_{2,N}^j}. \tag{2.6}$$

The first row of the table corresponds to Figure 2.5a, the second row corresponds to Figure 2.5b, and the last row corresponds to Figure 2.5c. Table 2.1 shows that the ratio values are less than 1 for viscosities less than 3 cP, and for viscosities larger than 3 cP, the ratio is generally larger than 1. This trend in ratios corresponds to the viscosity dependent elongation that was noted in Figure 2.5 for higher numbers of frequencies, which corresponds to the ratios being less than one, and vice versa. For a single frequency, the ratio trends are visible in the table but not visually apparent in Figure 2.5a. Since the quantitative ratio values in the table do not change significantly with frequency, they do not provide much information about how the number of frequencies affects the flagellum shape or the swimming behavior. We further explore how to choose a Fourier series representation for the time-dependent coefficients in Chapter 3.

2.2.2. Flagellar Mean Shape Changes with Fluid Viscosity. The previous section focuses on analyzing variations about the mean flagellar shape, and here we narrow our focus to the time-independent mean shape itself. Figure 2.6a shows the time-averaged position of the flagellum corresponding to the mean shape. It is clear that the mean shape changes with viscosity. At lower viscosities, the time-averaged flagellar position is closer to the body, and at higher viscosities, the time-averaged position is in front of the body. The same pattern is apparent in Figure 1.1, where the time-dependent flagellar beat is closer to the body at lower viscosities and in front of the body at higher viscosities. The time-independent mean shape appears more curved for lower viscosities,

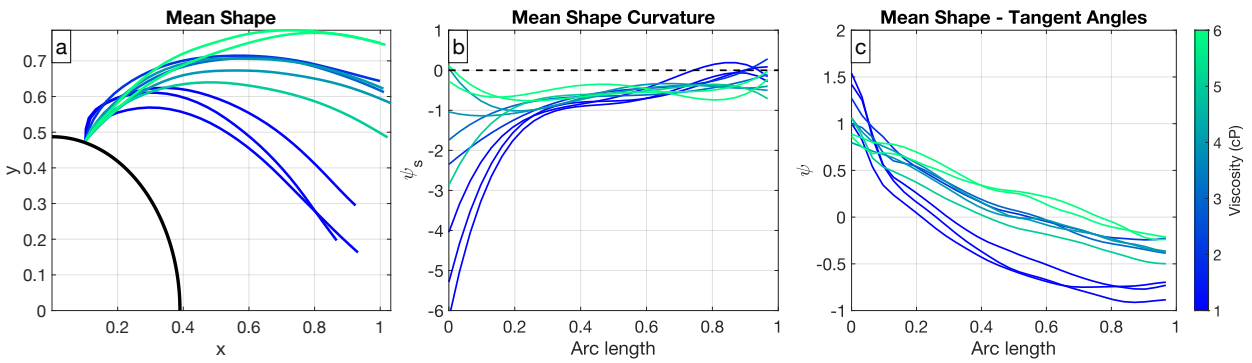

FIGURE 2.6. Different representations of mean flagellar shape, colored according to viscosity. (a) Non-dimensional time-averaged position of the flagellum, attached at a common point to a partial *C. reinhardtii* cell centered at the origin. (b) Non-dimensional curvature of mean shape, ψ_s, plotted against arc length. (c) Tangent angles, ψ, along the flagellum of the mean shape. Arc length zero corresponds to the base.

particularly near the base. In Figure 2.6b, we examine the curvature of the mean shape along the flagellum. The curvature is larger near the basal end in lower viscosity fluids and is relatively constant near the distal end of the flagellum in all fluids.

Previous studies have found fairly constant curvature of the time-independent shape of approximately $0.2\mu m^{-1}$ for isolated and reactivated axonemes of *C. reinhardtii* [1, 26] and uniflagellar mutants of *C. reinhardtii* [21] in buffer fluids with viscosity 1 cP. Examining Figure 9c of Eshel and Brokaw [21], which shows the tangent angles along the flagellum of the mean shape, we notice larger curvature close to the attachment point. In Figure 2.6c, we plot tangent angles for swimming, biflagellated *C. reinhardtii* and observe similarly shaped curves near the base at low viscosities. Although the curvature of the mean shape is not constant at low viscosities, if we compute the spatial average of the curvature for cells in fluid with viscosity 1 cP and average these values across all available cells, we find the spatial average of the curvature is $\sim .195\mu m^{-1}$, which aligns with previous studies [1, 26]. The spatial average of the curvature can be read from Figure 2.6c using

$$\overline{\kappa}_{avg} = \left| \int_0^1 \overline{\kappa} ds \right| = \left| \int_0^1 \overline{\psi_s} ds \right| = \left| \overline{\psi}(1) - \overline{\psi}(0) \right|. \tag{2.7}$$

We observe that the spatial average of the mean shape curvature decreases with fluid viscosity, as seen in Figure 2.7. Note that flagellar lengths range between $10.28 - 14.00\mu m$.

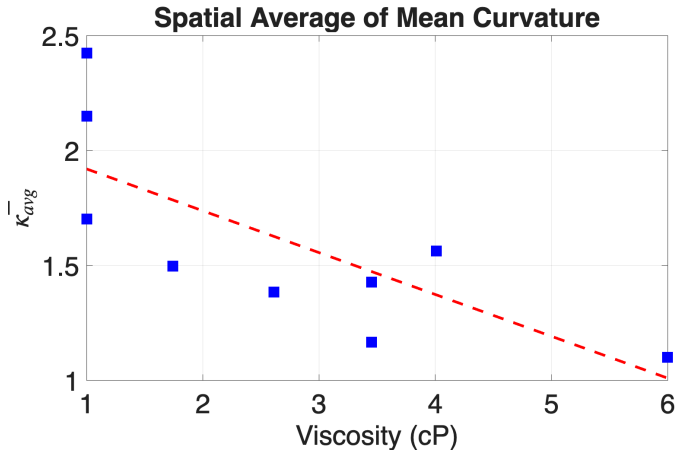

FIGURE 2.7. Spatial average of the mean shape curvature, as described in Equation (2.7). As the fluid viscosity increases, the spatial average of the mean shape curvature $\overline{\kappa}_{avg}$ decreases.

These viscosity dependent trends in mean shape are more obvious to the eye than the changes in time-dependent shapes seen in Figure 2.5. What is unknown is how these trends for mean shape along with the subtle trends in time-varying stroke affect the organism's swimming speed, which we investigate in Chapter 3.

CHAPTER 3

Numerical Swimming Simulations

In this chapter, we quantify how the changes in flagellar stroke with fluid viscosity affect the swimming speed using a numerical simulation. As shown for the *C. reinhardtii* dataset [67] in Figure 1.2, the swimming speed, the frequency of the flagellar beat, and the non-dimensional speed all decrease with fluid viscosity. This implies the frequency and the flagellar stroke change with viscosity and both directly affect the swimming speed.

We also want to understand how the choice of low-dimensional reconstruction affects the swimming behavior. When the number of shape modes and frequencies for the time-dependent coefficients increases, the reconstructed stroke approaches the data. Specifically, the behavior near the flagellum tip looks different in each reconstruction. We analyze how each reconstruction affects the speed to determine which shape reconstruction to use in simulations.

3.1. Low Reynolds Number Swimming

To model the swimming of microorganisms, we first model the fluid dynamics surrounding them. The Navier-Stokes equations describe the momentum balance and conservation of mass in fluid flow. The non-dimensional form of these equations reads:

$$Re\left(\frac{\partial \mathbf{u}}{\partial t} + \mathbf{u}\cdot\nabla\mathbf{u}\right) = \Delta\mathbf{u} - \nabla p + \mathbf{f}, \tag{3.1}$$

$$\nabla\cdot\mathbf{u} = 0, \tag{3.2}$$

where $\mathbf{u}$ is the fluid velocity, p is the fluid pressure, and $\mathbf{f}$ is the external force density. The Reynolds number, denoted Re, is the non-dimensional number which emerges from these equations and is defined as

$$Re = \frac{\rho U L}{\mu}. \tag{3.3}$$

Here, ρ is the fluid density, μ is the fluid viscosity, U is the characteristic speed, and L is the characteristic length scale of the problem. The Reynolds number describes the ratio of inertial forces to viscous forces. In the microorganism regime, viscous forces dominate, so the Reynolds number satisfies $Re << 1$. For the alga *C. reinhardtii*, the characteristic swimming speed is 100μm/s and the characteristic length scale is 10μm. For an alga cell in water, with a viscosity 1 cP and density 1 g/cm^3, the Reynolds number is on the order of $Re \sim 10^{-3}$. Thus, we set $Re = 0$, yielding the Stokes equations:

$$-\nabla p + \Delta \mathbf{u} = -\mathbf{f} \tag{3.4}$$

$$\nabla \cdot \mathbf{u} = 0. \tag{3.5}$$

In the study of flagellated swimmers, there are various approaches to describe the fluid mechanics of thin filaments [52]. Resistive force theory (RFT), or local drag theory [7, 32, 38, 55, 56], relates velocities and forces by treating the slender body locally as a straight cylindrical rod. However, RFT is only quantitatively accurate for very slender filaments and neglects the long-range interactions between different parts of the moving filament and the surrounding fluid [46]. Slender body theory [2, 17, 38, 47] is an improved modeling approach which, in addition to local drag, includes non-local hydrodynamic terms that are derived asymptotically.

When modeling *C. reinhardtii*, we model more than just a single filament, as the cell body is attached to two flagella, where the diameter of the cell body is similar to the flagellar length. Singularity methods for Stokes flows [12, 13] offer useful tools to construct solutions around bodies that are not necessarily slender. A widely used numerical method using singularity solutions is called the method of regularized Stokeslets (MRS) [15, 16], which computes Stokes flows in the presence of immersed boundaries. MRS is discussed further in Appendix A. This method exploits the structure of Stokes equations by computing the flow velocities through integrals of singular solutions along the immersed boundaries and provides a relationship between forces and velocities of the swimmers in Newtonian fluids. Different methods are required to solve fluid-structure interaction problems in non-Newtonian fluids. We utilize the method of regularized Stokeslets in our simulation in the following section.

3.2. Development of the Simulation

3.2.1. Geometry of Cell Body. We develop a three-dimensional computational model of a *C. reinhardtii* cell swimming in a Newtonian fluid at zero Reynolds number. An ellipsoidal body is used to model the cell, and the flagella are attached at the angle $\theta = 0.2147$ radians from the major axis, where this angle is generated by the average of the attachment angles from all cells, as shown in Figure 3.1a. The simulation is done non-dimensionally, where the lengths are scaled by the flagellar length and the time scale is the period of the flagellar beat. The major radius of the cell body in the swimming direction is $r = 0.4873$, which is chosen as the average across all cells in the data set. The other radii of the body are chosen to be 80% of the length of the major radius, since *C. reinhardtii* are generally ellipsoidal [39].

We discretize a model flagellum into thirteen equally spaced points, where the spacing is $\Delta s = 0.0833$. The model body is discretized using maximum determinant points on a sphere [79], with the average spacing between points on the sphere is approximately Δs, and then the body is scaled to the shape of an ellipsoid, as shown in Figure 3.1b. The flagellar gait is prescribed from the shape reconstructions in Chapter 2, where the position and velocity are given in the body frame.

3.2.2. Modeling Approach with Constraints. To solve for the swimming speed of the *C. reinhardtii* cell, we will solve the Stokes equations in order to relate the physics of the flow to that of the swimmer. At each discretized point on the body and flagellar structure, we can

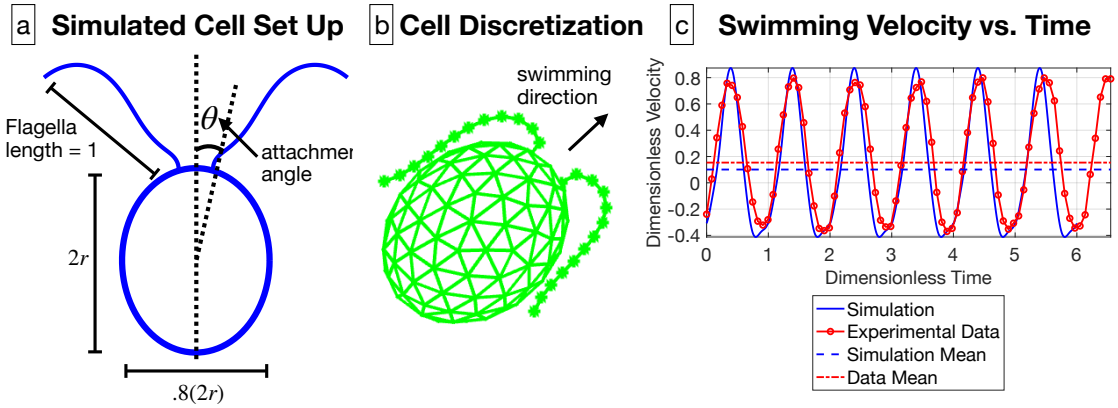

FIGURE 3.1. (a) A schematic of the *C. reinhardtii* cell model in 2 dimensions, including the cell body radius $r = 0.4873$, flagellar length, and attachment angle $\theta = 0.2147$ radians. (b) The discretization of the cell body and the flagella. (c) The swimming velocity from the experimental data and the simulation are compared, along with the mean swimming speed, for the cell swimming in viscosity 2.61 cP.

exploit the linearity of Stokes' equations to solve for the forces on the structure. To solve the Stokes equations, we utilize the method of regularized Stokeslets [15], which takes advantage of the following force-velocity relationship

$$\mathbf{U} = M\mathbf{F}. \tag{3.6}$$

In Equation (3.6), $\mathbf{U}$ is the velocity, M is the regularized Stokeslets mobility matrix, and $\mathbf{F}$ is the force on the immersed structure. The details of this equation and its origins are described in Appendix A.

We know the flagellar shapes from the shape reconstructions in Chapter 2 correspond to the gait in the body frame. Thus, the positions and velocities of the flagella and the cell body are known in the fixed body frame. We could use Equation (3.6) to find the forces in the body frame, using the known body frame velocities, but our goal is to find the swimming speed of the organism in the lab frame.

Let $\mathbf{X_b}$ denote the position of the swimmer in the body frame. To find the position of the swimmer in the lab frame $\mathbf{X_L}$, we relate these positions through a translation and rotation

$$\mathbf{X_L} = R(\mathbf{X_b} - \mathbf{X_0}) + \mathbf{X_T}, \tag{3.7}$$

where R is a rotation matrix, $\mathbf{X_0}$ is the reference point in the fixed body frame, and $\mathbf{X_T}$ is the position of a reference point in the lab frame. $\mathbf{X_T}$ and R are updated with each time step in the simulation, and $\mathbf{X_T}$ is initially set to the origin while R is initially set to the identity.

Again, our goal is to find the swimming speed of the organism in the lab frame. Taking the derivative of the Equation (3.7), after some rearranging, we get the following equation:

$$\mathbf{U_L} = \mathbf{\Omega} \times R(\mathbf{X_b} - \mathbf{X_0}) + R\mathbf{U_b} + \mathbf{U_T}, \tag{3.8}$$

where $\mathbf{U_b} = \partial_t \mathbf{X_b}$ is defined as the velocity in the body frame. The equation involves three unknown quantities: $\mathbf{U_L}$, the swimmer's velocity in the lab frame; $\mathbf{\Omega}$, the rotational velocity; and $\mathbf{U_T}$, the velocity of the reference point $\mathbf{X_T}$. Since one equation is insufficient to determine all three unknowns, we enforce the physical constraints that the swimmer experiences no net force and no net torque, as dictated by the force and torque balance in Stokes flow. Then, after further manipulations

of the equations, including using Equation (3.6), we find the following set of equations:

$$M\mathbf{F} - \boldsymbol{\Omega} \times (\mathbf{X_L} - \mathbf{X_T}) - \mathbf{U_T} = R\mathbf{U_b} \tag{3.9}$$

$$\sum_j \mathbf{F}_j = \mathbf{0} \tag{3.10}$$

$$\sum_j [(\mathbf{X_L} - \mathbf{X_T}) \times \mathbf{F}]_j = \mathbf{0}. \tag{3.11}$$

Note that the indices j in Equations (3.10)-(3.11) notate that we sum across all discrete positions and forces in the system. Once we have solved the for the forces $\mathbf{F}$, translational velocity $\mathbf{U_T}$, and rotational velocity $\boldsymbol{\Omega}$ using Equation (3.14), we then need to solve for the translational position $\mathbf{X_T}$ and the rotation matrix R. We update these quantities by solving the following differential equations:

$$\frac{d}{dt}\mathbf{X_T} = \mathbf{U_T} \tag{3.12}$$

$$\frac{d}{dt}R = \boldsymbol{\Omega} \times R. \tag{3.13}$$

We solve Equation 3.12 using Euler's method. In order to preserve the orthogonal structure of R, we use a geometric integration method to solve Equation 3.13. We use a first order Crouch-Grossman method [18], which is an extension of the explicit Runge-Kutta method.

3.2.3. Assembly of Simulation Matrix System. The system in Equations (3.9)-(3.11) can be rewritten into the following matrix vector system to solve for $\mathbf{F}$, $\boldsymbol{\Omega}$, and $\mathbf{U_T}$:

$$\tilde{A}\begin{bmatrix}\mathbf{F}\\ \mathbf{U_T}\\ \boldsymbol{\Omega}\end{bmatrix} = \begin{bmatrix} M & -A_1 & -A_2 \\ -A_1^T & 0 & 0 \\ -A_2^T & 0 & 0\end{bmatrix}\begin{bmatrix}\mathbf{F}\\ \mathbf{U_T}\\ \boldsymbol{\Omega}\end{bmatrix} = \begin{bmatrix}R\mathbf{U_b}\\ \mathbf{0}\\ \mathbf{0}\end{bmatrix}. \tag{3.14}$$

A_1 is a block matrix which takes the following form:

$$A_1 = \begin{bmatrix}\mathbb{1} & 0 & 0\\ 0 & \mathbb{1} & 0\\ 0 & 0 & \mathbb{1}\end{bmatrix}$$

where $\mathbb{1}$ is a vector of ones of length of the number of discrete points N. A_1 is used to compute the sum in Equations (3.10)-(3.11) and is size $3N \times 3$.

A_2 is a block matrix which represents the cross product with $(\mathbf{X_L} - \mathbf{X_T})$ in Equations (3.9) and (3.11). It takes the following form

$$A_2 = \begin{bmatrix} 0 & (\mathbf{X_L} - \mathbf{X_T})_3 & -(\mathbf{X_L} - \mathbf{X_T})_2 \\ -(\mathbf{X_L} - \mathbf{X_T})_3 & 0 & (\mathbf{X_L} - \mathbf{X_T})_1 \\ (\mathbf{X_L} - \mathbf{X_T})_2 & -(\mathbf{X_L} - \mathbf{X_T})_1 & 0 \end{bmatrix},$$

where $(\mathbf{X_L} - \mathbf{X_T})_j$ refers to the jth component of the vector, assuming three dimensions. A_2 is sized $3N \times 3$. Thus, our full block matrix $\tilde{A}$ in Equation (3.14) is square, symmetric, and sized $(3N+6) \times (3N+6)$ for N discrete points.

When forming this full system, both the body and the flagella are discretized. If the body has N_b discrete points and each flagellum has N_f discrete points, N represents the total number of discretization points, where $N = N_b + 2N_f$. We want the mesh spacing on the body and the mesh spacing along the flagella to be approximately the same. In order to maintain a grid spacing on the body which is approximately the same as $\Delta s = 0.0833$ along the flagellum, this requires the number of body points to be $N_b = 900$, where we are using the maximum determinant points on a sphere [79]. Then, $N_f = 13$, which means that $N = 926$, so $\tilde{A}$ in Equation (3.14) is sized 2874×2874.

3.2.4. Interpolation of Different Cell Body Meshes. To decrease the computational time of the simulation, we employ both a coarse mesh and a fine mesh for the cell body. This allows us to still use the fine mesh where $N_f = 13$ for the flagellum discretization, but reduces the overall size of $\tilde{A}$. We choose a coarse mesh where $\Delta s_{\text{coarse}} = 0.132$, and $N_{b_{\text{coarse}}} = 400$. The unknown forces $\mathbf{F}$ are represented on the coarse mesh, but the fluid solver is employed on the fine mesh. The forces on the coarse mesh are interpolated to the fine mesh using spherical harmonics, and the resulting velocities computed with the fluid solver are projected onto the course mesh, again using spherical harmonics.

Thus, we can rewrite Equation (3.14) with a interpolation matrix $\mathcal{I}_c^f$ that interpolates from the coarse to the fine mesh, and a restriction matrix $\mathcal{I}_f^c$ that restricts from the fine to the coarse mesh.

We rewrite this equation including these interpolation matrices as

$$\begin{bmatrix} M_f & M_{fb}\mathcal{I}_c^f & -A_{1,f} & -A_{2,f} \\ \mathcal{I}_f^c M_{bf} & \mathcal{I}_f^c M_b \mathcal{I}_c^f & -\mathcal{I}_f^c A_{1,b} & -\mathcal{I}_f^c A_{2,b} \\ -A_{1,f}^T & -A_{1,b}^T \mathcal{I}_c^f & 0 & 0 \\ -A_{2,f}^T & -A_{2,b}^T \mathcal{I}_c^f & 0 & 0 \end{bmatrix} \begin{bmatrix} \mathbf{F}_f \\ \mathbf{F}_b \\ \mathbf{U_T} \\ \mathbf{\Omega} \end{bmatrix} = \begin{bmatrix} R\mathbf{U_{b_f}} \\ \mathcal{I}_f^c R\mathbf{U_{b_b}} \\ \mathbf{0} \\ \mathbf{0} \end{bmatrix}. \tag{3.15}$$

M_f refers to the mobility Stokeslets matrix for the discrete flagellar points, M_b refers to the mobility Stokeslets matrix for the discrete body points, and M_{fb} and M_{bf} refer to the mobility matrices which map between the flagellar and body points. The corresponding indices b and f refer to the discrete body and flagellar points, respectively. We compare the translational velocity $\mathbf{U_T}$ from the original simulation based on Equation 3.14 with $N_b = 900$ to the corresponding $\mathbf{U_T}$ from the computationally faster simulation in Equation 3.15. The resulting swimming speeds agree up to four decimal places, so we implement this computational speed up in all simulations in this chapter.

Thus, our simulation begins with a known initial position $\mathbf{X_T}$ and an initial rotation matrix R. At each time step, we solve the matrix system for the rotational velocity $\mathbf{\Omega}$, and the translational swimming velocity $\mathbf{U_T}$. Finally, we need to update $\mathbf{X_T}$ and R for the next time step, which we do by solving evolutionary differential equations. An example of the swimming velocity $\mathbf{U_T}$ that results from the simulation is pictured in Figure 3.1c.

3.3. Dimension of the Reconstruction Shape Space

We first must determine which low-dimensional reconstruction from Chapter 2 to use in the simulation. Adjusting the number of shape basis modes or frequencies for the time-dependent coefficients slightly affects the shape of the flagellar stroke, particularly at the distal end of the flagellum. We can examine the de-meaned waveforms of the flagellar beat in Figure 3.2. We notice that the waveform for the experimental data in blue is still asymmetric in the beat. This asymmetry can be defined clearly by the concept of antiperiodicity. A periodic function f with period p is antiperiodic if

$$f\left(x + \frac{p}{2}\right) = -f(x).$$

Waveforms that have this property are described as symmetric, like $\sin(x)$ or the waveforms shown in Figure 3.2 for two or four basis modes and 1 frequency in the far left panels. However, the

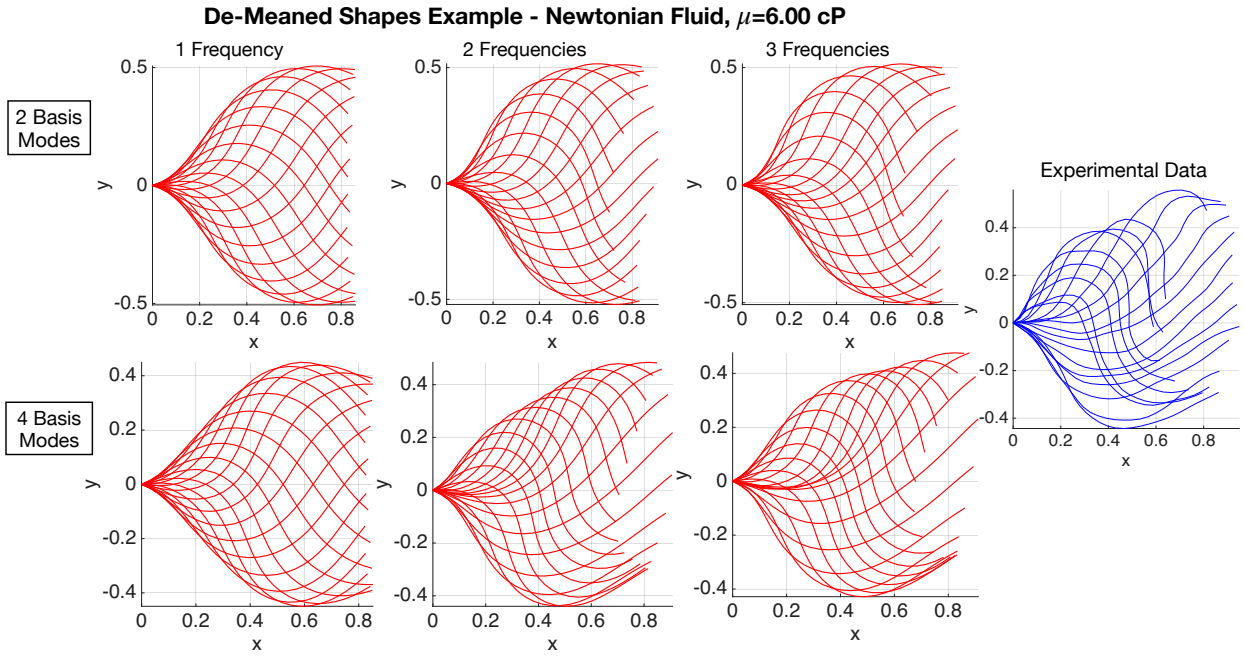

FIGURE 3.2. Flagellar shape reconstruction example, where the mean shape has been subtracted from the waveform. This example is for the cell in a Newtonian fluid with viscosity 6.00 cP, using different numbers of shape basis modes and frequencies. The difference between reconstructions and the experimental data is most apparent near the flagellum tip and in the symmetry of the beat. The length of the flagella is scaled to be one in all panels.

experimental data does not have this property; in fact, the de-meaned waveform is not antiperiodic. In order to generate a waveform that is not antiperiodic, we need a waveform with multiple frequencies. As we increase the number of frequencies for the time-dependent coefficients, we lose the antiperiodicity, and the beat appears asymmetric.

Additionally, we utilize swimming speeds from the numerical simulation to quantify how the swimming speed is affected by the flagellar shape reconstruction. We compare different numbers of shape modes and frequencies for the time-dependent coefficients in Figure 3.3. Based on shape mode analysis, six shape modes statistically gives 99.4% of the shape data. Generally, for the Fourier series representations of the time-dependent coefficients, as seen in one example in Figure 2.3, there are two dominant frequencies in most cells, where some cells have notable peaks at the third or fourth frequencies (ie, the second or third harmonic) in higher shape modes. Thus, we compare speeds to those from a reconstruction using six shape modes and four frequencies.

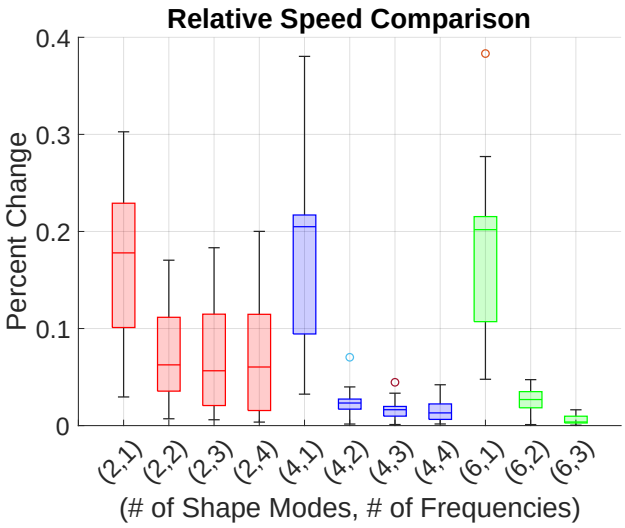

FIGURE 3.3. Relative differences in swimming speed, where swimming speeds from simulations with reconstructions using different numbers of shape modes and frequencies are compared to the swimming speed from a simulation using the reconstruction with six shape modes and four Fourier frequencies.

In Figure 3.3, the relative speed difference for single frequencies is essentially the same for different numbers of shape modes. First, we focus on two shape modes, where the relative speed differences for different number of frequencies are as large as 20% and average around 5%, as shown with the red bars in Figure 3.3. When increasing to four shape modes and two frequencies, the speed difference is generally less than 3% with an average change closer to 2%. As the number of frequencies and shape modes is increased beyond four shape modes and two frequencies, relative speed differences drop below 2%.

Thus, as shown in Figure 3.3, even though the results do not vary greatly between reconstructions, we choose to use four shape modes and two frequencies for the low dimensional reconstruction for the rest of our analysis. We make sure to use at least 2 frequencies, not only because of the affect on the swimming speed as highlighted in Figure 3.3, but also in order to keep the asymmetry of the beat, as shown in Figure 3.2.

3.4. Comparison of Experimental and Simulated Results

The cell swimming speed for the experimental data and the simulation are compared using the reconstruction with four shape basis modes and two Fourier series frequencies in Figure 3.4. There is some variation between the data and the simulation, but many factors may account for these

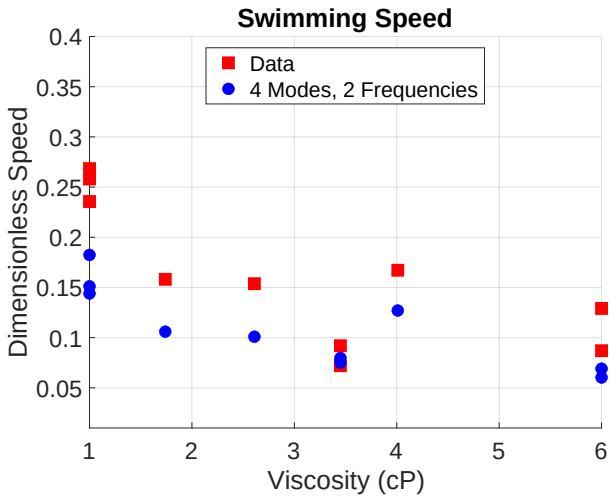

FIGURE 3.4. A comparison of experimental and simulated non-dimensional speed for all cells, where the simulation is based on a reconstruction with four shape modes and two Fourier modes.

differences. The body size, length of the flagella, and position at which the flagella were attached to the body are all held fixed in the simulation, but these vary slightly in the data due to cell variation. The simulation was computed in free space, but the experiment was performed in a thin film to keep the cells swimming in the plane. These changes in the simulation may account for the data and model differences. Despite these differences, the overall trend of the dimensionless speed from the simulation is the same as that of the data. As the viscosity increases from 1.00 to 6.00 cP, the mean speed is approximately halved in both the simulation and the data.

3.5. Varying Mean Shape and Stroke Independently

In Chapter 2, Figures 2.5 and 2.6 detail the comparison of the time-dependent stroke in the phase space and the time-independent mean shape as fluid viscosity varies. It is not clear how these changes in mean shape and stroke contribute to changes in speed. In Figure 3.4, the mean shape and the time-varying stroke from each cell change with viscosity and the non-dimensional speed decreases with viscosity. This introduces the question of how much each factor, the mean shape or the time-varying stroke, contributes to the change in swimming speed. Thus, we vary these two factors independently within the swimming simulation to quantify how each affects the swimming speed. A diagram of how this variation occurs in shown in Figure 3.5. Beginning at the upper left corner, we have a cell in a low viscosity fluid. If we adjust the mean shape to be that from a high

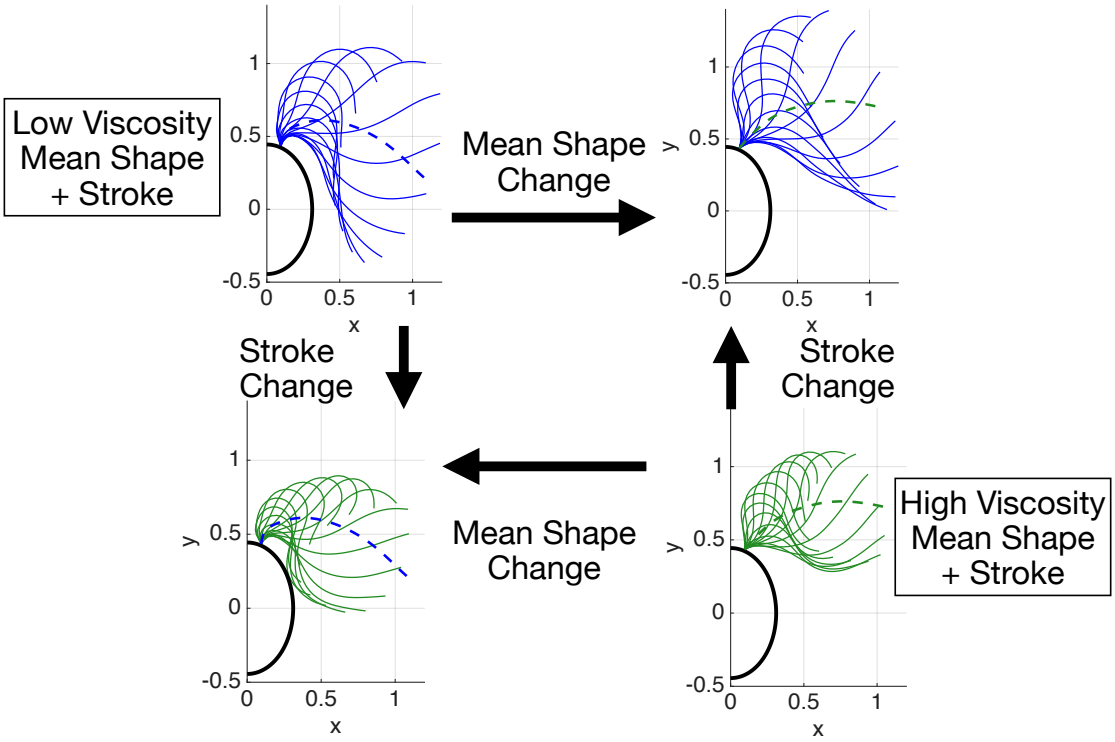

FIGURE 3.5. Diagram illustrating the simulation modifications to mean shape and time-varying stroke. The upper left panel shows a cell in a low viscosity fluid and the lower right panel shows a cell in a high viscosity fluid. Moving horizontally represents replacing the mean flagellar shape and moving vertically represents replacing the time-varying stroke. We look to investigate what happens to the swimming speed when the cells in the lower left and upper right panels are inputted into the swimming simulation.

viscosity fluid by moving to the right in the diagram, we can ask what happens to the swimming speed when we put that cell into our swimming simulation. Similarly, if we adjust the flagellar stroke about the mean shape to be that from a high viscosity fluid by moving downward in the diagram, we can ask what happens to swimming speed with that cell in our swimming simulation. We explore this idea in the following sections.

3.5.1. Effect of Time-Varying Stroke. We initially look at the effect of time-varying stroke on the swimming speed by holding the mean shape fixed and varying the stroke with viscosity. Figure 3.6 depicts two examples, where one mean shape is fixed from a cell in viscosity 1.00 cP and the other mean shape is fixed from a cell in viscosity 6.00 cP. When the mean shape is fixed, the changes in speed are small. Since the R^2 values are less than 0.14, this small decrease in speed is not correlated to the change in viscosity. Thus, the time-varying stroke does not have a strong

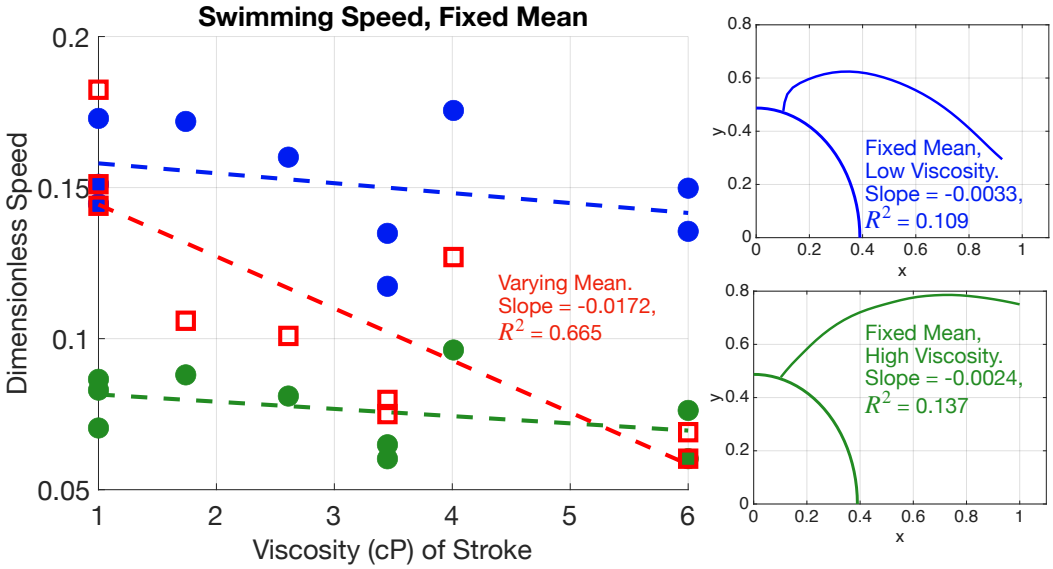

FIGURE 3.6. Simulated speed comparison with the mean flagellar shape fixed from cells in 1 and 6 cP fluids while the time-varying stroke varies. The horizontal axis gives the viscosity of the cell contributing the stroke. Blue and green circles show speeds using mean shapes from 1.00 cP and 6.00 cP cells, respectively, with the corresponding mean shapes shown on the right. Open red squares show speeds where both mean shape and stroke vary with viscosity, matching the blue points in Figure 3.4.

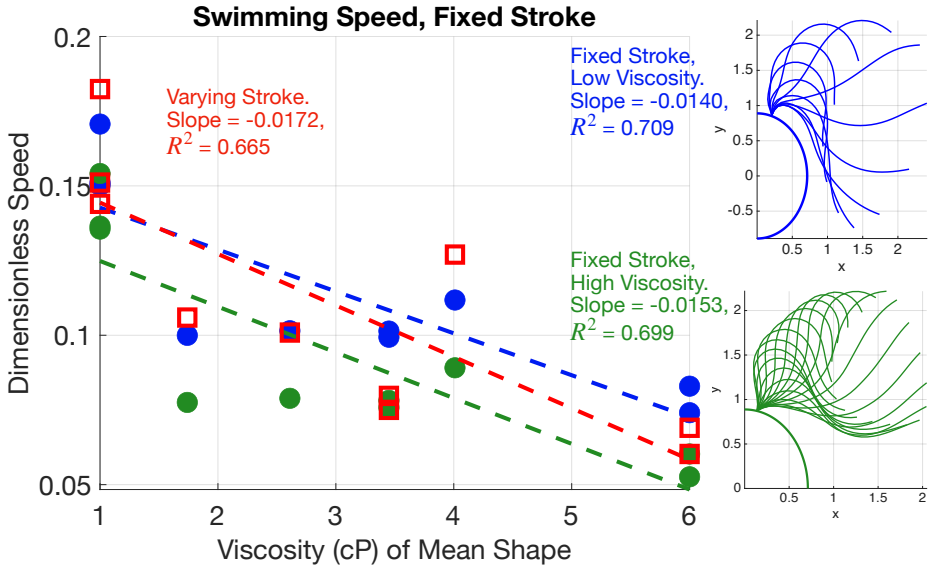

FIGURE 3.7. Simulated speed comparison with the time-varying stroke fixed from cells in 1 and 6 cP fluids while the mean shape varies. The horizontal axis gives the viscosity of the cell contributing the mean shape. Blue and green circles show speeds using time-varying stroke from 1.00 cP and 6.00 cP cells, respectively, with the corresponding strokes shown on the right. Open red squares show speeds where both mean shape and stroke vary with viscosity, matching the blue points in Figure 3.4.

effect on the swimming speed. The changes to swimming speed with varying stroke are on scale with cell variation, as demonstrated in the difference in size of swimming speeds for the different cells in viscosity 1.00 cP in Figure 3.4.

3.5.2. Effect of Mean Shape. Figure 3.7 shows how the mean shape affects the swimming speed by holding the stroke fixed from a specific cell and varying the mean shape across all cells in the data set in the swimming simulations. One fixed stroke is from a cell swimming in water and the other stroke is from a cell swimming in a fluid with a viscosity 6.00 cP. The swimming speeds are similar in Figure 3.7 whether the time-varying stroke changes or is fixed with viscosity. The data points fall on nearby trend lines with similar slopes and R^2 values. The R^2 values demonstrate that the correlation between speed and viscosity does not change whether the stroke is fixed or not, which highlights the important effect of the mean shape on the swimming speed.

3.5.3. Mean Shape Changes Primary Cause for Speed Decrease with Viscosity. Figures 3.6 and 3.7 show the effects of mean shape and time-varying stroke on swimming speed for two specific cells. We now compare combinations across all cells by examining the swimming speed for all combinations of mean shape and time-varying stroke across each cell in the data in Figure 3.8a. Figure 3.8b shows that for a fixed stroke, as the mean shape changes, the speed decreases approximately by a factor of two. Note that in this figure, for cells in the same viscosity, we show the average speed across these cells. Furthermore, we see that the time-varying stroke is not correlated with viscosity by looking at the ordering of the height of the line segments in Figure 3.8b, which do not correspond with viscosity. These results shown in Figure 3.8b are consistent with what was observed in previous sections.

We compare the variation of the stroke changes where the mean shape is fixed for each cell in Table 3.1. This table looks at the standard deviation normalized by the 'natural' speed, or the speed where the stroke and mean shape are from the same cell. These variations are compared to that of cell variation for swimming speeds from cells with the same viscosity. The variation in swimming speed for cells in fluids with viscosity 1.00 cP is 12.84%, and for cells in fluids with viscosity 6.00 cP is 9.59%. While a few of the values in Table 3.1 are slightly larger than these cell variation values, the average of the values in this table is 14.53%, which implies that the majority of minute differences in swimming speed from stroke changes are similar to differences in swimming speed from cell variation. Since the changes in swimming speed due to stroke variation are on the

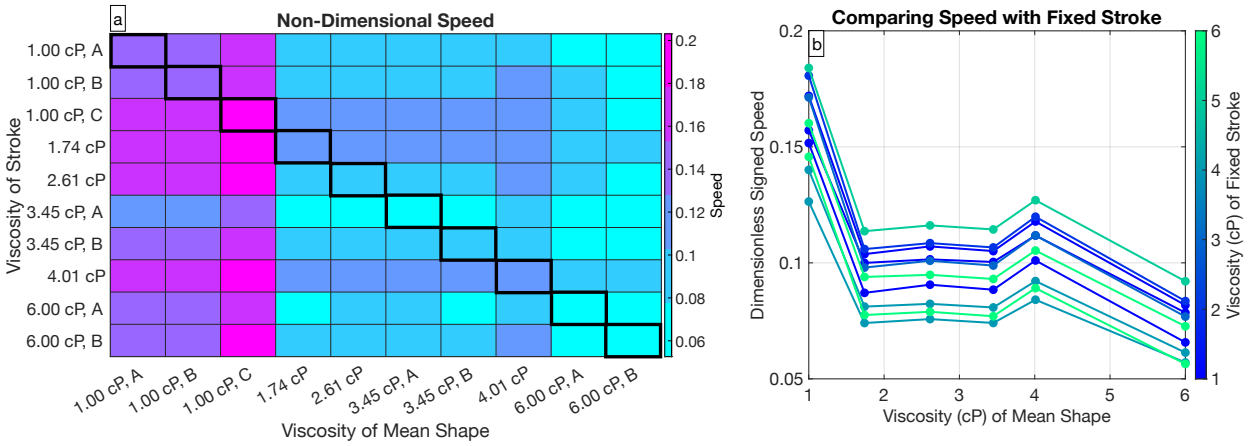

FIGURE 3.8. (a) Swimming speed values for each pair of strokes and mean shapes across the data set. Columns corresponds to a fixed mean shape from a specific cell and rows corresponds to a fixed stroke from a specific cell. (b) Comparison of swimming speed with the time-varying stroke fixed and mean shape varying across different cells in different viscosity fluids. When multiple cells in the dataset are in the same viscosity fluid, the average of the different speeds is shown. Each connected line segment represents a simulation with varying mean shape and fixed stroke from a cell in a specific viscosity fluid.

same scale as changes due to cell variation, we conclude that changes in stroke are not strongly correlated with viscosity.

Both Figure 3.8 and Table 3.1 demonstrate that across all cells, the change in mean shape is the primary cause in the change of non-dimensional speed with viscosity, and the change in time-dependent stroke is not correlated with viscosity changes.

3.6. Discussion

We initially showed in Chapter 2 that the mean shape changes substantially with viscosity, as seen in Figure 2.6. This mean shape is shown to be an important contributor to the change in non-dimensional swimming speed. As depicted in Figures 3.6-3.8, the change in mean shape with

Vis. (cP)	1.00	1.00	1.00	1.74	2.61	3.45	3.45	4.01	6.00	6.00
% Var.	12.30	12.62	10.58	12.41	13.45	18.08	17.00	11.21	20.59	17.02

TABLE 3.1. Variation of swimming speed for varying strokes across different cells in different viscosity fluids, calculated by taking the standard deviation of all of the swimming speeds with a particular fixed mean shape and varying stroke and dividing by the 'natural' speed, where the stroke and mean shape are from the same cell. The viscosity in the first row denotes that of the fluid from the cell which contributes the mean shape.

viscosity majorly contributes to the change in swimming speed. While the small changes in time-varying stroke from shape mode analysis indicate a small dependence on viscosity, as visualized in Figure 2.5, the significance of these changes in stroke is measured by quantifying their effect on the swimming speed in Table 3.1, and we find these speed changes to be on the scale of cell variation. Similarly, Wilson et al. [78] noted that the amplitude of the flagellar gait changes with viscosity. We find that amplitude of the time-varying stroke is not sensitive to fluid viscosity, but rather the change in mean shape is responsible for the observed change in the amplitude of the flagellar beat.

Different potential sources of a force imbalance inside the axoneme that may produce the time-independent mean shape have been proposed [26, 80]. The changes in mean shape we observe may result from passive deformations of the flagellum from the increased external load from swimming in a fluid of elevated viscosity or through feedback on the mechanochemical origin of the force imbalance. We investigate mechanochemical feedback mechanisms on motor activity regulating the dynamic flagellar beat in the following chapter.

CHAPTER 4

Integrating Motor Models into a Swimming Simulation

In this chapter, we examine how eukaryotic flagella generate their characteristic beating patterns and review the mechanochemical feedback mechanisms that have been hypothesized to regulate this beat. We introduce the sliding control motor model [9], and compare the results with previous work. Finally, we develop a swimming simulation for a model of *C. reinhardtii*, in which the hydrodynamics are fully coupled to the sliding control motor model.

Eukaryotic organisms with flagella swim by generating a periodic beating pattern. Each flagellum contains an axoneme composed of a characteristic 9+2 microtubule structure, consisting of nine outer microtubule doublets arranged around the cylindrical perimeter of the flagellum with a microtubule pair in the center [9]. These doublets are connected by nexin, a protein which provides elastic resistance and structural stability to the axoneme. When ATP is present, dynein motors generate internal forces and drive the sliding between adjacent doublets [57].

Although the overall flagellar structure and the physical mechanisms governing force generation are well known, the regulation of motor activity through mechanochemical feedback is not well understood [5, 40, 58, 68]. The beat emerges from the coupled dynamics of the external fluid, the flagellum, and internal motors whose activity depends on deformation. Evidence of such feedback is apparent from the observed flagellar beat changes in response to fluid rheologies [33, 54, 83].

Several different mechanisms have been proposed to explain spontaneous flagellar beating. Many mechanisms have been explored using qualitative, small-amplitude models [5, 6, 68, 73]. These studies typically analyze linear, low amplitude dynamics and discuss that larger amplitude behavior must be studied to fully capture realistic flagellar motion. Over the past decade, multiple studies have explored the intrinsic nonlinearities which arise from coupling the dynein dynamics with the flagellar shape [10, 11, 53, 66].

Mechanochemical motor model results have also been compared with data, including Riedel-Kruse et al. [68] and Gallagher et al. [24] for sperm, and Sartori et al. [73] and Cass and Bloomfield-Gadêlha [10] for *C. reinhardtii*. The majority of these investigations focused on the isolated flagellar

beat, rather than the full microorganism. Gallagher et al. [24] and Li et al. [53] each developed a swimming simulation for sperm that incorporated a molecular motor model using different regulation mechanisms; Gallagher et al. [24] additionally compared their model predictions with data. In these cases, the swimmer head influenced the flagellar motion and was therefore important for understanding how motor activity affects the waveform.

Thus, in this chapter, we begin by discussing mechanochemical feedback mechanisms. We then develop a full swimming simulation for a model *C. reinhardtii* cell, coupling the hydrodynamics with a sliding control motor model.

4.1. Molecular Motor Models

Brokaw [8] and Camalet and Jülicher [9] proposed a simplified model of the 9+2 structure of flagellar axoneme called the two filament model. This model consists of two filaments that slide relative to each other, as seen in Figure 4.1. The top filament is labeled +, the bottom filament is labeled −, and the distance between the two filaments is fixed at a distance a. Springlike objects connect the two filaments, which represent the nexin links that connects the microtubule doublets in the axoneme. A set of motors bridges between one filament to the other, pictured in red in Figure 4.1, and these motors, along with many other motors, bind and unbind to the filaments, generating shear force densities f_+ and f_-. These force densities act in opposite directions on each filament, which causes the filaments to slide relative to one another, resulting in sliding displacement Δ. The sliding displacement is defined as [9, 68]

$$\Delta(s,t) = a[\phi(s,t) - \phi_0(s,t) - \kappa_0 s] + \Delta_0. \tag{4.1}$$

In this equation, ϕ represents the tangent angle of the centerline and Δ_0 represents the sliding displacement at the base of the flagellum. We subtract off the tangent angle at the base point ϕ_0, as well as the constant resting curvature κ_0. We incorporate a constant intrinsic curvature κ_0 that produces spontaneous bending in the absence of active motor forces, representing either the standard base curvature of *C. reinhardtii* flagellum or a prescribed straight reference state. This formulation of the sliding displacement Δ gives a standard resting position of the filament bundle that is not necessarily horizontally placed or flat with zero tangent angle.

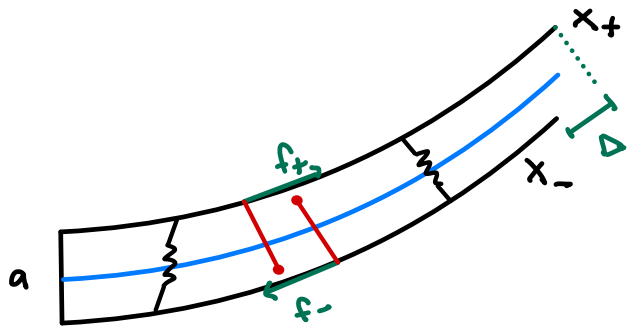

FIGURE 4.1. An illustration representing the two filament simplified model of the axoneme structure [8, 9]. X_+ and X_- represent the top and bottom filaments, respectively. a represents the fixed distance between the two filaments. The internal force density f caused by the motor binding and causes the filaments to slide relative to one another, resulting in sliding displacement Δ, as given in Equation (4.1). The red segments represent the motors, and the black springs model nexin.

This model also takes into account internal stresses due to active and passive elements, including stresses due to passive bending forces and active forces due to the activity of dynein motors. The dynein motors generate these active forces by binding and unbinding to the filament. The binding and unbinding of the motors is thought to be regulated by a feedback control mechanism. These mechanisms are discussed in the following subsections.

4.1.1. Sliding Control Mechanism. The sliding control mechanism describes feedback based on the sliding displacement of the filament. Camalet and Jülicher [9] introduce the idea that motor forces are regulated by a linear response function which depends explicitly on sliding displacement Δ and its time derivative. Riedel-Kruse et al. [68] further this model by deriving an explicit linear response function based on the biophysical force velocity relationship [43]. The motor force $F_\pm$, which is the force exerted by an individual motor attached to the top (+) or bottom (-) filament, is assumed to depend linearly on the sliding velocity $\partial_t\Delta$, such that

$$F_\pm = \pm f_0 \left(1 \mp \frac{\partial_t \Delta}{\nu_0}\right). \tag{4.2}$$

Here, f_0 is the stall force for motor dynamics, where the size of the force corresponds to $\partial_t\Delta = 0$, and ν_0 is the motor walking speed at zero load, or the speed that the motors walk without an applied force. Oriola et al. [66] further develops these ideas by considering the nonlinearities which arise from coupling the dynein activity and flagellar shape by explicitly defining a relationship for binding and unbinding of motors. We describe the model developed by Oriola et al. [66] as follows.

Consider a collection of motors, where $n_\pm$ is the number of motors bound to the top (+) or bottom (-) filament. The force density that results from both active motors and passive links in the filament is

$$f(s,t) = \rho(n_+F_+ + n_-F_-) - K\Delta, \tag{4.3}$$

where ρ is the mean density of motors along both filaments, $F_\pm$ represents the force exerted by the individual motor attached to the top or bottom filament as given in Equation (4.2), K is the effective spring stiffness, and Δ is the sliding displacement given by Equation (4.1). The first term in Equation (4.3) is due to motor activity, while the $-K\Delta$ term represents forces from the passive nexin links.

Changes in force density $f(s,t)$ result in a deformation of the filament, or a change in geometry of the filament. When the filament geometry changes, this leads to a change in the sliding displacement, which directly affects the motor unbinding. Oriola et al. [66] models the control of the binding and unbinding $n_\pm$ as follows:

$$\partial_t n_\pm = \Pi_0(1 - n_\pm) - \epsilon_0 n_\pm \exp\left[\frac{F_\pm}{f_c}\right]. \tag{4.4}$$

In this equation, $\Pi_0(1 - n_\pm)$ represents the binding rate, where Π_0 is the binding rate constant and $(1-n_\pm)$ is the number of unbound motors to the respective filament. $\epsilon_0 n_\pm \exp\left[\frac{F_\pm}{f_c}\right]$ represents the unbinding rate, which has an exponential dependence on the resulting load [64, 66, 68]. ϵ_0 is the rate when there is no applied force and f_c is the characteristic unbinding force of the motors. Evaluating the forces $F_\pm$ from Equation (4.2) with the control of binding and unbinding, the full motor evolution equation is

$$\partial_t n_\pm = \Pi_0(1 - n_\pm) - \epsilon_0 n_\pm \exp\left[\frac{f_0}{f_c}(1 \mp \partial_t\Delta/\nu_0)\right]. \tag{4.5}$$

4.1.2. Curvature Control Mechanism. The curvature control mechanism, originally introduced by Hines and Blum [40], describes feedback where the active dynein motor force is directly dependent on the filament's curvature. The force F, or the force density f, is defined by the expression

$$af(s,t) = a\partial_s F(s,t) = \partial_s(S_r(s,t) - S_d(s,t)), \tag{4.6}$$

where S_r represents the shear force due to deformation of passive components of the axoneme and S_d is the active dynein force. S_d is defined explicitly as

$$\partial_t S_d = \frac{1}{\tau}\left(-m_0 \partial_s \phi - S_d\right), \tag{4.7}$$

where τ is a time constant and m_0 is a constant that determines the effect of curvature feedback on dynein activity. Here, curvature is related linearly to the force. The passive component of the shear S_r is related to the sliding displacement Δ from Equation (4.1) by the nonlinear relationship [40]

$$S_r = k_1 \Delta \left(1 - \frac{1}{\sqrt{1 + k_2 \Delta^2}}\right). \tag{4.8}$$

In this equation, k_1 and k_2 are given constants. More details are provided in Hines and Blum [40] and Bayly and Wilson [6].

The curvature control mechanism has been explored through alternative representations. Sartori et al. [73] uses a linearized model involving curvature control and fits parameters to experimental *C. reinhardtii* data. Gallagher et al. [24] develop a curvature control model based on active moment control, where a change in the sign of the rate of change of active moment density occurs once a threshold curvature is reached. Chakrabarti and Saintillan [11] introduce an explicit dependence on curvature in the motor force $F_{\pm}$, which directly affects the rate of binding and unbinding of motors in Equation (4.4). While these models produce stable oscillatory solutions, a criticism of curvature control is that, unlike the other two feedback models detailed in this chapter, curvature control is not based on a specific biophysical feedback mechanism.

4.1.3. Geometric Clutch Mechanism. The geometric clutch mechanism [58] describes feedback where dynein activity is controlled by the separation between doublets. If the doublets are close enough, dynein motors are more likely to bind to the opposite doublet and more force is produced. If the doublets are far enough apart, they will unbind, dynein activity will decrease, and less motor force will be produced. Bayly and Wilson [5] provide the full details and derivation of these equations presented below.

The equations of motion in this model allow the distance between the doublets to vary. We define h as the distance the doublets separate from a fixed radius a, and the size of h affects the binding and unbinding rates of dynein motors. If the doublets get closer together, the distance between them is $a - h$ and if they move further apart, the distance between them is $a + h$. Thus,

a key difference is the addition of an interdoublet separation equation [5], which is

$$\kappa_b \partial_s^4 h = 2f_N - S\partial_s \phi, \tag{4.9}$$

where κ_b represents the rigidity of the flagellum, ϕ is the tangent angle and

$$S = 2\int_s^L f_T(\xi)d\xi.$$

f_N represents the normal component of the force density, and f_T represents the shear component. The interdoublet forces are the sum of both active and passive contributions. The tangential and normal components of the interdoublet force density are [5]

$$f_T = \overline{f_T}p - k_T\Delta - b_T\partial_t\Delta \tag{4.10}$$

$$f_N = \overline{f_N}p - k_N h - b_N\partial_t h. \tag{4.11}$$

$\overline{f_T}$ and $\overline{f_N}$ denote the maximum active dynein force densities in the tangential and normal directions, respectively. p is the probability that the dynein motor will attach to the doublet, and is a function of h. Finally, the tangential force $-k_T a\phi - b_T a\partial_t\phi$ and normal force $-k_N h - b_N\partial_t h$ are passive forces which oppose the deformation of the axoneme [5]. k_T and k_N are the interdoublet shear and normal stiffness coefficients, and b_T and b_N are the interdoublet shear and normal viscous coefficients. The geometric clutch model includes feedback from both curvature and sliding shear deformation [5], so it combines ideas from both the sliding control and curvature control models.

4.2. Single Filament Model

In this section, we develop the model for a single isolated filament in free space. The mechanochemical regulation mechanism is based on the sliding control model. Linearized solutions to models incorporating the sliding control mechanism have been studied previously [5,73]. Here, we consider the nonlinearities that occur from the coupling of dynein motor activity and flagellar shape, based on previous formulations [11, 66]. Our simulation differs from this prior work in two ways: (1) we model the fluid dynamics differently and (2) we incorporate the cell body into the simulation. For now, we start by analyzing a single isolated filament and the effects of the cell body will be discussed in a later section of this chapter.

In terms of the fluid model, the model in Oriola et al. [66] develops the nonlinear coupling of flagellar shape and dynein kinetics and their analysis is derived to allow large amplitudes, but they model the hydrodynamics using resistive force theory, which is valid in the small curvature limit. Chakrabarti and Saintillan [11] derive a similar set of nonlinear equations, where the hydrodynamics around the filament was modeled using slender body theory. Our approach is more closely aligned to that of Chakrabarti and Saintillan [11], but we instead model the fluid using the method of regularized Stokeslets [15]. This section develops the framework for the single filament mechanics within the context of the method of regularized Stokeslets.

We model the single flagellum as a filament bundle composed of two filaments subject to planar deformations, as pictured in Figure 4.1. The filaments have length L and are separated by a constant spacing of size a, where $a << L$. We define the centerline position of the flagellum as

$$\mathbf{X}(s,t) = (x(s,t), y(s,t), z(s,t)) \tag{4.12}$$

for arc length s and time t. The positions of each filament in the bundle are noted as $\mathbf{X}_{\pm}(s,t) = \mathbf{X} \pm (a/2)\hat{\mathbf{n}}$, where $\hat{\mathbf{n}}$ is the normal vector to the centerline. Often, we will refer to the tangent angle of the centerline rather than the position, where the tangent angle is $\phi(s,t)$. The position and tangent angle are related by

$$\mathbf{X}(s,t) = \mathbf{X}(0,t) + \int_0^s \big(\cos\phi(s',t), \sin\phi(s',t), 0\big)\, ds'. \tag{4.13}$$

Based on the method of regularized Stokeslets, as described further in Appendix A, we compute the velocity of the centerline of the filament using

$$\frac{\partial \mathbf{X}}{\partial t} = M\mathbf{F}, \tag{4.14}$$

where M is the mobility matrix for the method of regularized Stokeslets and $\mathbf{F}$ is the force along the filament. Since the beat is planar, instead of evolving $\mathbf{X}$, we evolve the tangent angle ϕ. To derive an expression for $\partial_t\phi$, take the time derivative of the unit tangent vector

$$\hat{\mathbf{t}} = \frac{\partial \mathbf{X}}{\partial s} = (\cos(\phi), \sin(\phi), 0).$$

Taking the time derivative of $\hat{\mathbf{t}}$, we find that

$$\frac{\partial}{\partial t}\hat{\mathbf{t}} = \frac{\partial}{\partial t}\frac{\partial}{\partial s}\mathbf{X} = (-\sin(\phi), \cos(\phi), 0)\frac{\partial \phi}{\partial t} = \hat{\mathbf{n}}\frac{\partial \phi}{\partial t},$$

where $\hat{\mathbf{n}}$ is the unit normal vector. Thus, we use Equation (4.14) and rewrite the equation of motion as

$$\hat{\mathbf{n}}\frac{\partial \phi}{\partial t} = \frac{\partial}{\partial t}\frac{\partial}{\partial s}\mathbf{X} = \frac{\partial}{\partial s}(M\mathbf{F}).$$

Simplifying both sides by taking the inner product with the normal vector, we find

$$\frac{\partial \phi}{\partial t} = \hat{\mathbf{n}} \cdot \frac{\partial}{\partial s}(M\mathbf{F}). \tag{4.15}$$

Now that we have described the filament shape evolution, to solve this equation for ϕ, we need to know the forces exerted on the filament. The forces have both passive and active contributions, and the sum of force densities is given as

$$\mathbf{F} = \mathbf{F}^b + \mathbf{F}^T + \mathbf{F}^m, \tag{4.16}$$

where $\mathbf{F}^b$ is the bending force density, $\mathbf{F}^T$ is the tension force density which maintains the inextensibility of the filament, and $\mathbf{F}^m$ is the active motor force density. These force densities are derived from the expressions for the energy functionals, similar to Camalet and Jülicher [9]. The energy functional is

$$\varepsilon = \int_0^L \frac{k_b}{2}(\kappa(s,t) - \kappa_0)^2 ds + \int_0^L \frac{\Lambda(s)}{2}\left\|\frac{\partial}{\partial s}\mathbf{X}(s,t)\right\|^2 ds + \int_0^L f(s,t)\Delta(s,t) ds, \tag{4.17}$$

where the first term accounts for the bending energy, the second term accounts for the inextensibility constraint via the tension of the filament, and the third term accounts for the energy from the active motors. Here, k_b is the bending stiffness, κ is the curvature of the filament, κ_0 is the base curvature of the filament, and L is the length of the filament. The tension $\Lambda(s)$ acts as a Lagrange multiplier; i.e. it is determined to enforce the inextensibility of the filament. Finally, the internal motor force density defined by the mechanochemical regulation mechanism $f(s,t)$ is defined in Equation (4.3) for the sliding control mechanism, and Δ is the sliding displacement defined in Equation (4.1). The force densities can be computed from the variational derivative of the energy functional in Equation

(4.17) as follows

$$\frac{\delta\varepsilon}{\delta\mathbf{X}}\tilde{\mathbf{X}} = -\int_0^L \mathbf{F}\tilde{\mathbf{X}}ds = -\int_0^L (\mathbf{F}^b + \mathbf{F}^T + \mathbf{F}^m)\tilde{\mathbf{X}}ds,$$

where $\mathbf{F}^b$, $\mathbf{F}^T$, and $\mathbf{F}^m$ are the force densities corresponding to bending, tension, and active motors, respectively. When we take this variational derivative, we have to take into account the boundary conditions of the filament. Here, we consider the boundary conditions of a free filament and consider other boundary conditions in a later section.

4.2.1. Non-Dimensionalization and Parameters. This model involves a large selection of parameters, many of which can be estimated directly from experiments based on *C. reinhardtii*. Table 4.1 lists these parameters along with a numerical value and description. Many of these parameters are provided in Oriola et al. [66], but the direct source of the experiment or calculation is listed in the table when possible.

From this list of parameters, we non-dimensionalize arc length by the length of the filament L and time by the characteristic time scale of dynein motor kinetics τ_0. The characteristic scale for internal force densities is given by the characteristic bending force density k_b/L^3. The scale for the internal motor force density is ρf_0 and the sliding displacement is scaled by the effective axoneme diameter a.

Non-dimensionalization of the governing equations results in the following dimensionless parameters, all of which have been defined previously by Oriola et al. [66]. We list the following non-dimensional parameters: the sperm number raised to the fourth power Sp^4, which compares

Parameter	Numerical Value	Description
μ	1-6 cP	Viscosity of the fluid [67]
a	200 nm	Effective diameter of the axoneme [23]
L	10 μm	Length of a *C. reinhardtii* flagellum [39]
k_b	4×10^{-22} N m^2	Range of bending rigidity for a *C. reinhardtii* flagellum [27]
K	2×10^3 N m^{-2}	Interdoublet elastic resistance measured for *C. reinhardtii* [63]
$\xi_\perp$	1.5×10^{-3} Pa s	Normal drag coefficient in viscosity 1 cP fluid for *C. reinhardtii* [3]
f_0	1-5 pN	Stall force for motor dynamics [41, 71]
f_c	0.5-2.5 pN	Characteristic unbinding force of the motors [42]
ν_0	5-7 μm/s	Motor velocity at zero load [42, 71]
ρ	10^3 motors μm^{-1}	Mean number density of motors [66]
τ_0	50 ms	Characteristic time scale of dynein motor kinetics [6, 42]
η	0.14	Dynein duty ratio $\frac{\pi_0}{\pi_0+\epsilon_0}$ - π_0 is binding, ϵ_0 is unbinding rate [42, 71]

TABLE 4.1. Numerical values and descriptions of dimensional parameters as reported experimentally.

the characteristic time scale of relaxation of a bending mode to the motor correlation time, where

$$\mathrm{Sp}^4 = L^4 \left(\frac{\xi_\perp}{k_b \tau_0} \right);$$

the measure of motor activity μ_a, which measures the strength of the motor force relative to the bending stiffness of the filament bundle, where

$$\mu_a = \frac{a \rho f_0 L^2}{k_b};$$

μ_b, which is the comparison of the elastic forces generated by nexin links from sliding to the characteristic bending forces

$$\mu_b = \frac{K a^2 L^2}{k_b};$$

and ζ, which is the ratio of the diameter of the entire filament and the characteristic displacement from the motor activity

$$\zeta = \frac{a}{\nu_0 \tau_0}.$$

The non-dimensional expression for internal motor force density is

$$f(s,t) = \mu_a(\overline{n} - \xi n' \Delta_t) - \mu_b \Delta, \tag{4.18}$$

where the numbers of motors on the top and bottom filaments in Figure 4.1 are represented by $\overline{n} = n_+ - n_-$ and $n' = n_+ + n_-$. The dimensionless motor evolution equation is

$$\frac{\partial n_\pm}{\partial t} = \eta(1 - n_\pm) - (1 - \eta) n_\pm \exp\left(\overline{f}(1 \mp \zeta \phi_t)\right), \tag{4.19}$$

where $\eta = \pi_0/(\pi_0 + \epsilon_0)$ is the duty ratio of the motors and $\overline{f}$ denotes the characteristic unbinding force [68]. These dimensionless parameters are all listed in Table 4.2, as previously defined [11,66].

Dimensionless number	Numerical value
$\mathrm{Sp} = L(\xi_\perp/k_b\tau_0)^{1/4}$	0.5 - 2.5
$\mu_a = a f_0 \rho L^2/k_b$	$0.5 - 3 \times 10^3$
$\mu_b = K a^2 L^2/k_b$	50-100
$\zeta = a/(v_0 \tau_0)$	0.4
$\overline{f} = f_0/f_c$	2

TABLE 4.2. Table listing the numerical values of the dimensionless parameters used in this paper, originally generated by [66].

We discuss the values of the parameters in Table 4.2 for *C. reinhardtii*. We first look at the range of sperm numbers $0.5 < \text{Sp} < 3$ based on the parameters in Table 4.1 for *C. reinhardtii*. If we calculate Sp using those in the table, we find $\text{Sp} \approx 1$. Since the normal drag coefficient $\xi_\perp$ is proportional to fluid viscosity μ, if we want to examine the viscosity range of our data, which is $1 < \mu < 6$ cP, then the corresponding sperm numbers are $1 < \text{Sp} < 1.57$. We expand this parameter regime and examine $0.5 < \text{Sp} < 2.5$ in Chapter 5. Similarly, if we compute the motor activity μ_a, depending on the value of the stall force, we find that $500 < \mu_a < 2500$ for the parameters for *C. reinhardtii*. Both sperm number Sp and motor activity μ_a values are lower than those explored in Oriola et al. [66] and Chakrabarti and Saintillan [11], as these studies examine parameter ranges for sperm rather than *C. reinhardtii*. The quantities for μ_b, ζ, and $\overline{f}$ are calculated in a similar fashion.

4.2.2. Discretization of the Model. We solve the system of governing equations numerically by discretizing the centerline filament arc length into N discrete nodes, separated by $N-1$ equal segments, or edges, of length $\Delta s = L/(N-1)$. We define the arc length s_j on the nodes, where $0 \le j \le N-1$. An example of the discretized filament is shown in Figure 4.2.

Elements on the nodes are notated with an integer subscript, and include the position of the filament $\mathbf{X}_j$ and the forces densities $\mathbf{F}_j$. We define different elements on the edges, which are notated with a half-integer subscript. These elements include the tangent angles $\phi_{j+\frac{1}{2}}$ and the unit

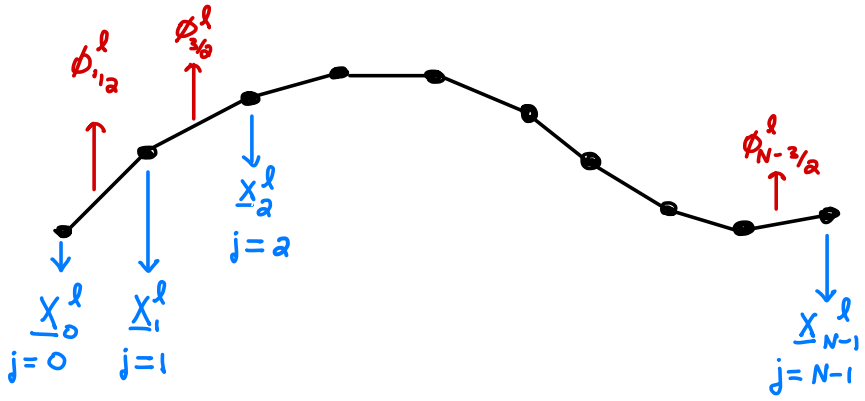

FIGURE 4.2. A discrete representation of the filament centerline, as shown in the discrete position given in Equation (4.2.2). The filament has N nodes, where the positions $\mathbf{X}_j^\ell$ are defined, where the subscript j is the node index, and the superscript ℓ is the index for the timestep, where $t^\ell = \ell \Delta t$. The filament has $N-1$ edges between the nodes, where the tangent angles $\phi^\ell_{j+\frac{1}{2}}$ are defined.

normal and tangent vectors $\hat{\mathbf{n}}_{j+\frac{1}{2}}$ and $\hat{\mathbf{t}}_{j+\frac{1}{2}}$. The forward difference operator D_+ maps quantities from edges to nodes and the backwards difference operator D_- maps quantities from nodes to edges.

We discretize time by $\Delta t = T/(N_t - 1)$, where T is the length of time we run the simulation for and N_t is the number of discrete time points. We represent a discrete time $t^\ell = \ell \Delta t$, and a superscript represents the temporal index. For example, the position of the filament at the arc length s_j and time t^ℓ is $\mathbf{X}_j^\ell$. Thus, the discrete representation of the position of the filament using tangent angles is

$$\mathbf{X}_j^\ell = \mathbf{X}_0^\ell + \Delta s \sum_{k=0}^{j} \left(\cos \phi_{k+\frac{1}{2}}^\ell, \sin \phi_{k+\frac{1}{2}}^\ell, 0 \right).$$

4.2.3. Discretizing Force Densities. In our simulation, we find the force densities from the energy functionals by taking the discrete variational derivative. We review this process below.

4.2.3.1. *Bending Force Density.* The bending energy functional is defined as

$$\varepsilon^b = \frac{k_b}{2} \int_0^L (\kappa - \kappa_0)^2 ds,$$

where k_b is the bending stiffness, κ is the curvature of the flagellum, and κ_0 is the prescribed target curvature. In the discrete model with free ends, bending only occurs at interior points, and thus, the discrete bending energy is

$$E^b = \frac{k_b}{2} \sum_{j=2}^{N-1} (\kappa_j - \kappa_{0_j})^2 \Delta s.$$

We compute the discrete variational derivative and find that the discrete bending force density, written in terms of tangent angle ϕ is given as:

$$\mathbf{F^b}_k = k_b \Delta s^2 \left[-(\kappa_{k+1} - \kappa_{0_{k+1}}) \hat{\mathbf{n}}_{k+\frac{1}{2}} + (\kappa_k - \kappa_{0_k})(\hat{\mathbf{n}}_{k-\frac{1}{2}} + \hat{\mathbf{n}}_{k+\frac{1}{2}}) - (\kappa_{k-1} - \kappa_{0_{k-1}}) \hat{\mathbf{n}}_{k-\frac{1}{2}} \right]$$

for $k = 2, \ldots, N-3$ at the interior points. The edge terms can be defined appropriately given boundary conditions. At the edge points for $k = N-2, N-1$, considering free boundary conditions, the bending force density is defined as

$$\begin{aligned} \mathbf{F^b}_{N-2} &= k_b \Delta s^2 \left[(\kappa_{N-2} - \kappa_{0_{N-2}})(\hat{\mathbf{n}}_{N-\frac{5}{2}} + \hat{\mathbf{n}}_{N-\frac{3}{2}}) - (\kappa_{N-3} - \kappa_{0_{N-3}}) \hat{\mathbf{n}}_{N-\frac{5}{2}} \right] \\ \mathbf{F^b}_{N-1} &= -k_b \Delta s^2 (\kappa_{N-2} - \kappa_{0_{N-2}}) \hat{\mathbf{n}}_{N-\frac{3}{2}}. \end{aligned}$$

The edge points at indices $k = 0, 1$ are defined similarly. Note the force densities are defined on the nodes of the discrete filament. These forces and energies are at a fixed point in time, but the temporal indexing is left out for clarity.

4.2.3.2. *Active Motor Force Density.* The energy functional from active motor stresses [9] is given by

$$\varepsilon^m = \int_0^L \Delta(s,t) f(s,t) ds$$

where f is the internal motor force density and the sliding displacement $\Delta(s,t)$ is defined in Equation (4.1). In the discretization, we define the tangent angle and the internal motor force density on the edges, and the position of the filament is defined on the nodes, as represented on the filament in Figure 4.2. Thus, the sliding displacement is also defined on the edges. We define the discretization:

$$\varepsilon^m = \sum_{j=0}^{N-2} \Delta_{j+\frac{1}{2}} f_{j+\frac{1}{2}} \Delta s.$$

Then, we take the discrete variational derivative to find the motor force density. Assuming the variational derivative of f is 0:

$$\begin{aligned}
\mathbf{F^m}_0 &= -a \left[\left(-\frac{\delta \phi_{\frac{1}{2}}}{\delta \mathbf{X}_0} \right) \sum_{j=1}^{N-2} f_{j+\frac{1}{2}} \right] \\
\mathbf{F^m}_1 &= -a \left[\frac{\delta \phi_{\frac{3}{2}}}{\delta \mathbf{X}_1} f_{\frac{3}{2}} - \frac{\delta \phi_{\frac{1}{2}}}{\delta \mathbf{X}_1} \sum_{j=1}^{N-2} f_{j+\frac{1}{2}} \right] \\
\mathbf{F^m}_k &= -a \left[f_{k-\frac{1}{2}} \frac{\delta \phi_{k-\frac{1}{2}}}{\delta \mathbf{X}_k} + f_{k+\frac{1}{2}} \frac{\delta \phi_{k+\frac{1}{2}}}{\delta \mathbf{X}_k} \right], \qquad k = 2, \ldots, N-2 \\
\mathbf{F^m}_{N-1} &= -a \left[f_{N-\frac{1}{2}} \frac{\delta \phi_{N-\frac{1}{2}}}{\delta \mathbf{X}_{N-1}} \right].
\end{aligned}$$

The variational derivative of the tangent angle is given as follows:

$$\frac{\delta \phi_{j+\frac{1}{2}}}{\delta \mathbf{X}_k} = \begin{cases} \frac{1}{\Delta s} \hat{\mathbf{n}}_{j+\frac{1}{2}}, & k = j+1 \\ -\frac{1}{\Delta s} \hat{\mathbf{n}}_{j+\frac{1}{2}}, & k = j \\ 0, & \text{otherwise} \end{cases},$$

where $\hat{\mathbf{n}}_{j+\frac{1}{2}}$ is the unit normal vector. In our simulation, we define the motor force density f using the sliding control model, as shown in Equation (4.3) and defined by [9, 66].

4.2.3.3. *Inextensibility / Tension Force.* We consider filaments in this model that can bend but cannot stretch as they evolve in time. From the variation of the energy functional

$$\varepsilon^T = \int_0^{:} \frac{\Lambda}{2} \left\| \frac{\partial}{\partial s} \mathbf{X}(s,t) \right\|^2 ds,$$

we can derive the tension force density

$$\mathbf{F}^T = \frac{\partial}{\partial s} \left(\Lambda \frac{\partial \mathbf{X}}{\partial s} \right).$$

We solve for the Lagrange multiplier Λ by enforcing the inextensibility constraint on the filament [61]

$$\frac{\partial \mathbf{X}}{\partial s} \cdot \frac{\partial \mathbf{X}}{\partial s} = 1. \tag{4.20}$$

We can define $\dfrac{\partial \mathbf{X}}{\partial s} = \mathbf{T}$ as the tangent vector, so our constraint can also be written as

$$\mathbf{T} \cdot \mathbf{T} = 1.$$

If $\mathbf{T}$ satisfies this condition, $\mathbf{T} = \hat{\mathbf{t}}$, the unit tangent vector. We can discretize both the tension force density and the constraint in space as

$$\begin{aligned} \mathbf{F}^T &= D_+ \left(\Lambda \mathbf{T} \right) \\ \mathbf{T} \cdot \mathbf{T} &= 1. \end{aligned}$$

In order to solve for the Lagrange multiplier Λ, we consider the evolution equation of the filament, from Equation (4.14). We rewrite that equation, discretized in space, as

$$\frac{\partial \mathbf{X}}{\partial t} = M \left(\mathbf{F}^\star(\mathbf{X}) + D_+(\Lambda \mathbf{T}) \right), \tag{4.21}$$

where $\mathbf{F}^\star = \mathbf{F}^b + \mathbf{F}^m$, the summation of the bending and motor force densities as defined in the previous subsections and the mobility M is defined using the method of regularized Stokeslets [15]. If we consider the discrete constraint

$$D_- \mathbf{X} \cdot D_- \mathbf{X} = 1,$$

and differentiate this constraint with respect to time, we get the equation

$$2(D_-\mathbf{X}) \cdot \left(D_- \frac{\partial \mathbf{X}}{\partial t} \right) = 0.$$

Now, if we apply a discrete spacial derivative D_- to Equation (4.21), we get

$$D_- \frac{\partial \mathbf{X}}{\partial t} = D_- M \mathbf{F}^\star(\mathbf{X}) + D_- M D_+ \left(\Lambda \mathbf{T} \right).$$

Taking the inner product of both sides with $D_-\mathbf{X} = \mathbf{T}$, we can apply the constraint and rearrange, which results in the following equation which we can use to solve for Λ,

$$\mathbf{T} \cdot D_- M D_+(\mathbf{T}\Lambda) = -\mathbf{T} \cdot D_- M \mathbf{F}^\star(\mathbf{X}). \tag{4.22}$$

4.2.4. Implementing Boundary Conditions on the Filament. Throughout the previous subsections, we have discussed implementing the forces on a free filament. In this subsection, we discuss how we impose clamped boundary conditions on the fixed end of the filament while the opposite end remains free. At the clamped end, both the tangent angle $\phi_{\frac{1}{2}}$ and the position $\mathbf{X}_0$ are fixed in time.

We consider the general evolution equation of the position of the filament, as described in Equation (4.14), where

$$\mathbf{U} = M\mathbf{F}$$

for all points $\mathbf{X}_j$, $0 \leq j \leq N-1$ along the filament. Since we have a clamped filament, $\mathbf{X}_j, j = 0, 1$ are fixed. This means that

$$\mathbf{U}_j = 0 \text{ for } j = 0, 1.$$

In order to enforce this constraint, we introduce $\mathbf{F}_p$, the force density which pins the first two points in place and is defined on $\mathbf{X}_j, j = 0, 1$. We also introduce the force density on the free points $\mathbf{F}_f$, defined at $\mathbf{X}_j$, $3 \leq j \leq N-1$, which is the force density computed in the previous subsections from Equation (4.16).

We know the force densities on the free points $\mathbf{F}_f$ as computed previously, and we are imposing the zero velocity at the pinned points in order to enforce the clamped boundary condition. Thus, we need to solve for the pinned forces $\mathbf{F}_p$, as well as the velocities at the free points. The resulting

system takes the following form, where p indicates pinned points and f denotes a free point:

$$\begin{bmatrix} M_{pp} & M_{pf} \\ M_{pf}^T & M_{ff} \end{bmatrix} \begin{bmatrix} \mathbf{F}_p \\ \mathbf{F}_f \end{bmatrix} = \begin{bmatrix} \mathbf{U}_p \\ \mathbf{U}_f \end{bmatrix}.$$

The velocity at the pinned points $\mathbf{U}_p$ is zero, and we have computed the forces at the free points $\mathbf{F}_f$ as seen in Equation (4.16). To obtain the velocities at the free points $\mathbf{U}_f$, given that $\mathbf{U}_p = 0$, we solve the following system:

$$\mathbf{U}_f = (M_{ff} - M_{pf}^T M_{pp}^{-1} M_{pf})\mathbf{F}_f. \tag{4.23}$$

This yields the velocity at all points along the filament.

4.2.5. Summary. The previous subsections provide a complete description of the setup for the single filament simulation. We conclude this section with a summary of the required equations to solve for the shape of the filament immersed in fluid.

The evolution equation for the shape of the filament in terms of tangent angles ϕ is

$$\frac{\partial \phi}{\partial t} = \hat{\mathbf{n}} \cdot \frac{\partial}{\partial s} \begin{bmatrix} \mathbf{U}_p \\ \mathbf{U}_f \end{bmatrix}, \tag{4.24}$$

where the velocities on the pinned points are $\mathbf{U}_p = \mathbf{0}$ and the velocities on the free points are $\mathbf{U}_f$. We solve for the motor configurations simultaneously using `ode15i`, solving the evolution equation

$$\frac{\partial n_\pm}{\partial t} = \eta(1 - n_\pm) - (1 - \eta) n_\pm \exp\left(\overline{f}(1 \mp \zeta \phi_t)\right). \tag{4.25}$$

We compute the velocities on the free points from the force densities on the filament using the method of regularized Stokeslets. We implement clamped boundary conditions as described in Section 4.2.4, which results in the following equation for the free velocities

$$\mathbf{U}_f = (M_{ff} - M_{pf}^T M_{pp}^{-1} M_{pf})\mathbf{F}_f.$$

In this equation, $\mathbf{F}_f$ is the force density on the free points, which is

$$\mathbf{F}_f = \mathbf{F^b} + \mathbf{F^T} + \mathbf{F^m},$$

where $\mathbf{F^b}$ is the bending force density described in Section 4.2.3.1, $\mathbf{F^T}$ is the tension force density as computed through an inextensibility constraint in Section 4.2.3.3, and $\mathbf{F^m}$ is the motor force density, as described in Section 4.2.3.2. All of these force densities are dependent on the tangent angle ϕ, but the motor force density also depends on motor configurations $n_\pm$ as well as the time derivative of tangent angle ϕ_t. For the model of the motor force density, we use the sliding control mechanism, as described in Section 4.1.1. The non-dimensional internal force density $f(s,t)$ for the sliding control mechanism in Oriola et al. [66] is explicitly derived from Equations (4.2)-(4.3) as

$$f(s,t) = \mu_a(\overline{n} - \zeta n' \phi_t) - \mu_b \left(\phi - \phi_0 - \kappa_0 s + \frac{\Delta_0}{a} \right),$$

where $\overline{n} = n_+ - n_-$, $n' = n_+ + n_-$, ϕ_0 is the base tangent angle, κ_0 is the constant resting curvature, and Δ_0 is the sliding displacement at the base of the flagellum. This internal force density and its parameters are described further in Section 4.2.1.

4.3. Tests for the Single Filament Model

For the implementation of the single filament model, we solve for the filament shape using Equation (4.24) and for the motor dynamics using Equation (4.19). We solve these equations simultaneously with MATLAB's implicit ODE solver `ode15i`.

We assign initial conditions for the tangent angle ϕ and bound motor populations $n_\pm$, since these are the quantities evolved by the PDEs. We specify an initial tangent angle configuration $\phi^0_{j+\frac{1}{2}}$, $0 < j < N-2$, either by prescribing a small wave, or by using the final tangent-angle configuration from a previous simulation. We also provide an initial state for the bound motors, chosen either as a constant value or one taken from the final state of another simulation. Finally, since we use an implicit solver, we must also supply an initial value for the time derivative. To obtain the initial value of $\partial_t \phi(s,0)$, we first compute an initial guess by evaluating the derivative in the absence of active motor forces. Then, we solve for the initial derivative, now including active motor forces, using `fsolve`. We set $\partial_t n_\pm(s,0) = 0$.

In this section, following Oriola et al. [66] and Chakrabarti and Saintillan [11], we explore the parameter space defined by the sperm number Sp and motor activity μ_a, and we identify the various resulting dynamical transitions and beating patterns. Additionally, we perform a refinement study across different spatial discretizations of the mesh of the filament.

4.3.1. Examining the Emergent Beat. In this section, we examine our model and confirm that, for sufficiently high motor activity, the filament exhibits beating. We fix the sperm number $\mathrm{Sp} = 1$, and vary the motor activity μ_a between 500, 1500, and 2500. The number of points along the filament is set to $N = 101$. We initialize the simulation with a perturbed filament, where the initial discrete tangent angle is

$$\phi^0_{j+\frac{1}{2}} = 10^{-3}\left[\sin(3\pi s^*_{j+\frac{1}{2}}) + 3\pi\cos(3\pi s^*_{j+\frac{1}{2}})\right], \tag{4.26}$$

where $s^*_{j+\frac{1}{2}} = s_j + \frac{1}{2}\Delta s$ for $0 \le j \le N-2$ denotes the arc length defined on the edges of the discrete filament. We initialize the simulation with this perturbation of the filament, and set the initial bound motor state to the constant value

$$n^0_{\pm} = \frac{\eta}{\eta + (1-\eta)\overline{f}},$$

where $\eta = 0.14$ and $\overline{f} = 2$. The other parameters are set to $\mu_b = 90$ and $\zeta = 0.4$. For each of these simulations, we run the system long enough for the filament to settle into a steady state, whether that be a static configuration or an oscillatory beat. To visualize this behavior, Figure 4.3 shows the kymographs of the tangent angles for varying motor activity $\mu_a = 500, 1500, 2500$. In Figure 4.3a, the plot is one color, except at the initial transient, indicating that no beat emerges. In contrast, Figures 4.3b-c reveal oscillatory motion. As can be seen by examining the color bar, the amplitude of the beat is larger in Figure 4.3c, and it seems that the amplitude of the beat increases with motor activity μ_a.

Figure 4.4 shows the emergent waveforms from Figure 4.3 for $\mu_a = 500, 1500, 2500$. The colors in each plot represent one full period of the beat. In Figure 4.4b, the waveform is very flat and exhibits very small curvature. Figure 4.4c shows a waveform with greater curvature and larger amplitude for a higher motor activity.

Since our simulation produces stable oscillatory beating patterns for sufficiently high motor activity μ_a as shown in Figures 4.3-4.4, we next observe if the simulation is consistent across different filament discretizations.

4.3.2. Refinement Studies. We perform a refinement study for the mesh along the filament. For this test, we fix the regularization parameter ϵ in the method of regularized Stokeslets [15]. This regularization is tied to the physical width of the filament, and because we typically scale the

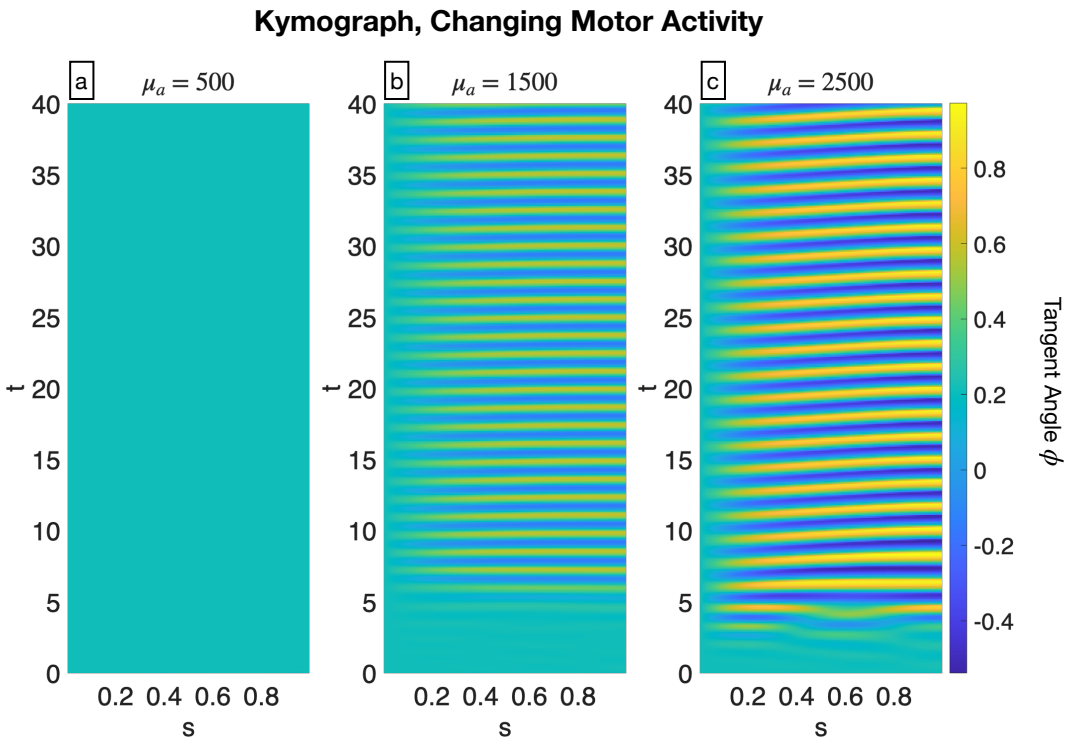

FIGURE 4.3. Kymograph of tangent angle amplitude for single filament simulations, with arc length s horizontally and time t vertically. All simulations share the same initial conditions and parameters Sp $= 1$, $\mu_b = 90$, $\zeta = 0.4$, $\eta = 0.14$, $\overline{f} = 2$. Shown are kymographs for (a) $\mu_a = 500$, no beat; (b) $\mu_a = 1500$, emergent periodic beat; (c) $\mu_a = 2500$, higher amplitude periodic beat.

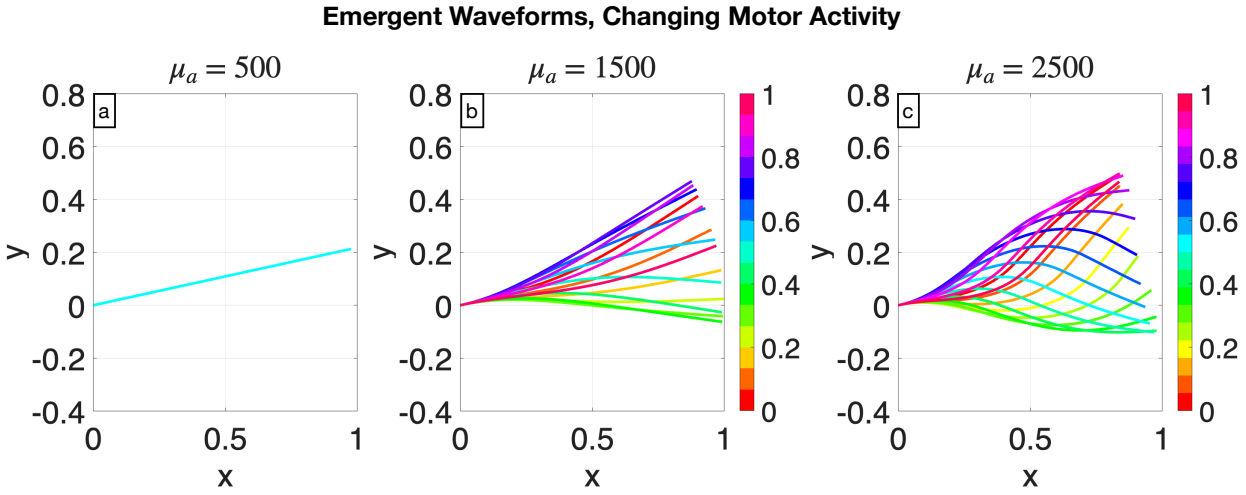

FIGURE 4.4. Emergent waveforms from single filament simulations at different motor activities μ_a. All panels use identical initial conditions and parameters Sp $=$ 1, $\mu_b = 90$, $\zeta = 0.4$, $\eta = 0.14$, $\overline{f} = 2$. Shown are waveforms for (a) $\mu_a = 500$, no beat; (b) $\mu_a = 1500$, flat emergent periodic beat; (c) $\mu_a = 2500$, higher amplitude periodic beat.

regularization with the grid spacing, changing the number of discretization points would otherwise change the effective thickness of the filament and thus alter the fluid dynamics. For this reason, for these experiments we fix $\epsilon = 0.001$. We begin with the same initial tangent angle configuration ϕ^0 from Equation (4.26) and the same initial conditions for $n_\pm$. The remaining parameters are set to Sp $= 1$, $\mu_a = 2000$, $\mu_b = 90$, and $\zeta = 0.4$. We then examine the tangent angle kymographs for this scenario using different numbers of discretization points $N = 51, 101$, and 201, shown in Figure 4.5. Visually, the kymographs appear nearly identical, with the length of the period of the emergent beat is very similar across all discretizations. In the title of each subfigure, we list the first six digits of the emergent period T, and we observe variation only beginning in the fourth digit. The period is shown dimensionally, re-dimensionalized using τ_0. These results indicate that our simulation is consistent across this range of discretizations.

Additionally, we show convergence using a refinement study for the final tangent angles ϕ and the final motor configurations $n_\pm$. This refinement study spans discretizations from $N = 51$ discretization points to $N = 801$ points. We compare the final values of the tangent angle ϕ and motor configurations $n_\pm$ for consecutive discretizations, by computing the two norm relative difference of these quantities at time $t = 40$ in the simulation. These values are shown in Table 4.6. We note that all of these quantities were found by solving the evolution equations using the implicit ODE solve `ode15i`, where the relative time tolerance was set to 10^{-3}. For all of the resolutions except for the finest grid, the relative spatial error in Table 4.6 looks to on the order of 10^{-2} for n_+ and 10^{-1} for ϕ and n_-, and thus we fix the relative time tolerance at 10^{-3} for all simulations. For the finest resolution, the temporal error may dominate at this resolution. As we increase the number of mesh discretization points, we see that the relative differences for the final tangent angles ϕ and the final motor configurations $n_\pm$ decrease and the simulation appears to be converging. In particular, we note that as we go from the second to the third row of Table 4.6, our relative differences all seem to cut approximately in half, which is a sign of first order convergence.

Therefore, we find that the simulation yields consistent results across different discretizations, as seen in Figure 4.5 and Table 4.6. We next compare the results of this simulation with those from previous studies.

4.3.3. Stability Curves. We compare our results with the previous work of Oriola et al. [66] and Chakrabati and Saintillan [11] for the case of an isolated clamped filament. Both studies

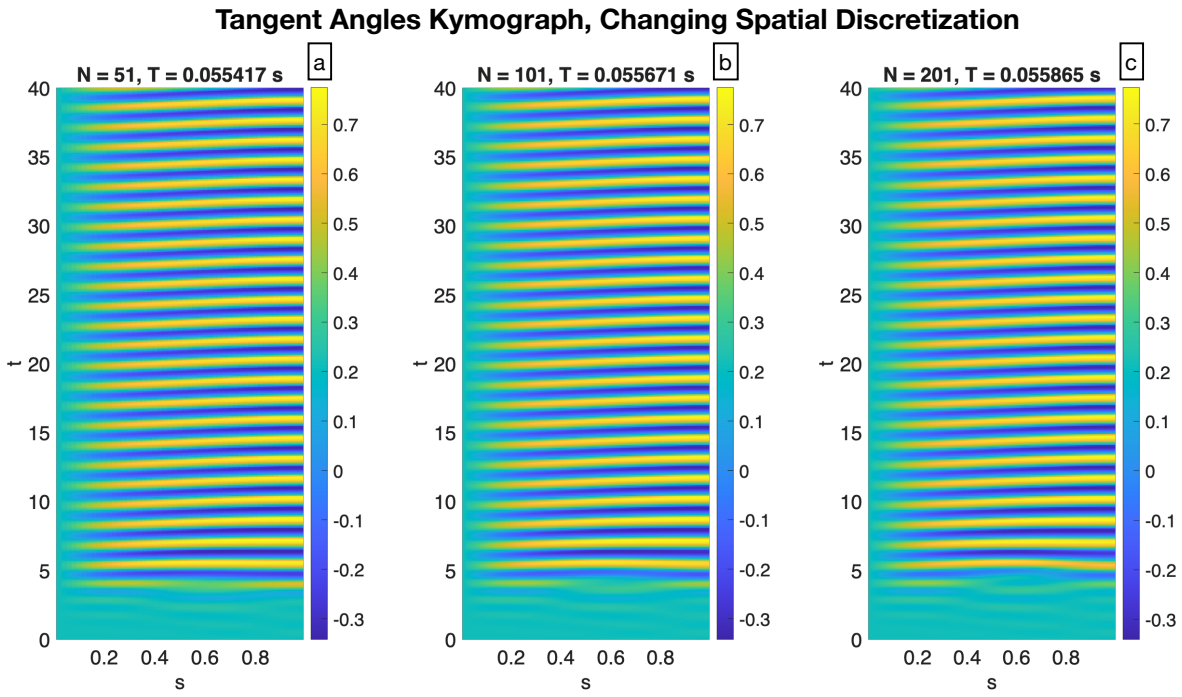

FIGURE 4.5. Kymograph of tangent angle amplitude for single filament simulations, with arc length s horizontally and time t vertically. All simulations share the same initial conditions and parameters Sp $= 1$, $\mu_a = 2000$, $\mu_b = 90$, $\zeta = 0.4$, $\eta = 0.14$, $\overline{f} = 2$. Shown are kymographs different spatial discretizations with (a) $N = 51$ and period $T = 0.055417$ s; (b) $N = 101$ and period $T = 0.055671$ s; (c) $N = 201$ and period $T = 0.055865$ s.

No. points j	No. Points k	$\frac{\left\|\phi^j - \phi^k\right\|_2}{\left\|\phi^k\right\|_2}$	$\frac{\left\|n_+^j - n_+^k\right\|_2}{\left\|n_+^k\right\|_2}$	$\frac{\left\|n_-^j - n_-^k\right\|_2}{\left\|n_-^k\right\|_2}$
51	101	0.2987	0.1156	0.4943
101	201	0.2084	0.0876	0.3490
201	401	0.1068	0.0461	0.1565
401	801	0.0007	0.0005	0.0012

FIGURE 4.6. Comparing the tangent angle ϕ and motor configurations on the top + filament and bottom - filament $n_\pm$ at the final time step for different discretizations of the filament. We compare the mesh with of consecutive numbers of discretization points. For each quantity, we compute the comparison via a relative two norm difference. As we increase the mesh spacing, this quantity decreases.

perform stability analysis, showing that, for a given sperm number Sp, there exists a critical motor activity level $\mu_a^\star$ above which the filament undergoes a Hopf bifurcation. Above the bifurcation, the filament begins to oscillate. Oriola et al. [66] perform this stability analysis using local resistive force theory [32], whereas Chakrabarti and Saintillan carry out this analysis using nonlocal slender body theory [38]. Thus, the instability thresholds predicted by the two studies differs quantitatively. Beyond differences in the fluid model, the other parameters, particularly μ_b and ζ, differ between the two models. The stability diagrams appear in Figure 2c in Oriola et al. [66] and Figure 4 in Chakrabarti and Saintillan [11]. We reproduce their figures on the same plot in Figure 4.7a. Below the two curves, there is no instability and the filaments from both studies do not beat. Above the curves, in the pink shaded region, traveling waves propagate down the filament in both studies. Between the two curves, in the blue shaded region, the filament in the fluid modeled by slender body theory from Chakrabarti and Saintillan [11] has emergent oscillatory motion, but the filament in the fluid modeled by resistive force theory from Oriola et al. [66] does not.

Since we model the fluid dynamics using the method of regularized Stokeslets, a different method than both Oriola et al. [66] and Chakrabarti and Saintillan [11], we compare the stability curve with those in Figure 4.7a under the same parameter regime, where sperm number varies between $7 < \text{Sp} < 12$ and motor activity varies between $1000 < \mu_a < 8000$. In our simulations, the other parameters $\mu_b = 50$, $\zeta = 0.4$, $\eta = 0.14$, and $\overline{f} = 2$ are set to match Oriola et al. [66]. The parameters for the stability curve from Chakrabati and Saintillan [11] vary slightly from these parameters.

To compute the stability curve, we run the simulations until the filament reaches a steady state. For low motor activities μ_a, the filament stops moving and no beat emerges. For higher motor activities, the filament settles into a periodic oscillatory beat. We look at the activity of the filament after the steady state. If we run the simulation until time T^*, then we compute the average bending energy across the time interval $[T^*/2, T^*]$ discretely. We do this by computing the square of the discrete two-norm of the curvature $\sum_j (\kappa(s_j, t^\ell))^2$. Then we average this across time for the given interval. When oscillatory beating occurs, the bending energy is nonzero, whereas when no beat emerges, the filament settles into a flat configuration and the bending energy is zero.

We compute these stability curves for two different models of the fluid, as is shown in Figure 4.7b. The first is for the method of regularized Stokeslets [15], where the simulation is set up

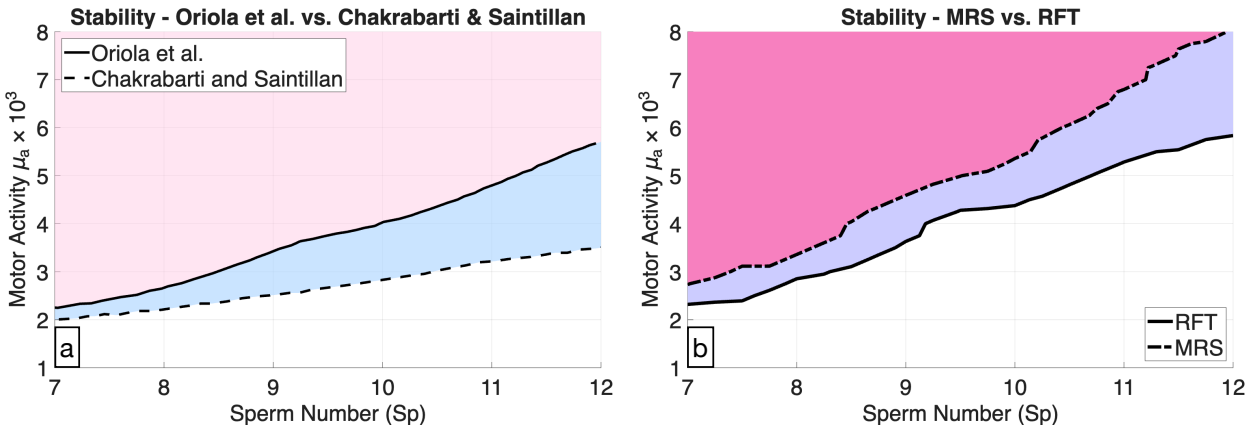

FIGURE 4.7. Stability curves for a clamped filament, for Sperm number Sp between $7 < \text{Sp} < 12$ and motor activity $1000 < \mu_a < 8000$. (a) Stability curves reproduced from Oriola et al. [66] and Chakrabarti and Saintillan [11]. The solid line is obtained from the stability curve found in Figure 2c in Oriola et al. [66] using resistive force theory and the dashed line is obtained from the stability curve found in Figure 4 in Chakrabarti and Saintillan [11]. Below both curves, there is no instability and the filament does not beat in both models. Above both curves in the light pink shaded region, the filament has an emergent oscillatory beat in both models. In the blue shaded region between the two curves, the filament from the simulation in Chakrabarti and Saintillan [11] has emergent oscillatory motion, but the filament from the simulation in Oriola et al. [66] does not. (b) Stability curves produced using the model described in Section 4.2. The solid line is the stability curve found using resistive force theory (RFT) and the dashed line is the stability curve found using the method of regularized Stokeslets (MRS). Below the curves, there is no instability and no beating. Between the curves, in the purple region, there is emergent motion for the filament immersed in the fluid modeled by RFT, not MRS. Above both curves, in the purple region, both filaments have oscillatory motion. The curves represent Hopf bifurcations.

exactly as is described in Section 4.2. The stability curve computed using the method of regularized Stokeslets is the dashed curve in Figure 4.7b. Second, we compute the stability curve when modeling the fluid using local resistive force theory [32], similar to Oriola et al. [66]. This changes the mobility matrix M found throughout our simulations, particularly in Equation 4.24. We form the mobility tensor M_{RFT} [32] as

$$M_{RFT} = \xi_{\parallel}\hat{\mathbf{t}}\hat{\mathbf{t}} + \xi_{\perp}\hat{\mathbf{n}}\hat{\mathbf{n}}.$$

Once we non-dimensionalize this tensor by the viscous time scale $[L^4(\xi_{\perp} + \xi_{\parallel})]/k_b$, we find that

$$M_{RFT} = \mathcal{R}\hat{\mathbf{t}}\hat{\mathbf{t}} + \hat{\mathbf{n}}\hat{\mathbf{n}},$$

where $\mathcal{R} = \xi_{\parallel}/\xi_{\perp}$ is the ratio of tangential and normal drag coefficients. Thus, we simply replace M_{RFT} where we have the mobility tensor M in previous equations, specifically in Equation (4.24).

To compute the value of $\mathcal{R}$, we calculate the tangential and normal drag coefficients $\xi_{\parallel}$ and $\xi_{\perp}$ using the method of regularized Stokeslets. To calculate these values, we take a horizontal, flat, filament of length 1. We assign a unit velocity to each point on the filament. For the tangential drag coefficient calculation, the unit velocity is parallel to the filament, $U_x = [1, 0, 0]$. For the normal drag coefficient, the unit velocity is orthogonal to the filament, $U_y = [0, 1, 0]$. We then use the method of regularized Stokeslets mobility matrix M, and solve for the forces using the force-velocity relationship $U = MF$, where the fluid viscosity is set to $\mu = 1$ cP. Then, we can calculate the drag coefficients

$$\xi_{\parallel} = \frac{F_x^{\text{net}}}{LU_x^{\text{net}}} \text{ and } \xi_{\perp} = \frac{F_y^{\text{net}}}{LU_y^{\text{net}}},$$

where L is the length of the filament, which we have set to 1. From this calculation, we find that

$$\xi_{\parallel} = 1.2561 \text{ and } \xi_{\perp} = 2.0118.$$

We can then calculate $\mathcal{R}$ as

$$\mathcal{R} = \frac{\xi_{\parallel}}{\xi_{\perp}} = 0.6243.$$

We use this value of $\mathcal{R}$ for the resistive force theory simulations used to generate the stability curve in Figure 4.7b. We calculate $\mathcal{R}$ in this manner in order to try to maintain consistency between the simulations where the fluid is modeled with resistive force theory and the method of regularized Stokeslets.

The stability curve computed using resistive force theory is the solid curve in Figure 4.7b. In this figure, in the empty region, neither filament beats and there is no instability. In the pink region above the curves, there is emergent oscillatory beating for filaments in both cases. In the purple shaded region between the two curves, the filament in a fluid modeled by resistive force theory has emergent oscillatory motion, and the filament in a fluid modeled by the method of regularized Stokeslets does not.

The stability curve obtained using the method of regularized Stokeslets in Figure 4.7b appears at higher motor activity μ_a levels than the curve obtained using resistive force theory, and has a steeper slope. It also lies above the stability curve reported for slender body theory [11]. The

stability curve obtained using resistive force theory in Figure 4.7b closely resembles that of the curve in Oriola et al. [66] and reproduced in Figure 4.7a, as expected, since their study also models the fluid dynamics of the system using resistive force theory. This agreement between curves demonstrates that the choice of hydrodynamic model affects the location of the stability boundary, meaning the precise quantitative results of the simulation depend on the framework of the model. However, regardless of the method which we model the fluid dynamics, we consistently observe that for a given sperm number Sp, there exists a critical motor activity level $\mu_a^\star$ at which the filament undergoes a Hopf bifurcation and oscillatory beating emerges. Based on these observations, we proceed using the method of regularized Stokeslets to model the fluid. In the next section, we incorporate the isolated filament model developed here into a full swimming simulation for a model *C. reinhardtii* cell.

4.4. Swimming Simulation

In this section, we describe how we incorporate the active filament model in Section 4.2 into a full swimming simulation for a model *C. reinhardtii* cell. The geometry of the swimming cell is the same as that from the simulation in Section 3.2.1, except that the kinematics are now emergent from the motor model rather than prescribed. For this simulation, we discretize the cell body using 900 grid points, again using maximum determinant points on a sphere [79]. This gives a spacing of $\Delta s = 0.0833$. We only use a single mesh on the body for this simulation, in contrast to the model presented in Section 3.2. The other geometric details of the cell body, such as the radii and flagellar attachment angles, remain the same as in Chapter 3. We solve for the emergent beat of the right flagellum only, while the dynamics of the left flagellum are obtained via reflection to ensure synchronous beating of the two filaments, consistent with our dataset [67]. In this section, we describe the algorithm for the simulation with the fully swimmer and examine emergent waveforms from the simulation.

4.4.1. Algorithm. To solve the evolution equations in this simulation, we do not use a built in `MATLAB` ODE solver, as we did in the single filament case. Instead, we alternately update the motor configuration and filament shape in each time step using backwards Euler's method. In addition to solving for the evolution of the filament shape via tangent angles ϕ and the motor

configurations $n_\pm$, we also solve for the reference position of the cell $\mathbf{X_T}$. Note that $\mathbf{X_T} \in \mathbb{R}^3$ uses the same notation as in Chapter 3 for the reference position of the cell body.

For the ℓ-th time step in the simulation, we start by solving for $n_\pm^\ell$ using a backwards Euler implementation of the motor configuration evolution from Equation (4.25):

$$\frac{n_\pm^\ell - n_\pm^{\ell-1}}{\Delta t} = \eta(1 - n_\pm^\ell) - (1-\eta) n_\pm^\ell \exp(\overline{f}(1 \mp \zeta \phi_t^{\ell-1})). \tag{4.27}$$

Note that the time derivative of the tangent angle ϕ_t is fixed at the previous time step $t^{\ell-1}$. After we find $n_\pm^\ell$, at time t^ℓ, we solve for the tangent angle ϕ^ℓ, using a backwards Euler implementation of Equation (4.24), as well as solve for ${\mathbf{X_T}}^\ell$

$$\frac{\phi^\ell - \phi^{\ell-1}}{\Delta t} = \hat{\mathbf{n}}^\ell \cdot D_- \mathbf{U}^\ell \tag{4.28}$$

$$\frac{{\mathbf{X_T}}^\ell - {\mathbf{X_T}}^{\ell-1}}{\Delta t} = {\mathbf{U_T}}^\ell. \tag{4.29}$$

Solving for ϕ^ℓ and ${\mathbf{X_T}}^\ell$ in Equations (4.28)-(4.29) requires the use of a nonlinear solver, as the right hand sides of these equations depend on those quantities. Additionally, due to the geometry of the swimmer, we impose realistic constraints on the solution to ensure that the two flagella do not cross, nor do they enter the cell body. Thus, to solve Equations (4.28)-(4.29) for ϕ^ℓ and ${\mathbf{X_T}}^\ell$, we implement `fmincon` with constraints to solve for the tangent angles ϕ and body reference point $\mathbf{X_T}$. We set the dummy objective function in `fmincon` to be identically zero and move our system of equations into the constraints of `fmincon`. This procedure functions similarly to `MATLAB`'s standard nonlinear solver `fsolve`, but allows us to add the extra physical nonlinear constraints.

In order to solve Equations (4.28)-(4.29), we compute the velocity on the free points of the flagellum in the fixed body frame $\mathbf{U}^\ell$ and the translational velocity ${\mathbf{U_T}}^\ell$. For the velocity on the free points of the flagellum in the fixed body frame $\mathbf{U}^\ell$, we use the method of regularized Stokeslets [15] to relate the forces on the flagellum with the velocities, where the force densities on a single filament are constructed as in Section 4.2.3. The boundary conditions on the filament are implemented in a similar manner to the single filament case, as described in Section 4.2.4. However, in this scenario with the free swimming cell, the net force on the cell body should be zero, which results in a translation of the cell body. We use this fact to solve for the translation velocity ${\mathbf{U_T}}^\ell$,

again relating forces and velocities using the method of regularized Stokeslets. Further details are provided in Appendix B.

Finally, for this simulation, we assign initial conditions for tangent angle ϕ, motor populations $n_{\pm}$, and starting reference position of the body $\mathbf{X_T}$. The initial conditions for the tangent angle ϕ and motor population $n_{\pm}$ are obtained in the same way as for the clamped isolated filament as described in Section 4.3, and the initial reference body position $\mathbf{X_T}^0$ is set to the origin. Since we stagger the solution of these two evolution equations, the initial value of $\partial_t \phi^0$ is used only when solving the bound motor dynamics in Equation (4.19). For this initial calculation, we set $\partial_t \phi^0 = 0$.

4.4.2. Examining the Emergent Waveforms. With this simulation, we evaluate the swimming simulation through similar tests to those in Section 4.3.1. We first confirm that, for sufficiently high motor activity, the flagellum on the swimmer exhibits emergent periodic beating. The initial conditions for the flagella are given by a perturbation of the filament given in Equation (4.26). The initial conditions for the bound motor state are set to a constant value, as in Section 4.3.1. We fix the sperm number Sp = 1, and vary the motor activity μ_a between 1500 and 2500. After running the simulation long enough for a steady state to emerge, we visualize the resulting waveforms in Figure 4.8. In Figure 4.8a, the filament remains flat and no beat emerges. In Figure 4.8b, a

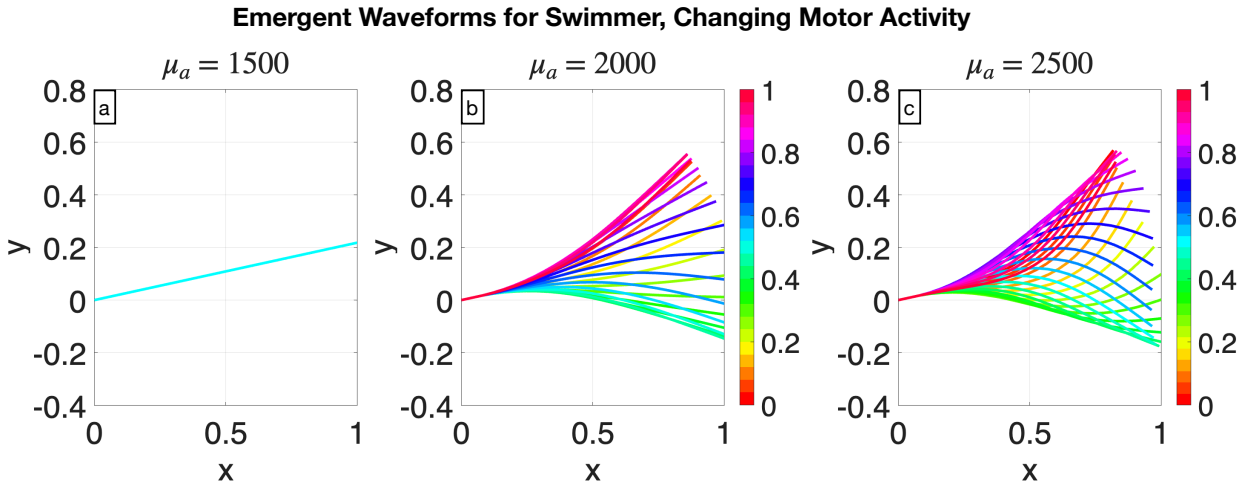

FIGURE 4.8. Emergent waveforms from the swimmer simulation for different motor activity μ_a. All simulations start at the same initial condition, with parameters Sp = 1, $\mu_b = 90$, $\zeta = 0.4$, $\eta = 0.14$, $\overline{f} = 2$. (a) Waveform for motor activity $\mu_a = 1500$, where no beat emerges. (b) Waveform for motor activity $\mu_a = 2000$, where flat periodic beat emerges. (c) Waveform for motor activity $\mu_a = 2500$, where periodic beat emerges with higher curvature and amplitude.

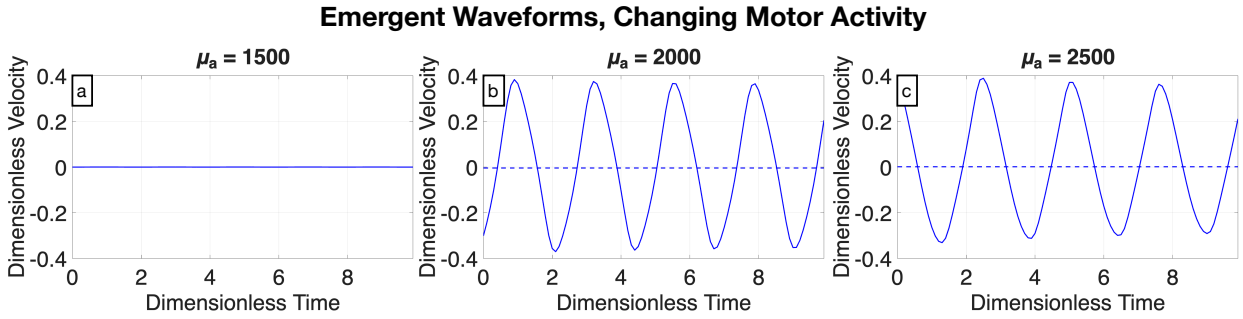

FIGURE 4.9. Cell swimming speeds from the swimmer simulation for different motor activity μ_a. All simulations start at the same initial condition, with parameters Sp $= 1$, $\mu_b = 90$, $\zeta = 0.4$, $\eta = 0.14$, $\overline{f} = 2$. (a) Swimming speed for (a) motor activity $\mu_a = 1500$, where cell does not move; (b) motor activity $\mu_a = 2000$, where the cell moves back and forth but has no net motion; and (c) motor activity $\mu_a = 2500$, where similarly, the cell moves back and forth but has no net motion.

waveform emerges, but it is nearly flat with minimal curvature. In Figure 4.8c, a waveform with noticeably higher curvature emerges. The colors in each plot represent one full beat period. It is evident from the absence of an emergent beat for the full swimmer at motor activity $\mu_a = 1500$ in Figure 4.8 that the presence of the body influences the emergent waveform, as this is different than the emergent beat in Figure 4.4. Additionally, the waveforms for a single filament in Figure 4.4 and for the swimmer in Figure 4.8 for the same motor activity μ_a are different, further demonstrating the effect of the body on the emergent dynamics.

With this swimming simulation, where the flagellar beat emerges from the mechanochemical motor model, we can also examine the swimming speed of the cell. We observe the swimming speeds corresponding to the simulations from Figure 4.8, for varying motor activity $\mu_a = 1500, 2000, 2500$. These swimming speeds are shown in Figure 4.9. For low motor activity $\mu_a = 1500$ in Figure 4.9a, where no beat emerges, the swimming speed is close to zero, as expected. For both $\mu_a = 2000$ and $\mu_a = 2500$ in Figure 4.9b-c, the swimming speed is nonzero, but the average of the swimming speed is close to zero. This indicates the cell moves back and forth, but has no net motion.

In the next chapter, we will investigate the role of the cell body in the swimming simulation and examine the lack of net motion observed in Figure 4.9.

CHAPTER 5

Motor Model Results

In the following chapter, we present simulations and compare the waveforms which emerge from the model with those from experiments [67]. First, we examine the impact of the cell body on the flagellar beat, similar to [53], but for *C. reinhardtii* rather than sperm. Second, we explore different methods to add asymmetry to our flagellar beat, with the goal of producing an emergent power and return stroke resembling the breaststroke of *C. reinhardtii*, as shown in Figure 1.1. Finally, we report the beat frequency that emerges from our model, and compare it with experimental data [67]. We conclude the chapter by summarizing our findings and discussing directions for future work.

5.1. Impact of the Cell Body

We begin by exploring how the presence of a cell body affects the emergent flagellar beat in the motor model simulation. Li et al. [53] previously investigated the influence of a sperm head on an emergent flagellar beat and found that the presence of the head has a substantial impact on the emergent waveforms.

Here, we examine the emergent beat for a *C. reinhardtii* cell. The *C. reinhardtii* cell size differs from that of a sperm, given in Li et al. [53], because the ratio of flagellar length to body size is different. A sperm flagellum is approximately ten times longer than a sperm head [53], whereas the *C. reinhardtii* body is $\sim$10 μm long, which is roughly the same length as its flagella [39]. Thus, the size of the body in comparison to the length of the flagellum is drastically different between *C. reinhardtii* and sperm.

We compare waveforms for the emergent flagellar for a fixed sperm number and varying motor activity levels μ_a, shown in Figure 5.1. We compare across three different scenarios: a clamped filament isolated in free space, two filaments attached to a *C. reinhardtii* cell body held fixed in place, and a free swimmer in which the filaments are attached to the *C. reinhardtii* cell body which is allowed to move freely. In Figure 5.1, we observe that emergent motion occurs at different

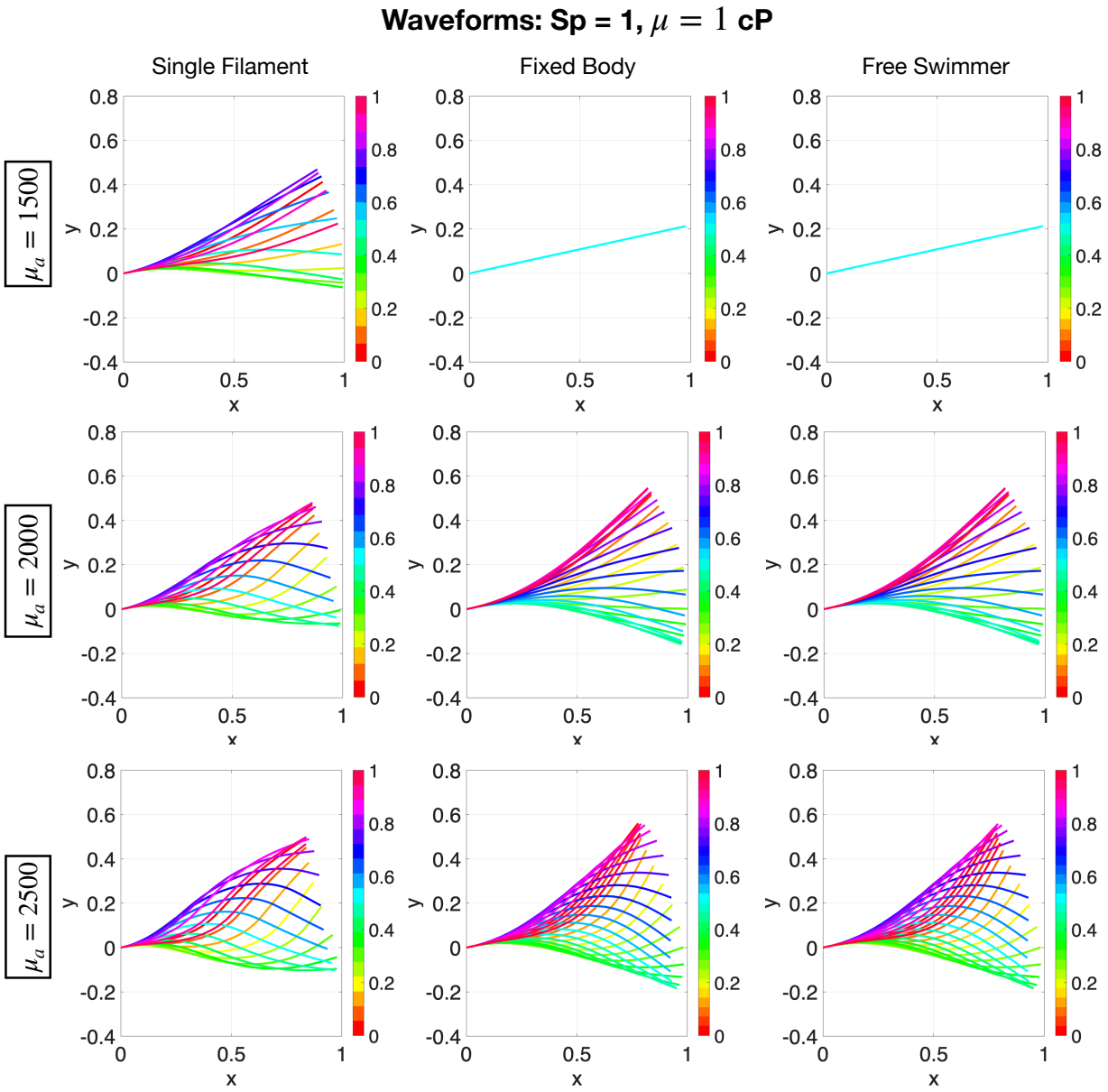

FIGURE 5.1. Comparison of emergent waveforms for the simulations with the isolated clamped filament, the filaments attached to a fixed body, and the free swimmer. For all simulations, we set Sp $= 1$, $\mu_b = 90$, $\zeta = 0.4$, $\eta = 0.14$, $\overline{f} = 2$, and vary the motor activity μ_a as is demonstrated in the left column. As seen in previous work [11, 66], as we increase motor activity for a fixed Sp number, a filament beat emerges. This beat emerges differently in each of the three cases. The colors represent the phase, with the power stroke is shown in oranges, yellows, and greens, and the return stroke is shown in blues and purples.

motor activity levels in these scenarios. In particular, no emergent motion is seen for scenarios that include a cell body at $\mu_a = 1500$. As observed in Chapter 4, increasing motor activity μ_a leads to increased curvature and amplitude of the waveform.

Additionally, in Figure 5.1, the emergent waveforms for the fixed body case and the free swimmer case are nearly the same. This similarity in waveform shape holds for all waveforms across the two scenarios and demonstrates that it is the presence of the cell body that affects the filament dynamics in this simulation, rather than the motion of the cell body.

We take a deeper look at the importance of the body presence in these simulations by investigating a stability curve in phase space, similar to Figure 2c in [66] and Figure 4 in [11], as we examined in Figure 4.7. We examine the behavior of the emergent filament motion across a varying parameter range, for different sperm numbers and motor activity levels. We look at a parameter regime that is more representative of *C. reinhardtii* flagella, where sperm number ranges for $0.5 < \text{Sp} < 2.5$ and motor activity $250 < \mu_a < 2500$, as described in Section 4.2.1. The stability curves for a clamped filament isolated in free space and a free swimmer are shown in Figure 5.2. Below the curves, the filament exhibits no instability and no beat emerges, and above the curves, periodic traveling waves emerge. This curve represents a critical motor activity level $\mu_a^\star$ above which the filament undergoes a Hopf bifurcation. The height of the stability curve differs between the two different types of simulations, as indicated by the colors of the regions, highlighting the difference in dynamics in each scenario. The presence of the cell body raises the height of the stability curve, and thus the critical motor activity level increases. Thus, just like the sperm head impacted the filament dynamics for Li et al. [53], the presence of the cell body is similarly important to the dynamics in a *C. reinhardtii* simulation.

5.2. Asymmetric Waveforms

Having established the importance of the cell body's presence, we next examine the free swimmer simulation. The simplest question to address is whether the swimmer exhibits net motion. We investigate this question using the example shown in Figure 5.3. We compare the dimensionless swimming velocity that is from a cell swimming in a fluid with viscosity 1 cP [67] with the velocity generated by the emergent beat from our motor simulation. In the experimental data, the swimming velocity has a nonzero mean, which results in net forward motion. In contrast, the velocity

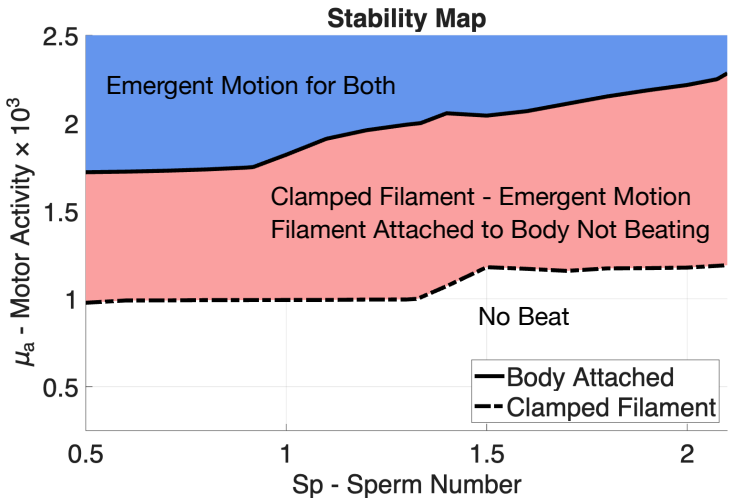

FIGURE 5.2. Stability curves highlighting the transition between no beat to an emergent beat for two scenarios: (1) an isolated clamped filament and (2) a free swimmer, modeled as a cell body with two attached filaments. The second scenario has an identical curve to that of a fixed cell body. We compare the emergent motion of the filaments across sperm number $0.5 < \text{Sp} < 2.5$ and motor activity $250 < \mu_a < 2500$ by looking at the stability curve. In the white region, there is no emergent beat for either simulation scenario. In the red region, the isolated clamped filament has an emergent oscillatory beat, but the swimmer has no emergent beat. In the blue region, both the isolated filament and the swimmer have an emergent oscillatory beat. The other parameters in these simulations are $\mu_b = 90$, $\zeta = 0.4$, $\eta = 0.14$, and $\overline{f} = 2$. These parameters, along with the parameter regime which we examine the motion in, are reasonable for *C. reinhardtii*, as discussed in Section 4.2.1.

produced by the emergent beat in the simulation has zero mean, so the swimmer oscillates back and forth with no net translation over time. A key difference between the data and the simulation is the asymmetry of the waveform. In the experimental waveform shown in the lower left corner of Figure 5.3, the power stroke in oranges, yellow, and greens bends much closer to the body, and the return stroke in blues and purples bends upwards with pronounced curvature. However, in the simulation, the power stroke in oranges, yellows, and greens does not approach the cell body as closely, and the return stroke in blues and purples exhibits far lower curvature than in the data. Additionally, the experimental waveform beats about a non-constant mean shape, shown as the black dashed line, whereas the simulated waveform is symmetric with a nearly flat mean shape. This symmetry and resulting lack of velocity is present across all cases of the model. Varying model parameters does not change the beat symmetry or produce sustained net motion.

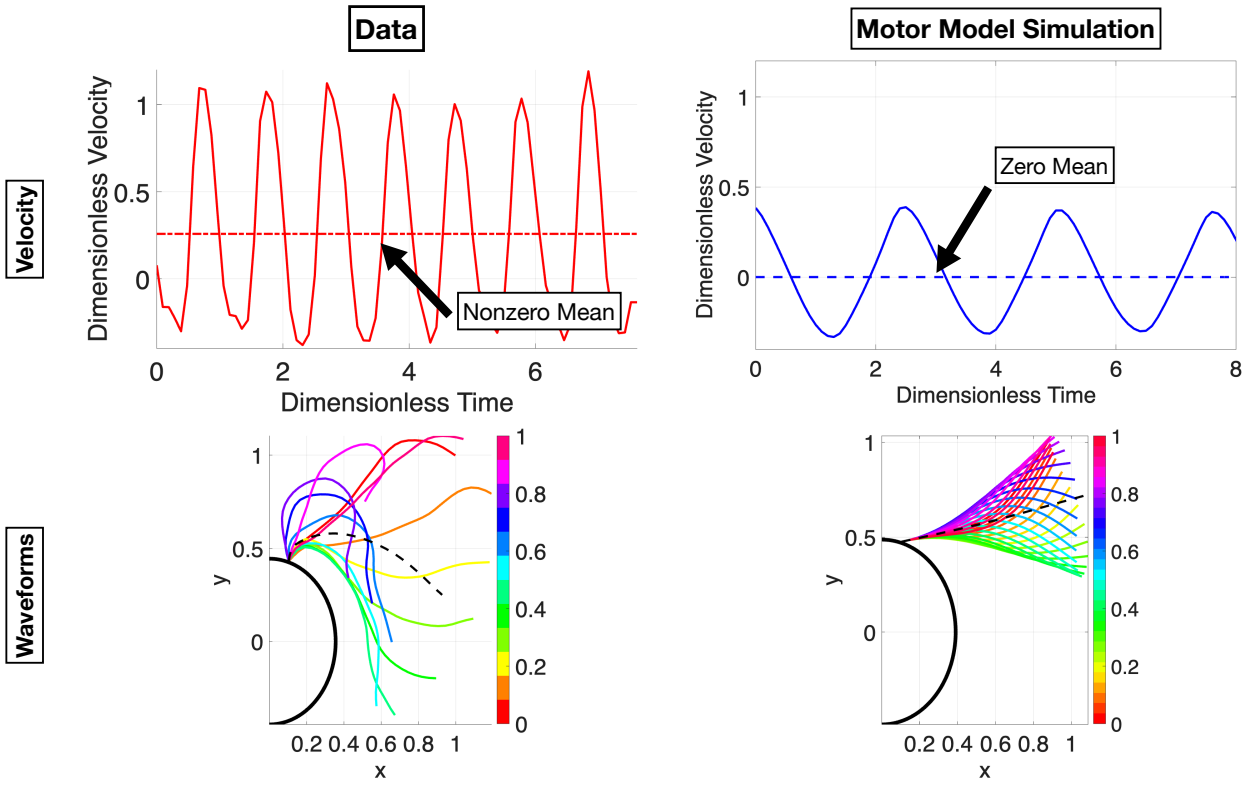

FIGURE 5.3. Comparison of dimensionless velocity and waveforms between data and motor model simulation for a free swimmer, with mean. The cell from the dataset [67] is a cell in fluid viscosity 1 cP. The simulation is run with the following parameters: Sp $= 1$, $\mu_a = 2500$, $\eta = 0.14$, $\zeta = 0.4$, $\overline{f} = 2$. The velocity from the simulation has zero mean, implying no net motion of the swimmer, whereas the cell from the data set has a positive mean and thus has net motion. The primary difference between the waveforms lies in the symmetry; the waveform from the dataset has an asymmetry whereas the waveform in the motor model is symmetric.

The generation of asymmetric beat patterns in models has been approached in several ways, particularly for modeling cilia beats [5, 11, 19, 20, 34, 35, 37], with fewer attempts focused on reproducing the asymmetric beat of *C. reinhardtii* [5, 10, 11, 58, 73]. Here, we add asymmetry to the beat using two different methods: (1) adding in a static, asymmetric mean shape [10] and (2) implementing biased kinetics [11].

5.2.1. Adding Mean Shape. Geyer et al. [26] discuss the decomposition of the flagellar waveform into a symmetric, dynamic beat and a static, asymmetric mean shape. Their study utilizes data for demembranated *C. reinhardtii* flagella reactivated with ATP. They report that the curvature of the mean flagellar shape increases with ATP concentration and that for a sufficiently

large ATP concentration, the amplitude of the symmetric beat becomes insensitive to ATP changes. These results support the idea that the mean shape and the dynamic beat have distinct regulation mechanisms. Cass and Bloomfield-Gadêlha [10] incorporated this idea into their own motor model simulations where they compared their results with the same demembranated *C. reinhardtii* data from [26]. They developed a reaction-diffusion model based on the sliding control mechanism [66],

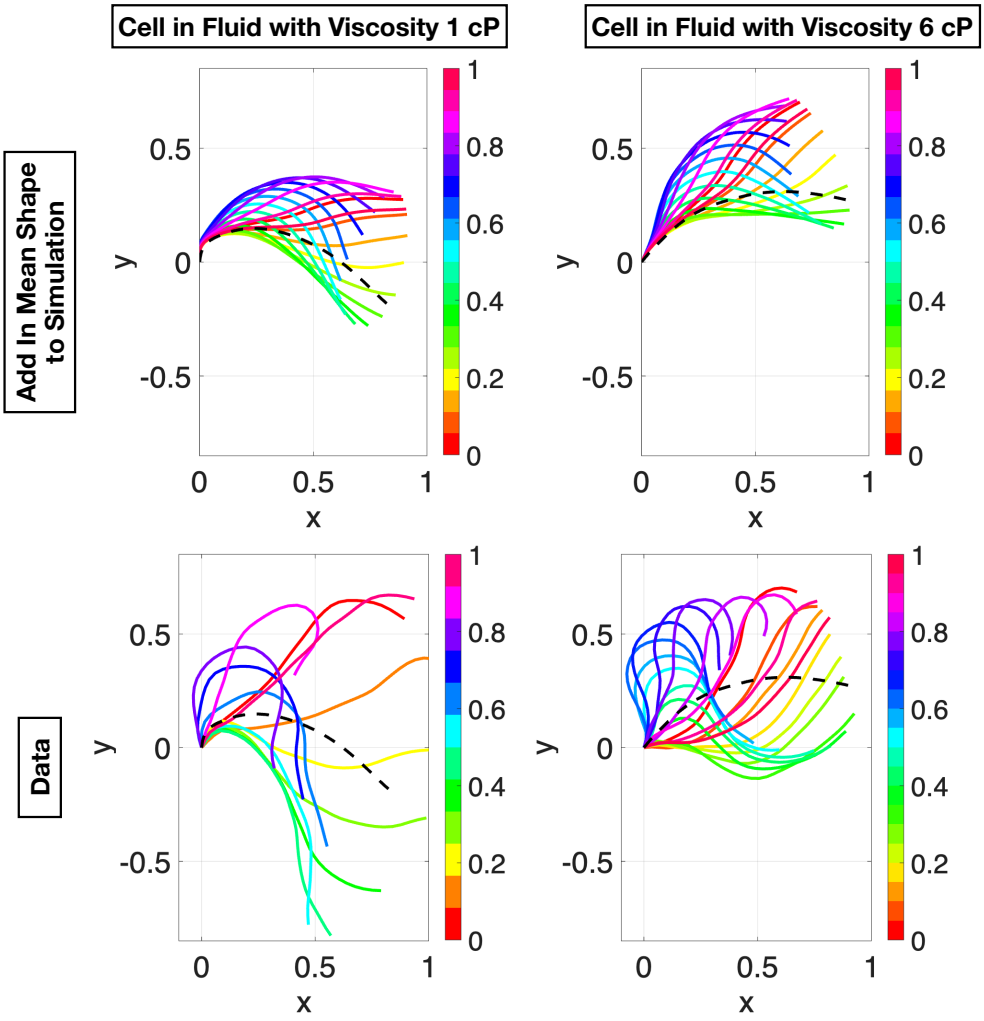

FIGURE 5.4. Two examples of adding the mean shape to the emergent beat from the molecular motor model simulation. The waveforms from the simulation were found using the following parameters: Sp $= 1$, $\mu_a = 2500$, $\mu_b = 90$, $\eta = 0.14$, $\overline{f} = 2$. The mean shape has been added from two different cells in the data set [67], one from a cell in a fluid of viscosity 1 cP and one in a fluid of viscosity of 6 cP. The first row shows this mean shape added to the symmetric beat that is from the motor model from Chapter 4, and the second row shows the original beat from the data. The mean shape is featured as a dashed black curve.

though their simulations do not include hydrodynamics. This study shows that the dynamic beat matched the de-meaned experimental waveform well, and that adding the static mean shape results in a total waveform that qualitatively resembles their demembranated *C. reinhardtii* data.

We apply the same idea in our simulation by adding the mean shape from our dataset [67] to the symmetric beat produced by the motor model simulation developed in Chapter 4. Two examples are shown in Figure 5.4. The parameters were selected to favor the increased bending of the waveform. The two different mean shapes were chosen to compare across the viscosity regime of our dataset [67]. Beginning with the left column of Figure 5.4, where we add the mean shape from the cell swimming in a fluid with viscosity 1 cP to the simulated waveform, we observe the power stroke in oranges, yellows, and greens bends downward more in the modified simulation compared to that without an added mean shape, though still not as strongly as in the experimental data. The return stroke in the simulation, shown in blues and purples, exhibits less curvature than the experimental waveform. The same pattern appears in the right column in Figure 5.4 as well, where we add the mean shape from the cell swimming in a fluid with viscosity 6 cP to the simulated waveform. Again, the return stroke lacks the pronounced curvature seen in the experimental data. Although this procedure introduces asymmetry into the beat, the resulting waveforms still do not resemble the beat observed in the experimental data. This motivates exploring an alternative method.

5.2.2. Biased Kinetics. Chakrabarti and Saintillan [11] introduce the idea of biased dynein kinetics to model ciliary beating, inspired by the geometric clutch mechanism model of Bayly and Wilson [5]. Biased kinetics are implemented by assigning distinct binding and unbinding rates to each filament. The binding rate is written as

$$\pi_{\pm} = \pi_0^{\pm}(1 - n_{\pm})$$

and the unbinding rate is written as

$$\epsilon_{\pm} = \epsilon_0^{\pm} n_{\pm} \exp(F_{\pm}/f_c).$$

After non-dimensionalization, the duty ratio η differs between the two filaments, so we label it as $\eta_\pm$. We rewrite this equation as

$$\partial_t n_\pm = \eta_\pm(1-n_\pm) - (1-\eta_\pm)n_\pm \exp\left(\overline{f}(1 \mp \zeta\phi_t)\right). \tag{5.1}$$

It is important to note that Chakrabarti and Saintillan [11] also incorporate an element of the curvature control feedback mechanism to reproduce waveforms similar to *C. reinhardtii*, motivated by the findings of Sartori et al. [73]. Since Cass and Bloomfield-Gadêlha [10] obtain a good fit to *C. reinhardtii* data for the sliding control motor model with sufficiently large amplitudes, we do not include curvature control feedback in our model.

We run several different duty ratios, where $0.01 < \eta_\pm < 0.4$. We pick this regime because Chakrabarti and Saintillan [11] choose $\eta_+ = 0.17$ and $\eta_- = 0.25$ for their cilia beat, and $\eta_+ = 0.24$ and $\eta_- = 0.39$ for the *C. reinhardtii* beat. From this regime, we pick duty ratios to highlight in Figure 5.5 with a variety of swimming behaviors. These tests were performed in the swimming simulation, so we also examine the resulting cell displacement over time. We examine several duty ratio combinations, where η_+ is the duty ratio on the top + filament in Figure 4.1 and η_- is the duty ratio on the bottom - filament. For duty ratios that are too low ($\eta_\pm < 0.07$), no emergent beat is observed. Figure 5.5 highlights three representative cases, one in which the swimmer moves backwards, and two with different degrees of forward motion. For $(\eta_+, \eta_-) = (0.07, 0.19)$, shown in the first column of Figure 5.5, the waveform exhibits limited bending, the mean shape is slightly bend downward, and the cell body undergoes net backward motion. The mean swimming velocity is slightly less than zero as well. For $(\eta_+, \eta_-) = (0.21, 0.28)$, shown in the middle column of Figure 5.5, the waveform displays more pronounced bending and has a mean shape that tilts slightly downward. In this case, the cell body achieves a small net forward motion, though the mean swimming velocity is almost zero. Finally, for $(\eta_+, \eta_-) = (0.21, 0.24)$, shown in the right column of Figure 5.5, there is some small bending near the tip, but this case produces the largest net forward motion and the mean swimming velocity is the furthest from zero. This case is particularly interesting because the mean shape bends in the opposite direction of the experimental data in Figure 2.6. Across additional parameter choices not shown, we see similar behavior, where we have the most net forward motion and bending when $\eta_\pm > 0.1$.

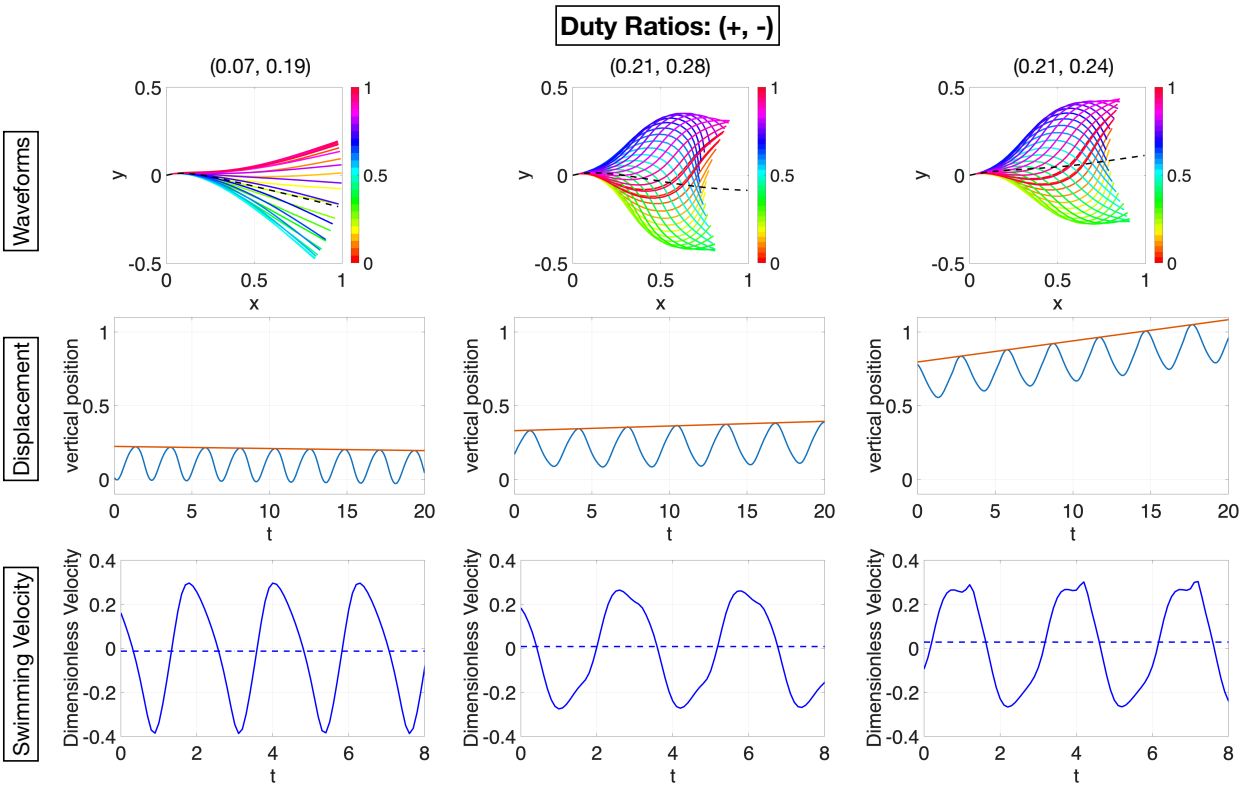

FIGURE 5.5. The top row shows the given waveforms, with the mean shape as a dashed black curve, the middle row shows the vertical displacement of the cell body across time, and the bottom row shows the swimming velocity, with the mean velocity shown as a dashed line. The first column has a duty ratio η_+ for the top "+" filament $= 0.07$ and a duty ratio η_- for the bottom "-" filament $= 0.19$. The second column looks at $(\eta_+, \eta_-) = (0.21, 0.28)$ and the third column shows results for $(\eta_+, \eta_-) = (0.21, 0.24)$. The other parameters in these simulations are as follows: Sp $= 1$, $\mu_a = 2000$, $\mu_b = 90$, $\overline{f} = 2$.

When we examine the waveforms that emerge from simulations with these different duty ratios η, one striking feature is that although these waveforms appear asymmetric, they still do not qualitatively reproduce the stroke seen in the *C. reinhardtii* data in Figure 1.1. In the experimental datasets, the mean shape of the waveform has much higher curvature, as seen in Figure 2.6. In contrast, in Figure 5.5, the mean shapes of the waveforms for these emergent beats are all flat or nearly flat, with very little curvature. Additionally, the experimental waveforms in Figure 1.1 have distinct power and return strokes, where the power stroke is relatively flat and the return stroke bends sharply to hug the cell body. This distinction is also visible in Figure 5.3, where the power stroke for the experimental data is in oranges, yellows, and greens, and the return stroke in blues and purples. In Figure 5.5, the power stroke is again pictured in orange, yellows, and greens, and

the return stroke is pictured in blues and purples. However, these components of the stroke look very similar to each other, and we do not observe a flatter power stroke or a return stroke with higher curvature. We explore this idea further in the following section.

5.2.3. Extra Asymmetry in De-meaned Beat. After exploring two methods for introducing asymmetry into the beat and still failing to qualitatively reproduce the stroke of *C. reinhardtii* as seen in our dataset in Figure 1.1, we take a closer look at our original data and at the symmetric waveform from our simulations coupled with the molecular motor model to determine if there is an additional feature we are missing.

Initially, we reconsider what 'asymmetry' means in this context. We know that the mean shape, as shown in Figure 2.6, contributes asymmetry to the beat. To isolate the dynamic stroke, we remove the mean shape and examine only the de-meaned strokes from the data [67], shown in Figure 5.6. This figure is arranged in the same manner as the first two rows of Figure 1.1.

We see that these figures contain asymmetric beats. If the beat were symmetric, it would be antiperiodic, as defined in Section 3.3. As shown in Figure 5.6 and previously in Figure 3.2,

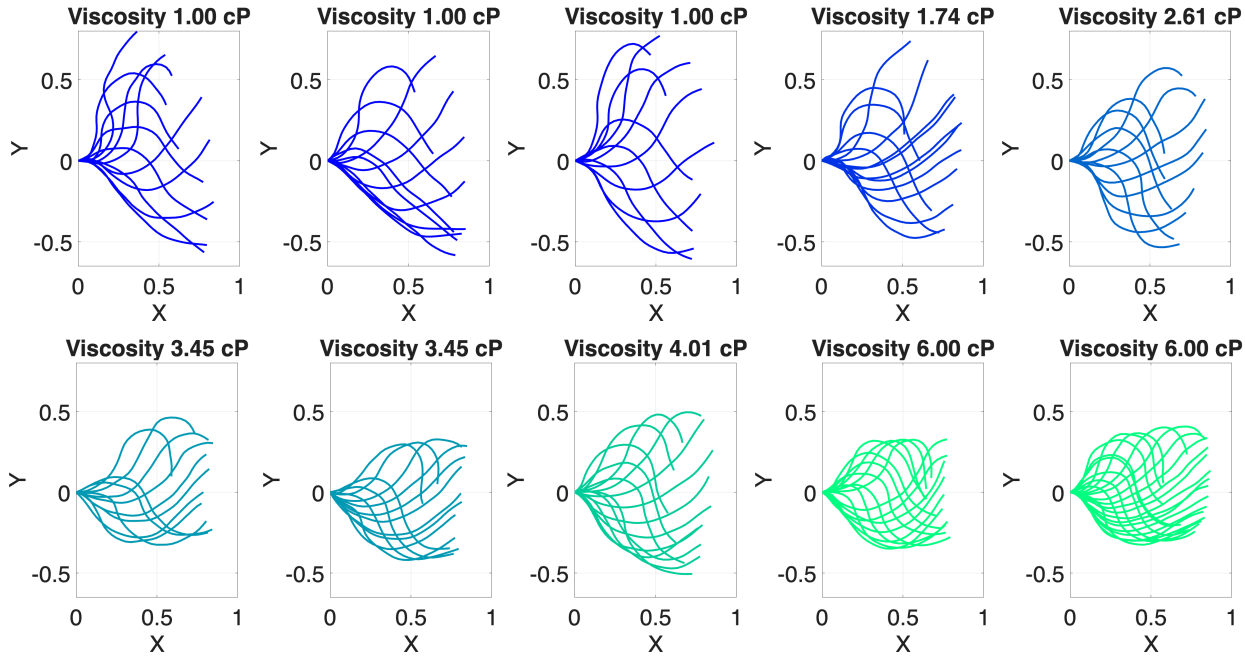

FIGURE 5.6. De-meaned flagellar stroke patterns over a single period, where the length of the flagellum has been normalized to 1. Each panel corresponds to experimental data from [67] with individual *C. reinhardtii* cells. The cells are colored in blue and green and are in Newtonian fluids, with viscosities ranging between 1-6 cP.

the experimental data is not antiperiodic. In Section 3.3, we previously examined the lack of antiperiodicity in the de-meaned waveforms and concluded that producing such non-antiperiodic behavior requires a waveform containing multiple frequencies, as used in our reconstruction of the data in Figure 2.3.

Knowing that the experimental waveforms exhibit this non-antiperiodic property, we next explore if the emergent waveforms from our motor model simulations are antiperiodic. Thus, we perform shape mode analysis on an example from our simulation following the procedure described in Chapter 2. The results are shown in Figure 5.7. First, we look at an example with non-biased kinetics, from a simulation with a free swimmer, where the waveform is displayed in the bottom right panel of Figure 5.1. The parameters for this simulation are: Sp $= 1$, $\mu_a = 2500$, $\mu_b = 90$, $\eta = 0.14$, $\overline{f} = 2$. We review the results from Figure 5.7 for this specific simulation of a free swimmer. Other parameter choices produces similar results. The shape modes in Figure 5.7a resemble those in Figure 2.2a, with slightly fewer bends. Figure 5.7b shows the eigenvalue strength, where we see that the first two shape modes capture 99.7% of the variance. For comparison, the first four modes in our data analysis in Chapter 2 captured 99.1% of the variability. We note that for waveforms that exhibit more bending (such as that in Figure 5.1 for the clamped filament in the bottom left panel), the first eigenvector may contribute approximately 60% of the variability, but the first two eigenvectors still contribute close to 100% of the variability. Therefore, in the following subfigures we display only the first two coefficients, as they capture the majority of the stroke. Figures 5.7c-d show the first two simulated time-dependent coefficients in blue and their corresponding Fourier series fits using Equation (2.4) with two frequencies in red. The upper half of these panels show the projections, with the projections in frequency space are shown on the lower panel. These plots show the coefficients with a single dominant frequency and no harmonics, unlike those in Figure 2.3, which contain multiple harmonics. This demonstrates that the de-meaned stroke in these simulations are antiperiodic, which is different than what we observe in the experimental data.

We repeat this process of shape mode analysis for a simulation with biased kinetics, as described in Section 5.2.2. The results are shown in Figure 5.8 for a free swimmer, with the waveform shown in the top right panel of Figure 5.5. The parameters for this simulation in Figure 5.8 are Sp $= 1$, $\mu_a = 2500$, $\mu_b = 90$, $\eta_+ = 0.21$, $\eta_- = 0.24$, $\overline{f} = 2$. The shape modes in Figure 5.8a resemble those in Figure 5.7a. Figure 5.8b shows the eigenvalue strength, where the first two shape modes capture

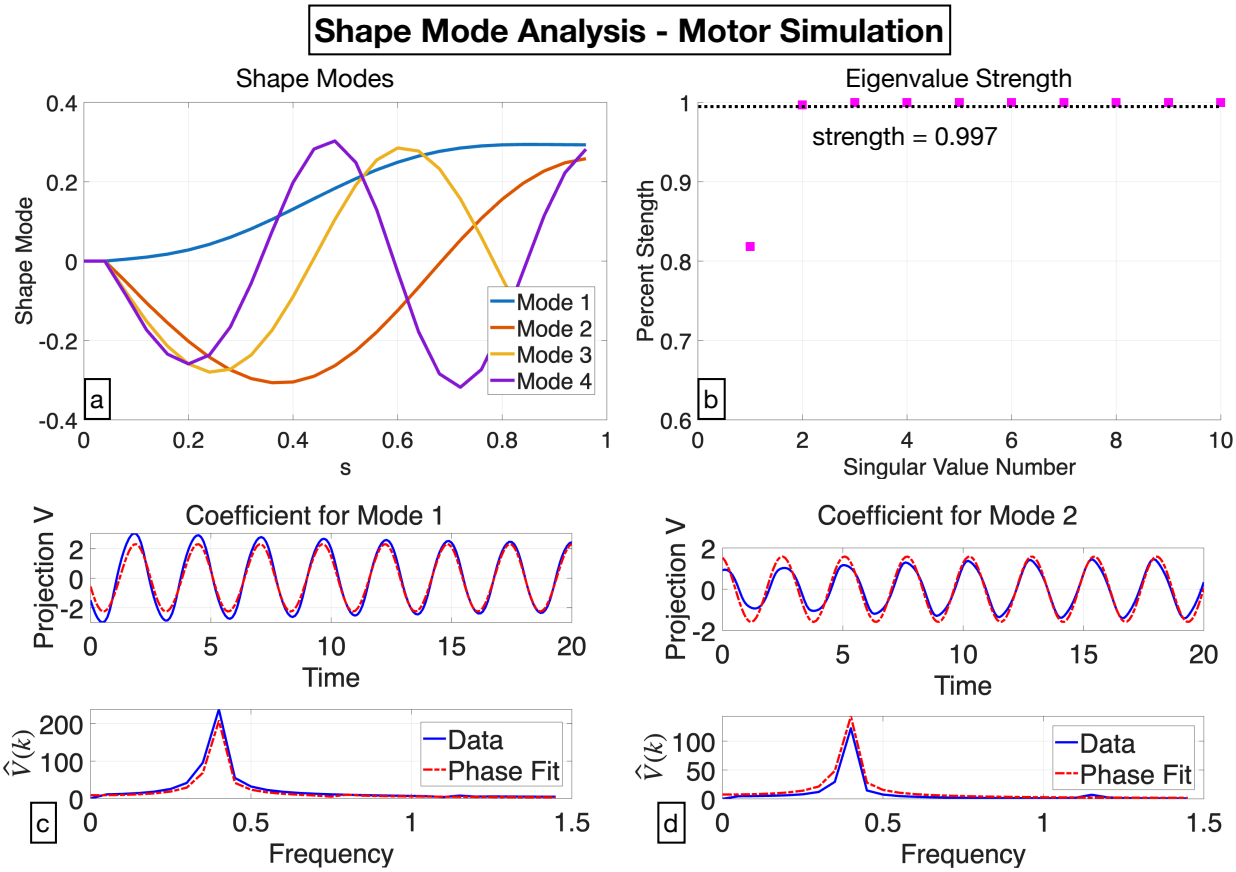

FIGURE 5.7. Shape mode analysis on motor model simulation. This is an simulation with a free swimmer, with the following parameters: Sp = 1, $\mu_a = 2500$, $\mu_b = 90$, $\eta = 0.14$, $\overline{f} = 2$. A waveform for this scenario is shown in the bottom right corner of Figure 5.1. Figure (a) shows the shape basis modes for this simulation, where the basis modes are similar to those in Figure 2.2a. Figure (b) shows the eigenvalue strength, which is defined in Equation (2.3). We see that the first two shape modes dominate the variability of the space much more than that of the data seen in 2.2b. Figures (c)-(d) show the projections v_1-v_2, with the results from the simulation in blue and the fits as defined in Equation (2.4) in red. The Fourier transforms of these projections are shown in the lowest panels.

99.7% of the variability of the space, and we see the first shape mode captures slightly less than 70% of the space variability. As before, we therefore display only the first two coefficients in the following figures, since they capture the majority of the stroke. Figures 5.8c-d again show the first two simulated time-dependent coefficients in blue and their corresponding Fourier series fits with two frequencies in red. These coefficients still exhibit a single dominant frequency with no harmonics, unlike those in Figure 2.3, which contain multiple harmonics. Since the time dependent coefficients still are single frequency with no harmonics, even for the simulations with biased kinetics, the

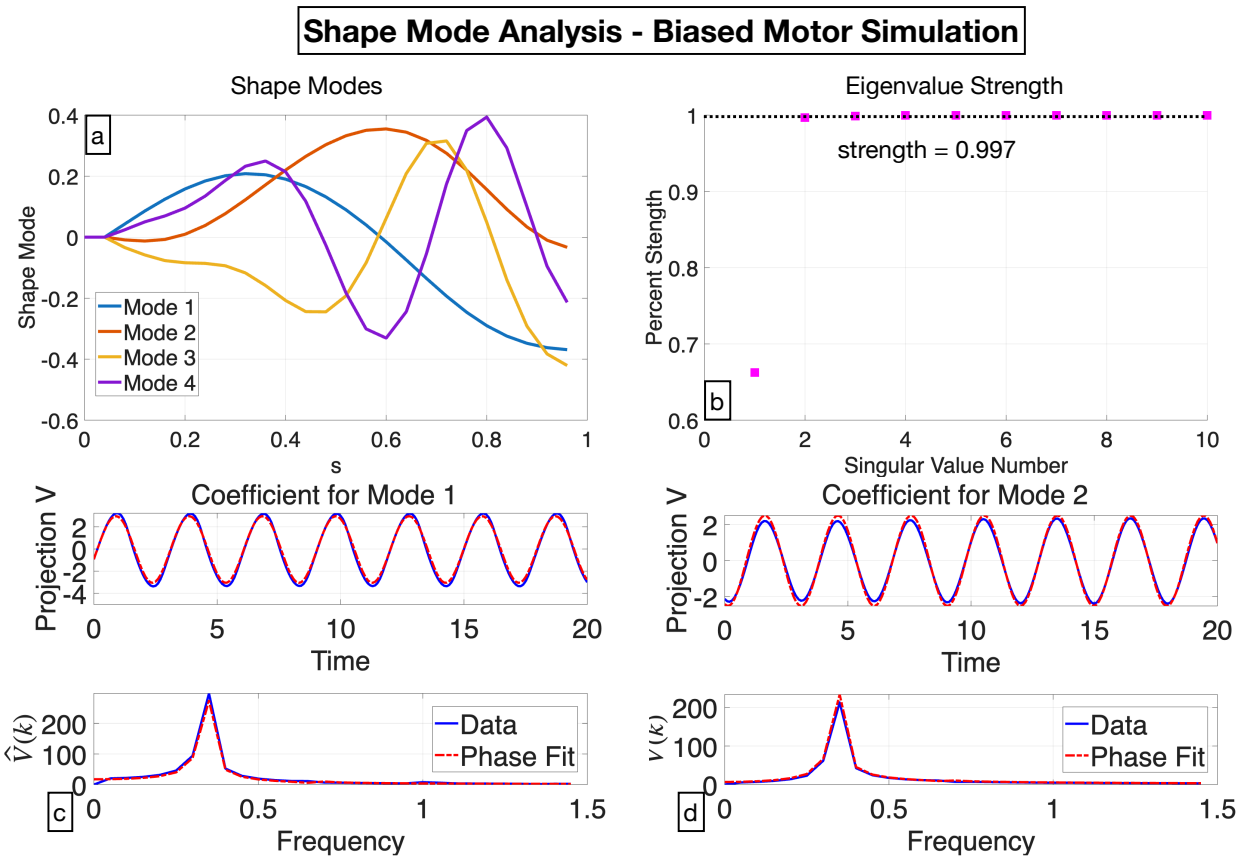

FIGURE 5.8. Shape mode analysis on motor model simulation with biased kinetics. This is an simulation with a free swimmer, with the following parameters: Sp = 1, $\mu_a = 2000$, $\mu_b = 90$, $\eta_+ = 0.21$, $\eta_- = 0.24$, $\overline{f} = 2$. A waveform for this scenario is shown in the top right corner of Figure 5.5. Figure (a) shows the shape basis modes for this simulation, where the basis modes are similar to those in the previous figures. Figure (b) shows the eigenvalue strength, which is defined in Equation (2.3). We see that the first two shape modes dominate the variability of the space much more than that of the data seen in 2.2b. Figures (c)-(d) show the projections v_1-v_2, with the results from the simulation in blue and the fits as defined in Equation (2.4) in red. The Fourier transforms of these projections are shown in the lowest panels.

de-meaned stroke for these simulations remain antiperiodic, which is different than we see in the experimental data.

Thus, our current formulation for the molecular motor model cannot capture the inherent asymmetry of the beat, even if we include biased kinetics. We will discuss possible alternatives to the model in the discussion, but first, we examine whether this model captures the frequency changes observed in the data.

5.3. Frequency Comparison

We investigate whether the simulation described in Chapter 4 captures the changes in beat frequency with fluid viscosity observed in *C. reinhardtii*. Camalet and Jülicher [9] previously identified a critical frequency at the Hopf bifurcation where motion emerges, and showed that this frequency scales as $\xi_{\perp}^{-1/2}$, where $\xi_{\perp}$ is the perpendicular drag coefficient. Since $\xi_{\perp}$ is proportional to the fluid viscosity μ, their model predicts that the beat frequency should scale as $\mu^{-1/2}$. Qin et al. [67] argue this relationship from Camalet and Jülicher [9] applies to cells swimming in fluids with low viscosities from 1-6 cP. This drop in frequency with fluid viscosity is visible in Figure 1.2b. Although Qin et al. [67] shows this scaling in their Figure 2a, it is important to note that this original scaling law was derived specifically at the Hopf bifurcation, for a critical motor activity $\mu_a^{\star}$. Due to the nature of the experimental data from [67], it is unclear how close the *C. reinhardtii* beats are to the bifurcation and critical motor activity $\mu_a^{\star}$. Other studies [25, 78] also report a decrease in beat frequency in response to increasing fluid viscosity for *C. reinhardtii*, but these studies do not show the same scaling relationship between frequency and fluid viscosity. In fact, Garcia et al. [25] finds that frequency scales like μ^{-1} in their study. Nevertheless, both the experiments and theory of Camalet and Jülicher [9] agree that as fluid viscosity is increased, beat frequency should decrease.

Figure 5.9 shows how the beat frequency changes with sperm number, for the single isolated filament on the left panel and the swimming simulation on the right panel. The different colors correspond to different motor activity levels μ_a. For lower motor activity, several curves terminate midway across the plot. As the sperm number increases for a fixed motor activity μ_a, the system passes through a Hopf bifurcation, the beat oscillation is lost, and the rest state becomes stable. This stabilization of the rest state corresponds to crossing the stability curves pictured in Figure 5.2. Generally, looking at the vertical axis on both plots in Figure 5.9, we see that as sperm number increases, frequency does not decrease substantially and the curves appear fairly flat in some areas.

To examine these frequency changes more closely, we zoom in on the region for $1 < \mathrm{Sp} < 1.6$, which corresponds to fluid viscosity $1 < \mu < 7$ cP, matching the viscosity regime of our *C. reinhardtii* experimental dataset. Figure 5.10 compares the beat frequency normalized by the frequency for the cell at fluid viscosity 1 cP for the isolated clamped filament, the free swimmer, and the *C. reinhardtii* dataset [67]. In the experimental data, as shown in Figure 5.10c, increasing fluid

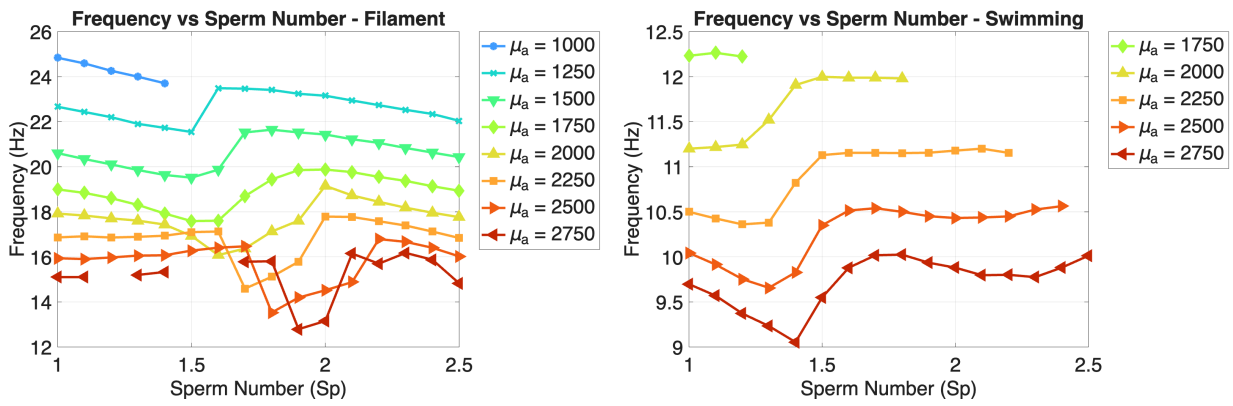

FIGURE 5.9. We compare frequency (Hz) with sperm number (Sp) in our simulation as developed in Chapter 4. The left panel shows the scenario with the isolated clamped filament, whereas the right panel shows the simulation with a free swimmer. The frequency here is re-dimensionalized using frequency time scale as found in Table 4.1. The different colors represent different motor activities μ_a.

viscosity from 1 to 6 cP reduces the beat frequency by roughly a factor of 2. However, in both simulated scenarios, for the isolated filament and the free swimmer, increasing viscosity leads to only a very slight decrease, or even a slight increase in frequency. The largest drop in frequency is about 10%. Thus, our simulation does not reproduce the experimentally observed decrease in beat frequency for *C. reinhardtii* reported in the literature [25, 67, 78], regardless of whether or not the cell body is included in the simulation.

5.4. Discussion

In Chapter 4, we developed a swimming simulation for *C. reinhardtii* coupled with the nonlinear sliding control molecular motor model [9, 66]. In this chapter, we evaluate this model in three ways: (i) assessing the importance of the presence of the cell body, (ii) investigating how this model could be modified to reproduce the asymmetric beat of *C. reinahrdtii*, and (iii) comparing the emergent beat frequency with experimental data as we change fluid viscosity. We find that while the presence of the cell body does influence the flagellar beat dynamics, its inclusion coupled with the motor model in its current implementation does not produce asymmetric waveforms, and the emergent frequency does not match the trends of our data. While others have reproduced *C. reinhardtii* beats that qualitatively resemble the experimental stroke [5, 10, 11], these studies have neither explored a broad parameter regime to determine whether patterns of *C. reinhardtii* beats emerge, nor relied solely on the sliding control model to reproduce these beats qualitatively. While we have

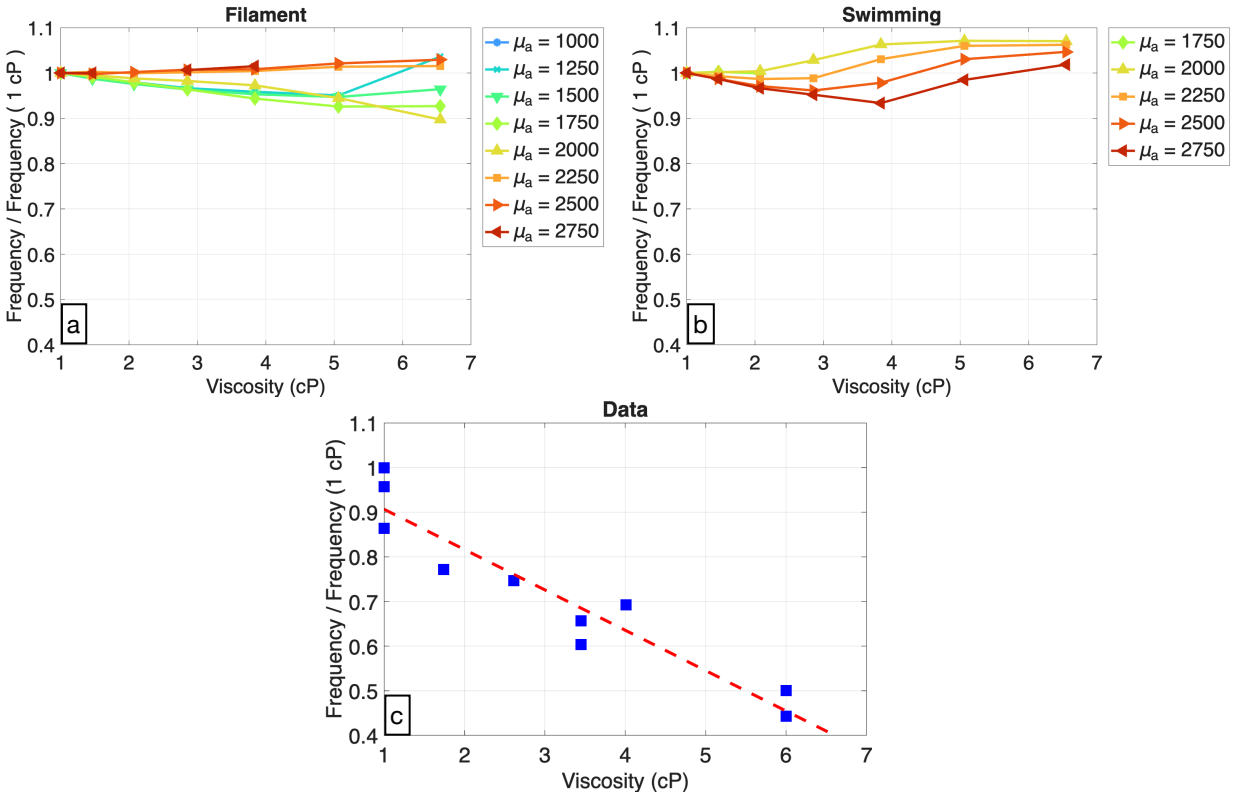

FIGURE 5.10. Comparison of frequencies from simulations to that of *C. reinhardtii* data [67]. Beat frequency divided by the frequency from the cell in fluid with viscosity 1 cP plotted against fluid viscosity, for (a) the isolated clamped filament, (b) the free swimmer, and (c) the *C. reinhardtii* data. For the experimental data, the frequency is normalized by the average frequency at 1 cP.

not performed a complete parameter search, our current results indicate that this model does not reproduce *C. reinhardtii* beats.

CHAPTER 6

Conclusion

This dissertation explores the effects of fluid viscosity on flagellar waveforms of *C. reinhardtii* using experimental data and numerical simulations.

First, we quantify the viscosity-dependent changes on the flagellar beat by performing shape mode analysis on ten different cells in Newtonian fluids from the experimental dataset [67]. In Chapter 2, we identify a unified shape basis, construct low dimensional representations of the flagellar beat, and then separately examine how the fluid viscosity influences the mean shape and the time-dependent stroke. It is not apparent how these changes affect the cell swimming speed, so we then develop and utilize a swimming simulation to further quantify viscosity dependent changes in gait in Chapter 3. Using this numerical swimming simulation, we isolate the contributions of the mean shape and time-dependent stroke, and we find that the viscosity-dependent changes in mean shape have a substantial impact on the swimming speed.

Next, we examine the mechanistic origins of these gait changes by investigating the generation of flagellar beating patterns. In Chapter 4, based on previous studies [9, 11, 53, 66, 68], we develop a molecular motor model for the filament with a sliding control regulation feedback mechanism, coupled with a swimming simulation. We use this simulation to explore how fluid viscosity affects emergent flagellar beats in Chapter 5. In particular, we determine that the *C. reinhardtii* cell body affects the emergent beat, but the model cannot capture waveform asymmetries found in experimental waveforms, and the emergent frequency changes with fluid viscosities do not match that of our dataset. We conclude in Chapter 5 that while we have not conducted a full parameter exploration of this model, our current results using parameters that others have utilized [10, 11, 66] do not reproduce waveforms nor changes in beat frequency as seen in experimental data [67].

One possible modification to the model is to change the mechanochemical regulation mechanism. In our simulations, we used the sliding control regulation mechanism [9, 66]. Other studies [6, 11, 73] have explored adding a curvature control mechanism to their simulation, but unlike the sliding control mechanism, this regulation mechanism is not based on a specific biophysical feedback

mechanism. The geometric clutch mechanism [58], as detailed in Chapter 4, has been used to model a specific, individual *C. reinhardtii* beat [5] using reasonable parameter values. Thus, an alternative direction would be to attempt to reproduce frequencies and asymmetries of the *C. reinhardtii* beat using the geometric clutch model for the regulation mechanism instead.

Other studies have argued that a regulation mechanism based on mechanochemical feedback is not necessary to produce emergent motion [4, 80]. Bayly and Dutcher [4] propose that a flutter instability may occur when the filament is subject to steady axial loading. They demonstrate that dynein motors simply need to generate a tension that pulls steadily above a critical force. Woodhams et al. [80] further develops this model, developing a multi-filament model of the axoneme, rather than the simple two filament representation used in this dissertation. This flutter instability framework has been shown to capture the changes in *C. reinhardtii* beat frequency with fluid viscosity [59].

It has also been shown that the sliding control model may not fully capture the dynamics of an entire eukaryotic flagellum. Sangani et al. [72] applied the sliding control model to analyze the beat of *Ciona* sperm flagellum. This study found that the central 50-60 percent of the flagellum behaves consistently with sliding control theory, and their results suggest more complex models may be required, such as those that vary the density of motors along the filament or different regulation mechanisms like geometric clutch. Sangani et al. [72] conclude that the complex flagellar dynamics cannot be adequately described with the sliding control model alone. This work is extended Foster et al. [22], who demonstrated that a mechanical control mechanism where torque is proportional to the microtubule sliding velocity can produce the beating frequency and other characteristic features of eukaryotic flagella.

Our results in this dissertation are consistent with the conclusions of Sangani et al. [72], providing further evidence that the sliding-control model is unable to reproduce the complex dynamics of a eukaryotic flagellum, specifically that of *C. reinhardtii*. The consistency of this failure across multiple tests suggests a structural limitation of the model rather than a parameter-selection issue. A comprehensive exploration of the non-dimensional parameter space in Table 4.2 would be required to fully rule out isolated parameter regimes, but the results presented here indicate that the sliding control mechanism framework, in its current form, is insufficient to capture the characteristic beating patterns and beat frequency of *C. reinhardtii*.

APPENDIX A

The Method of Regularized Stokeslets

The method of regularized Stokeslets is a numerical method that was initially derived by Ricardo Cortez [15, 16] for computing Stokes flows driven by regularized point forces. The method utilizes a regularized Green's function, which is the exact solution to the Stokes equations with a regularized point force centered at $\mathbf{x_0}$.

We consider the generic situation in an infinite domain where we are given a point force $\mathbf{F}$, given by

$$\mathbf{F} = \mathbf{f}\delta(\mathbf{x} - \mathbf{x_0}),$$

where $\delta(\mathbf{x} - \mathbf{x_0})$ is a Dirac delta function centered at $\mathbf{x_0}$. We input this as the forcing term in Stokes equations

$$\begin{aligned} \mu\Delta\mathbf{u} &= \nabla p - \mathbf{f}\delta(\mathbf{x} - \mathbf{x_0}) \\ \nabla \cdot \mathbf{u} &= 0. \end{aligned}$$

We can find the exact solution $\mathbf{u}$ to this equation [15, 16]. The velocity at $\mathbf{x}$ for a point force at $\mathbf{x_0}$ is defined as

$$\mathbf{u}(\mathbf{x}) = \frac{1}{8\pi\mu}\left[\mathbf{F}(\mathbf{x_0})\frac{1}{r} + (\mathbf{x} - \mathbf{x_0})\frac{[\mathbf{F}(\mathbf{x_0}) \cdot (\mathbf{x} - \mathbf{x_0})]}{r^3}\right]. \tag{A.1}$$

Since we are solving the Stokes equations numerically, we must regularize this Dirac delta function using an approximation. This approximation is called a blob function ϕ_ϵ [15]. Blob functions are radially smooth, symmetric functions integrate to one and approach a Dirac delta as $\epsilon \to 0$. Throughout this dissertation, we use the particular blob function for $\mathbf{x} \in \mathbb{R}^3$ [15]

$$\phi_\epsilon(\mathbf{x} - \mathbf{x_0}) = \frac{15\epsilon^4}{8\pi(\|\mathbf{x} - \mathbf{x_0}\|^2 + \epsilon^2)^{\frac{7}{2}}}. \tag{A.2}$$

Another example of a blob function is a Gaussian function with width ϵ.

We can regularize the solution of Stokes equations for the velocity $\mathbf{u}$ at $\mathbf{x}$ for a point force at $\mathbf{x_0}$ in Equation (A.1) using blob function ϕ_ϵ given in Equation (A.2), as [16]

$$\mathbf{u}(\mathbf{x}) = \frac{1}{8\pi\mu}\left[\mathbf{f}(\mathbf{x_0})\frac{r^2+2\epsilon^2}{(r^2+\epsilon^2)^{\frac{3}{2}}} + (\mathbf{x}-\mathbf{x_0})\frac{[\mathbf{f}(\mathbf{x_0})\cdot(\mathbf{x}-\mathbf{x_0})]}{(r^2+\epsilon^2)^{\frac{3}{2}}}\right], \tag{A.3}$$

where $r = \|\mathbf{x}-\mathbf{x_0}\|$.

If we have multiple point forces, we can utilize the linearity of Stokes' equations and use superposition to find the velocity at some point $\mathbf{x_i}$. Then, we have the following relationship where the velocity at a location $\mathbf{x_i}$ can be written as:

$$\mathbf{U}(\mathbf{x_i}) = \sum_{j=1}^{N} M_{ij}(\mathbf{x_1},\ldots,\mathbf{x_N})F(\mathbf{x_j}). \tag{A.4}$$

The Stokeslets matrix, or mobility tensor, M is defined with the blob function from Equation (A.2) and the regularized velocity in Equation (A.3). Thus, we can relate forces and velocities in Stokes flow by the simple linear equation

$$\mathbf{U} = M\mathbf{F},$$

where $\mathbf{U} \in \mathbb{R}^{3M}$, $M \in \mathbb{R}^{3M\times 3N}$, and $\mathbf{F} \in \mathbb{R}^{3N}$. We use this method to solve Stokes equations. Unless explicitly stated, the regularization parameter $\epsilon = \frac{1}{2}\Delta s$.

APPENDIX B

Further Details: Swimmer Simulation Coupled With Motor Model

As described in Section 4.4.1, this appendix details the solution for the translational velocity and the velocity of the free points of the flagellum in the fixed body frame using the method of regularized Stokeslets [15]. We start by considering the velocity at all points on the cell body and on the two flagella. We can separate the velocities on the body and the flagella, as well as isolate the velocity from the fixed body frame and the translational frame. We separate the velocities in this way to consider solving for the velocities in the body frame and translational frame separately. For this section, we will drop indices for space and time, since we require different indices for clarity between flagella and the body (subscripts f and b), as well as for the body frame (superscript b). Thus, the velocities can be deconstructed as

$$\mathbf{U}_f = \mathbf{U}_f^b + \mathbf{U}_T \tag{B.1}$$

$$\mathbf{U}_b = \mathbf{U}_b^b + \mathbf{U}_T. \tag{B.2}$$

In Equation (B.1), we consider the velocity at each point along each flagellum $\mathbf{U}_f$, which is equal to the sum of the translational velocity and the flagellar velocity in the body frame $\mathbf{U}_f^b$. Similarly, in Equation (B.2), we consider the velocity at each point on the cell body $\mathbf{U}_b$, which is equal to the sum of the translational velocity $\mathbf{U_T}$ and the cell velocity in the body frame $\mathbf{U}_b^b$. In the fixed body frame, the cell body is not moving, so the velocity of the body in the fixed frame $\mathbf{U}_b^b$ is zero.

Our goal from this system is to find the velocities on the flagellum in the fixed body frame $\mathbf{U}_f^b$ and the translational velocity $\mathbf{U_T}$. We begin by examining the velocity in the fixed body frame, and then consider what the translational velocity for the swimmer should be when the cell is not pinned in place.

B.1. Flagellum Velocities In the Body Frame

We begin by focusing on the fixed body frame. We relate the forces and velocities using the method of regularized Stokeslets [15]

$$\begin{bmatrix} M_{bb} & M_{bf} \\ M_{bf}^T & M_{ff} \end{bmatrix} \begin{bmatrix} \mathbf{F}_b \\ \mathbf{F}_f \end{bmatrix} = \begin{bmatrix} \mathbf{U}_b^b \\ \mathbf{U}_f^b \end{bmatrix}. \tag{B.3}$$

In Equation (B.3), M_{ff} refers to the mobility Stokeslets matrix for the discrete flagellar points, M_{bb} refers to the mobility Stokeslets matrix for the discrete body points, and M_{fb} and M_{bf} refer to the mobility matrices which map between the flagellar and body points. We know the swimming velocity of the body in the body frame is $\mathbf{U}_b^b = \mathbf{0}$, since the body does not move in the fixed body frame. We define the force

$$\mathbf{F} = \begin{bmatrix} \mathbf{F}_b \\ \mathbf{F}_f \end{bmatrix}, \tag{B.4}$$

where the forces acting on the flagellum are $\mathbf{F}_f = \mathbf{F^b} + \mathbf{F^T} + \mathbf{F^m}$, the sum of the bending, tension, and active motor forces, as defined in Chapter 4. The forces acting on the body are given as $\mathbf{F}_b$.

Our goal is to determine the velocities of the flagella in the body frame, $\mathbf{U}_f^b$. We begin by rewriting the system. First, we solve for the forces on the body $\mathbf{F}_b$:

$$\mathbf{F}_b = -M_{bb}^{-1} M_{bf} \mathbf{F}_f. \tag{B.5}$$

Substituting this expression into the second row of Equation B.3 gives an expression for the flagellar velocities in the fixed body frame,

$$\mathbf{U}_f^b = (-M_{bf}^T M_{bb}^{-1} M_{bf} + M_{ff}) \mathbf{F}_f. \tag{B.6}$$

A useful feature of this solution is that the only matrix inversion required is that of M_{bb}. Since the components of M_{bb} do not change over time, as the body frame coordinates of the cell body remain fixed, we pre-compute M_{bb}^{-1}. Thus, we have the free velocities on the flagellum in the body frame $\mathbf{U}_f^b$, which only require matrix multiplication to compute.

B.2. Translational Velocity

We now allow the cell body to translate and consider the translational reference frame. When the body is fixed in place, as described in the previous section, the forces on the cell body and flagella were not in balance. The free swimmer should experience no net force, as dictated by the force balance in Stokes flow. The translational velocity is determined so that the resulting net drag force $\mathbf{F}^d$ balances the net force in the fixed body frame. With the contribution of the drag force on the cell body and the flagella, the total forces on the cell satisfy the following relation,

$$\Sigma(\mathbf{F} + \mathbf{F}^d) = 0, \tag{B.7}$$

where $\mathbf{F}$ is the force from Section B.1 defined in Equation (B.4). This force $\mathbf{F}$ includes the bending, tension, and active motor forces on the flagellum, as well as the forces on the body as defined in Equation (B.5). The net drag force is given as $\mathbf{F}^d$, and Σ is a matrix which we define as

$$\Sigma = \begin{bmatrix} \mathbb{1} & 0 & 0 \\ 0 & \mathbb{1} & 0 \\ 0 & 0 & \mathbb{1} \end{bmatrix}, \tag{B.8}$$

where $\mathbb{1}$ is a vector of ones of length of the number of discrete points N. If we separate this equation for the forces into terms on the body and the flagellum, we find

$$\Sigma_b(\mathbf{F}_b + \mathbf{F}_b^d) + \Sigma_f(\mathbf{F}_f + \mathbf{F}_f^d) = 0, \tag{B.9}$$

where Σ_b and Σ_f represent summation over the body and flagellar points, respectively.

We now consider the emergent translational velocity $\mathbf{U_T}$. The translational velocity $\mathbf{U_T} \in \mathbb{R}^3$ can be related to the velocities on the body and flagellum in the translational frame by mapping $\mathbf{U_T}$ to each discrete point on the body and on each flagella using the matrix Σ. Thus, we relate forces and velocities using the method of regularized Stokeslets as

$$\begin{bmatrix} M_{bb} & M_{bf} \\ M_{fb} & M_{ff} \end{bmatrix} \begin{bmatrix} \mathbf{F}_b + \mathbf{F}_b^d \\ \mathbf{F}_f + \mathbf{F}_f^d \end{bmatrix} = \begin{bmatrix} \mathbf{U}_b^b + \Sigma_b^T \mathbf{U_T} \\ \mathbf{U}_f^b + \Sigma_f^T \mathbf{U_T} \end{bmatrix}. \tag{B.10}$$

The forces are split as in Equation (B.9) and the velocities are decomposed as in Equations (B.1)–(B.2). Subtracting the fixed body force-velocity relationship in Equation (B.3) from the

full system above yields an equivalent formulation in the translational frame that depends on the drag forces,

$$\begin{bmatrix} M_{bb} & M_{bf} \\ M_{fb} & M_{ff} \end{bmatrix} \begin{bmatrix} \mathbf{F}_b^d \\ \mathbf{F}_f^d \end{bmatrix} = \begin{bmatrix} \Sigma_b^T \mathbf{U_T} \\ \Sigma_f^T \mathbf{U_T} \end{bmatrix}.$$

Since we want to solve for $\mathbf{U_T}$, we write this equation in simplified form as

$$M\mathbf{F}^d = \Sigma^T \mathbf{U_T}. \tag{B.11}$$

In order to solve for the translational velocity $\mathbf{U_T}$, we utilize the force constraint in Equation (B.7) to find the net drag forces $\mathbf{F}^d$.

From Equation (B.11), we can invert M to express the drag force as

$$\mathbf{F}^d = M^{-1}\Sigma^T \mathbf{U_T}.$$

Then, we sum these drag forces $\Sigma\mathbf{F}^d$ and use the constraint in Equation (B.7) to get

$$-\Sigma\mathbf{F} = \Sigma M^{-1}\Sigma^T \mathbf{U_T}. \tag{B.12}$$

We invert $\Sigma M^{-1}\Sigma^T$ to solve for $\mathbf{U_T}$. Thus, we have solved for the translational velocity $\mathbf{U_T}$ as needed for the full simulation.

Bibliography

[1] R. Ahmad, C. Kleineberg, V. Nasirimarekani, Y.-J. Su, S. Goli Pozveh, A. Bae, K. Sundmacher, E. Bodenschatz, I. Guido, T. Vidaković-koch, and A. Gholami, *Light-powered reactivation of flagella and contraction of microtubule networks: Toward building an artificial cell*, ACS Synthetic Biology, 10 (2021), pp. 1490–1504. PMID: 33761235.

[2] G. K. Batchelor, *Slender-body theory for particles of arbitrary cross-section in stokes flow*, Journal of Fluid Mechanics, 44 (1970), p. 419–440.

[3] P. Bayly, B. Lewis, E. Ranz, R. Okamoto, R. Pless, and S. Dutcher, *Propulsive forces on the flagellum during locomotion of chlamydomonas reinhardtii*, Biophysical Journal, 100 (2011), p. 2716–2725.

[4] P. V. Bayly and S. K. Dutcher, *Steady dynein forces induce flutter instability and propagating waves in mathematical models of flagella*, Journal of The Royal Society Interface, 13 (2016), p. 20160523.

[5] P. V. Bayly and K. S. Wilson, *Equations of interdoublet separation during flagella motion reveal mechanisms of wave propagation and instability*, Biophysical Journal, 107 (2014), p. 1756–1772.

[6] P. V. Bayly and K. S. Wilson, *Analysis of unstable modes distinguishes mathematical models of flagellar motion*, Journal of The Royal Society Interface, 12 (2015), p. 20150124.

[7] J. J. Blum and J. Lubliner, *Biophysics of flagellar motility*, Annual Review of Biophysics and Bioengineering, 2 (1973), p. 181–219.

[8] C. Brokaw, *Microtubule sliding in swimming sperm flagella: Direct and indirect measurements on sea urchin and tunicate spermatozoa*, The Journal of Cell Biology, 114 (1991), p. 1201–1215.

[9] S. Camalet and F. Jülicher, *Generic aspects of axonemal beating*, New Journal of Physics, 2 (2000), p. 324.

[10] J. F. Cass and H. Bloomfield-Gadêlha, *The reaction-diffusion basis of animated patterns in eukaryotic flagella*, Nature Communications, 14 (2023).

[11] B. Chakrabarti and D. Saintillan, *Spontaneous oscillations, beating patterns, and hydrodynamics of active microfilaments*, Physical Review Fluids, 4 (2019).

[12] A. T. Chwang and T. Y.-T. Wu, *Hydromechanics of low-reynolds-number flow. part 1. rotation of axisymmetric prolate bodies*, Journal of Fluid Mechanics, 63 (1974), p. 607–622.

[13] ——, *Hydromechanics of low-reynolds-number flow. part 2. singularity method for stokes flows*, Journal of Fluid Mechanics, 67 (1975), p. 787–815.

[14] D. Cortese and K. Y. Wan, *Control of helical navigation by three-dimensional flagellar beating*, Physical Review Letters, 126 (2021), p. 088003.

[15] R. Cortez, *The method of regularized stokeslets*, SIAM Journal on Scientific Computing, 23 (2001), p. 1204–1225.

[16] R. Cortez, L. Fauci, and A. Medovikov, *The method of regularized stokeslets in three dimensions: analysis, validation, and application to helical swimming*, Physics of Fluids, 17 (2005).

[17] R. G. Cox, *The motion of long slender bodies in a viscous fluid part 1. general theory*, Journal of Fluid Mechanics, 44 (1970), p. 791–810.

[18] P. E. Crouch and R. Grossman, *Numerical integration of ordinary differential equations on manifolds*, Journal of Nonlinear Science, 3 (1993), p. 1–33.

[19] R. H. Dillon and L. J. Fauci, *An integrative model of internal axoneme mechanics and external fluid dynamics in ciliary beating*, Journal of Theoretical Biology, 207 (2000), p. 415–430.

[20] J. Elgeti and G. Gompper, *Emergence of metachronal waves in cilia arrays*, Proceedings of the National Academy of Sciences, 110 (2013), p. 4470–4475.

[21] D. Eshel and C. J. Brokaw, *New evidence for a "biased baseline" mechanism for calcium-regulated asymmetry of flagellar bending*, Cell Motility, 7 (1987), pp. 160–168.

[22] K. W. Foster, J. Vidyadharan, and A. S. Sangani, *Evidence for a self-organized compliant mechanism for the spontaneous steady beating of cilia*, Cytoskeleton, 74 (2017), p. 260–280.

[23] E. Gaffney, H. Gadêlha, D. Smith, J. Blake, and J. Kirkman-Brown, *Mammalian sperm motility: Observation and theory*, Annual Review of Fluid Mechanics, 43 (2011), p. 501–528.

[24] M. T. Gallagher, J. C. Kirkman-Brown, and D. J. Smith, *Axonemal regulation by curvature explains sperm flagellar waveform modulation*, Proceedings of the National Academy of Sciences Nexus, 2 (2023).

[25] M. Garcia, S. Berti, P. Peyla, and S. Rafa i, *Random walk of a swimmer in a low-reynolds-number medium*, Physical Review E, 83 (2011).

[26] V. F. Geyer, P. Sartori, B. M. Friedrich, F. Jülicher, and J. Howard, *Independent control of the static and dynamic components of the chlamydomonas flagellar beat*, Current Biology, 26 (2016), pp. 1098–1103.

[27] V. F. Geyer, P. Sartori, F. Jülicher, and J. Howard, *Computational modeling of dynein activity and the generation of flagellar beating waveforms*, Dyneins, (2018), p. 192–212.

[28] A. Ghanbari and M. Bahrami, *A novel swimming microrobot based on artificial cilia for biomedical applications*, Journal of Intelligent & Robotic Systems, 63 (2011), p. 399–416.

[29] A. Gholami, R. Ahmad, A. J. Bae, A. Pumir, and E. Bodenschatz, *Waveform of free, hinged and clamped axonemes isolated from C. reinhardtii: Influence of calcium*, New Journal of Physics, 24 (2022), p. 053025.

[30] A. Ghosh and P. Fischer, *Controlled propulsion of artificial magnetic nanostructured propellers*, Nano Letters, 9 (2009), p. 2243–2245.

[31] R. E. Goldstein, *Green algae as model organisms for biological fluid dynamics*, Annual Review of Fluid Mechanics, 47 (2015), p. 343–375.

[32] J. Gray and G. J. Hancock, *The propulsion of sea-urchin spermatozoa*, Journal of Experimental Biology, 32 (1955), p. 802–814.

[33] J. S. Guasto, J. B. Estrada, F. Menolascina, L. J. Burton, M. Patel, C. Franck, A. E. Hosoi, R. K. Zimmer, and R. Stocker, *Flagellar kinematics reveals the role of environment in shaping sperm motility*, Journal of The Royal Society Interface, 17 (2020), p. 20200525.

[34] S. Gueron, K. Levit-Gurevich, N. Liron, and J. J. Blum, *Cilia internal mechanism and metachronal coordination as the result of hydrodynamical coupling*, Proceedings of the National Academy of Sciences, 94 (1997), p. 6001–6006.

[35] B. Guirao and J.-F. Joanny, *Spontaneous creation of macroscopic flow and metachronal waves in an array of cilia*, Biophysical Journal, 92 (2007), p. 1900–1917.

[36] K. E. Gutierrez, B. Thomases, P. E. Arratia, and R. D. Guy, *Quantification of flagellar gait changes with combined shape mode analysis and swimming simulations*, Philosophical Transactions of the Royal Society A: Mathematical, Physical and Engineering Sciences, 383 (2025).

[37] J. Han and C. S. Peskin, *Spontaneous oscillation and fluid–structure interaction of cilia*, Proceedings of the National Academy of Sciences, 115 (2018), p. 4417–4422.

[38] G. J. Hancock, *The self-propulsion of microscopic organisms through liquids*, Proceedings of the Royal Society of London. Series A. Mathematical and Physical Sciences, 217 (1953), p. 96–121.

[39] E. H. Harris, *The Chlamydomonas Sourcebook*, Academic Press, 1989.

[40] M. Hines and J. Blum, *Bend propagation in flagella*, Biophysical Journal, 23 (1978), pp. 41–57.

[41] E. Hirakawa, H. Higuchi, and Y. Y. Toyoshima, *Processive movement of single 22s dynein molecules occurs only at low atp concentrations*, Proceedings of the National Academy of Sciences, 97 (2000), p. 2533–2537.

[42] J. Howard, *Mechanics of motor proteins and the cytoskeleton*, Sinauer Associates, Publishers, 2001.

[43] Y.-F. Hsiao and Y. C. Chou, *A dynamic model for the processive motion of dynein on microtubules*, Advances in Biological Chemistry, 06 (2016), p. 43–54.

[44] K. Ishimoto, H. Gadêlha, E. A. Gaffney, D. J. Smith, and J. Kirkman-Brown, *Coarse-graining the fluid flow around a human sperm*, Physical Review Letters, 118 (2017).

[45] ———, *Human sperm swimming in a high viscosity mucus analogue*, Journal of Theoretical Biology, 446 (2018), p. 1–10.

[46] R. Johnson and C. Brokaw, *Flagellar hydrodynamics. a comparison between resistive-force theory and slender-body theory*, Biophysical Journal, 25 (1979), p. 113–127.

[47] J. B. Keller and S. I. Rubinow, *Slender-body theory for slow viscous flow*, Journal of Fluid Mechanics, 75 (1976), p. 705–714.

[48] S. Kim, S. Lee, J. Lee, B. J. Nelson, L. Zhang, and H. Choi, *Fabrication and manipulation of ciliary microrobots with non-reciprocal magnetic actuation*, Scientific Reports, 6 (2016).

[49] G. S. Klindt, C. Ruloff, C. Wagner, and B. M. Friedrich, *Load response of the flagellar beat*, Physical Review Letters, 117 (2016).

[50] G. S. Klindt, C. Ruloff, C. Wagner, and B. M. Friedrich, *In-phase and anti-phase flagellar synchronization by waveform compliance and basal coupling*, New Journal of Physics, 19 (2017), p. 113052.

[51] O. M. Koo, I. Rubinstein, and H. Onyuksel, *Role of nanotechnology in targeted drug delivery and imaging: A concise review*, Nanomedicine: Nanotechnology, Biology and Medicine, 1 (2005), p. 193–212.

[52] E. Lauga and T. R. Powers, *The hydrodynamics of swimming microorganisms*, Reports on Progress in Physics, 72 (2009), p. 096601.

[53] C. Li, B. Chakrabarti, P. Castilla, A. Mahajan, and D. Saintillan, *Chemomechanical model of sperm locomotion reveals two modes of swimming*, Physical Review Fluids, 8 (2023).

[54] C. Li, B. Qin, A. Gopinath, P. E. Arratia, B. Thomases, and R. D. Guy, *Flagellar swimming in viscoelastic fluids: Role of fluid elastic stress revealed by simulations based on experimental data*, Journal of The Royal Society Interface, 14 (2017), p. 20170289.

[55] J. Lighthill, *Mathematical Biofluiddynamics*, Society for Industrial and Applied Mathematics, 1975.

[56] ———, *Flagellar hydrodynamics*, SIAM Review, 18 (1976), p. 161–230.

[57] C. B. Lindemann, *A model of flagellar and ciliary functioning which uses the forces transverse to the axoneme as the regulator of dynein activation*, Cell Motility, 29 (1994), p. 141–154.

[58] ———, *A "geometric clutch" hypothesis to explain oscillations of the axoneme of cilia and flagella*, Journal of Theoretical Biology, 168 (1994), p. 175–189.

[59] K. G. Link, R. D. Guy, B. Thomases, and P. E. Arratia, *Effect of fluid elasticity on the emergence of oscillations in an active elastic filament*, Journal of The Royal Society Interface, 21 (2024).

[60] R. Ma, G. S. Klindt, I. H. Riedel-Kruse, F. Jülicher, and B. M. Friedrich, *Active phase and amplitude fluctuations of flagellar beating*, Physical Review Letters, 113 (2014).

[61] O. Maxian, A. Mogilner, and A. Donev, *Integral-based spectral method for inextensible slender fibers in stokes flow*, Physical Review Fluids, 6 (2021).

[62] A. Maćkiewicz and W. Ratajczak, *Principal components analysis (pca)*, Computers & Geosciences, 19 (1993), p. 303–342.

[63] I. Minoura and R. Kamiya, *Strikingly different propulsive forces generated by different dynein-deficient mutants in viscous media*, Cell Motility, 31 (1995), p. 130–139.

[64] M. J. M uller, S. Klumpp, and R. Lipowsky, *Tug-of-war as a cooperative mechanism for bidirectional cargo transport by molecular motors*, Proceedings of the National Academy of Sciences, 105 (2008), p. 4609–4614.

[65] A. Nandagiri, A. S. Gaikwad, D. L. Potter, R. Nosrati, J. Soria, M. K. O'Bryan, S. Jadhav, and R. Prabhakar, *Flagellar energetics from high-resolution imaging of beating patterns in tethered mouse sperm*, eLife, 10 (2021).

[66] D. Oriola, H. Gadêlha, and J. Casademunt, *Nonlinear amplitude dynamics in flagellar beating*, Royal Society Open Science, 4 (2017), p. 160698.

[67] B. Qin, A. Gopinath, J. Yang, J. P. Gollub, and P. E. Arratia, *Flagellar kinematics and swimming of algal cells in viscoelastic fluids*, Scientific Reports, 5 (2015).

[68] I. H. Riedel-Kruse, A. Hilfinger, J. Howard, and F. Jülicher, *How molecular motors shape the flagellar beat*, Human Frontier Science Program Journal, 1 (2007), p. 192–208.

[69] U. Rüffer and W. Nultsch, *High-speed cinematographic analysis of the movement of Chlamydomonas*, Cell Motility, 5 (1985), pp. 251–263.

[70] G. Saggiorato, L. Alvarez, J. F. Jikeli, U. B. Kaupp, G. Gompper, and J. Elgeti, *Human sperm steer with second harmonics of the flagellar beat*, Nature Communications, 8 (2017).

[71] H. Sakakibara, H. Kojima, Y. Sakai, E. Katayama, and K. Oiwa, *Inner-arm dynein c of chlamydomonas flagella is a single-headed processive motor*, Nature, 400 (1999), p. 586–590.

[72] A. S. Sangani, J. Vidyadharan, and K. W. Foster, *Analysis of the forces acting on beating cilia*, Journal of Physics D: Applied Physics, 49 (2016), p. 255401.

[73] P. Sartori, V. F. Geyer, A. Scholich, F. Jülicher, and J. Howard, *Dynamic curvature regulation accounts for the symmetric and asymmetric beats of chlamydomonas flagella*, eLife, 5 (2016).

[74] A. Solovev and B. M. Friedrich, *Synchronization in cilia carpets and the kuramoto model with local coupling: Breakup of global synchronization in the presence of noise*, Chaos: An Interdisciplinary Journal of Nonlinear Science, 32 (2022).

[75] A. Solovev and B. M. Friedrich, *Synchronization in cilia carpets: Multiple metachronal waves are stable, but one wave dominates*, New Journal of Physics, 24 (2022), p. 013015.

[76] B. J. Walker, S. Phuyal, K. Ishimoto, C.-K. Tung, and E. A. Gaffney, *Computer-assisted beat-pattern analysis and the flagellar waveforms of bovine spermatozoa*, Royal Society Open Science, 7 (2020), p. 200769.

[77] S. Werner, J. C. Rink, I. H. Riedel-Kruse, and B. M. Friedrich, *Shape mode analysis exposes movement patterns in biology: Flagella and flatworms as case studies*, PLoS ONE, 9 (2014).

[78] K. S. Wilson, O. Gonzalez, S. K. Dutcher, and P. V. Bayly, *Dynein-deficient flagella respond to increased viscosity with contrasting changes in power and recovery strokes*, Cytoskeleton, 72 (2015), p. 477–490.

[79] R. Womersley, *Maximum determinant (fekete, extremal) points on the sphere*. https://web.maths.unsw.edu.au/~rsw/Sphere/MaxDet/, Jun 2020.

[80] L. G. Woodhams, Y. Shen, and P. V. Bayly, *Generation of ciliary beating by steady dynein activity: The effects of inter-filament coupling in multi-filament models*, Journal of the Royal Society Interface, 19 (2022).

[81] D. Woolley and G. Vernon, *Functional state of the axonemal dyneins during flagellar bend propagation*, Biophysical Journal, 83 (2002), p. 2162–2169.

[82] T. Yagi, I. Minoura, A. Fujiwara, R. Saito, T. Yasunaga, M. Hirono, and R. Kamiya, *An axonemal dynein particularly important for flagellar movement at high viscosity*, Journal of Biological Chemistry, 280 (2005), p. 41412–41420.

[83] F. Yazdan Parast, A. S. Gaikwad, R. Prabhakar, M. K. O'Bryan, and R. Nosrati, *The cooperative impact of flow and viscosity on sperm flagellar energetics in biomimetic environments*, Cell Reports Physical Science, 4 (2023), p. 101646.

[84] K. Zhang, A. Lewis, A. Klingner, V. Magdanz, S. Misra, and I. S. Khalil, *Locomotion of paired spermatozoa during flagellar synchronisation*, Journal of Fluid Mechanics, 1007 (2025).